
Artificial Intelligence in Brain Micro-Architecture Investigation Using Clinical Diffusion MRI

By
Abrar Faiyaz

Submitted in Partial Fulfillment of the Requirements for the Degree

Doctor of Philosophy



Supervised by
Professor Md Nasir Uddin
Professor Giovanni Schifitto
Professor Marvin M. Doyley

Department of Electrical and Computer Engineering
Arts, Science & Engineering
Edmund A. Hajim School of Engineering & Applied Sciences

University of Rochester
Rochester, NY, USA

January, 2024

To my incredible family...

Mrs Shelina Khatun, my extraordinary Ammu;

*Dr Md Ashraful Alam, my father & mentor without whom I wouldn't have
had an early exposure to Medical Imaging;*

My sibling and partner in intellectual exploration

Anan Faiyaz Radin

Last but not the least, my sweet & sour-

Sayka Sultana Mim!

◊ Alhamdulillah ◊

Table of Contents

Biographical Sketch	ix
Abstract	xiii
Contributors & Funding Sources	xv
List of Tables	xvii
List of Figures	xxvi
List of Acronyms	xxvii
1 Motivation	1
1.1 Context	1
1.2 Problem Statement	3
1.3 Thesis Objective	4
1.3.1 Hypothesis	4
1.3.2 Objectives	4
1.4 Structure of the Thesis	4
2 Background: Diffusion, MRI & Brain Microstructure	7
2.1 Overview	7

2.2	Diffusion	8
2.2.1	Basics of Molecular Movement	8
2.2.2	Einstein's Model of Molecular Diffusion	9
2.2.3	Free, Partial & Completely Restricted Diffusion	10
2.2.4	Diffusion Reveals Microstructure	11
2.3	Magnetic Resonance Imaging	12
2.3.1	Quick Introduction to MR	12
2.3.2	MR Image Generation	15
2.4	Encoding Diffusion using MRI	17
2.4.1	Diffusion Gradient, Time & b-value	19
2.4.2	Diffusion b-vectors & Q-space	20
2.5	Human Brain	22
2.5.1	White Matter	22
2.5.2	Gray Matter	24
2.5.3	Probing Brain Microstructure with dMRI	25
3	General Models, AI & Analysis in dMRI	27
3.1	Overview	27
3.2	Representing Diffusion MR Signals	28
3.2.1	Mathematical modeling	28
3.2.2	Biophysical modeling	32
3.3	Artificial Intelligence (DL/ML) for dMRI	37
3.3.1	General AI (DL/ML) Models	39
3.3.2	AI(DL/ML) Strategies for Microstructure Reconstruction	42
3.4	Statistical Evaluation Frameworks	45
3.4.1	Voxel Based Analysis	45

3.4.2	Tract Based Spatial Statistics (TBSS)	46
3.4.3	ROI Analysis	47
4	AI in Q-Space Up-Sampling: Recovering Lost Clinical Details	49
4.1	Motivation	49
4.2	Optimized Sampling of Q-space	52
4.2.1	HemiHex Sub-Sampling in Q-space	52
4.2.2	Fully Connected Multilayered Perceptron	53
4.2.3	Hemi-Hex Features with Machine Learning Model	55
4.2.4	Optimization	57
4.3	Metrics for Evaluation	57
4.4	Results & Discussion	61
4.4.1	MICCAI Challenge 2022 Score & Standings	62
4.4.2	Image Quality Metrics (SSIM & PSNR)	62
4.4.3	TBSS & True and False Positive Scores	64
4.4.4	Training Resources & Efficiency in Clinical Applications	65
4.5	Limitations & Future directions	69
5	Single-Shell NODDI Reconstruction: Simulation Study	71
5.1	Motivation	71
5.2	Simulation Study Design	72
5.2.1	NODDI Distribution in Healthy Human Brains	73
5.2.2	Microstructure Parameters for Simulation	74
5.2.3	Simulation Protocols	76
5.3	Proposed Architectures for Single-Shell NODDI	77
5.4	Results	81
5.4.1	Conditioning Single-Shell NODDI Problem	82

5.4.2	Estimation of Independent f_{ISO} with Single-Shell	84
5.5	Discussion	86
5.6	Limitation & Future Direction	88
6	AI in Single-Shell NODDI: Clinical Application & Validation	89
6.1	Motivation	89
6.2	Data Acquisition & Quality Comparison	90
6.2.1	High Quality Data: Human Connectome Project	90
6.2.2	Clinical Data: Cerebrovascular Small Vessel Disease	91
6.2.3	Data Analysis	92
6.3	Training, Validation & Test	92
6.4	Results & Discussion: Incorporating T2-w and MD Priors	95
6.4.1	Simulation	96
6.4.2	<i>In-vivo</i>	99
6.5	Clinical Validation of Single-Shell NODDI	106
6.5.1	Single-Shell Contrast on White Matter Hyperintensity	108
6.5.2	Error (%) & Pearson Correlation of GM & WM ROIs	109
6.5.3	Aging Vs Single/Multi-shell derived NDI, ODI & f_{ISO}	112
6.5.4	Cognitive Scores of HIV+ & Control Subjects Vs Single & Multi-shell Derived NDI, ODI & f_{ISO}	117
6.6	Conclusions	126
7	Summary of Contributions & Future Directions	129
7.1	Summary of Key Results	129
7.2	Discussion	131
7.2.1	Retrieving Lost DTI-based Microstructure Differences	131

7.2.2	Retrieving Neurite & Extracellular Sensitivity with Single-Shell NODDI	132
7.3	Future Opportunities	133
7.3.1	Q-space Up-sampling without Optimized Diffusion Protocol .	133
7.3.2	Single-Shell NODDI in Clinical Longitudinal Study	135
7.3.3	Multi-modal Sensitivity & AI in General MR	135
7.3.4	Tackling Data Scarcity in Clinical dMRI	137
	Bibliography	138



Biographical Sketch

ABRAR FAIYAZ, born in Dhaka, Bangladesh, is an esteemed scholar with a background in Computer Science and Engineering (CSE). He earned his BSc in CSE from the Islamic University of Technology (IUT), receiving the *OIC Gold Medal* for academic excellence. He completed his internship in *Samsung Research & Development Institute, Bangladesh* in 2016 and in 2017, he was appointed as a Lecturer in the CSE department of *IUT* for Microprocessor Programming & Computer Graphics. Because of his interest in Medical Imaging and Machine Learning, Abrar engaged in research on machine learning features of ultrasound images during his undergraduate studies with Professor Hasanul Kabir and Dr. Kaiser Alam, a visiting Professor at IUT from Riverside Research Institute, NY. This led him to pursue his graduate studies on artificial intelligence(ML/DL) for Medical Imaging in Electrical Engineering at the University of Rochester, where he completed his MS in 2020. Collaborating with experts such as Dr. Marvin Doyley, Giovanni Schifitto, and Md Nasir Uddin, his doctoral research focused on brain micro-structure modeling with Clinical Diffusion MRI & AI. The following publications were the result of work conducted during his doctoral study.

Journal Articles

- J1.** Faiyaz, A., Doyley, M., Schifitto, G., Zhong, J., Uddin, M. N., “Single-shell noddi using dictionary-learner- estimated isotropic volume fraction,” *NMR in Biomedicine*, vol. 35, no. 2, e4628, 2022
- J2.** Faiyaz, A., Doyley, M. M., Schifitto, G., Uddin, M. N., “Artificial intelligence for diffusion mri-based tissue microstructure estimation in the human brain: An overview,” *Frontiers in Neurology*, vol. 14, p. 1 168 833, 2023.
- J3.** Aja-Fernandez, S., Martin-Martin, C., Planchuelo-Gomez, A., Faiyaz, A., Uddin, M.N., Schifitto, G. et al, “Validation of deep learning techniques for quality augmentation in diffusion MRI for clinical studies,” *NeuroImage: Clinical*, vol. 39, p. 103 483, Jan. 2023.
- J4.** Finkelstein, A., Faiyaz, A., Weber, M. T., Qiu, X., Uddin, M. N., Zhong, J., Schifitto, G., “Fixel-based analysis and free water corrected dti evaluation of hiv associated neurocognitive disorders,” *Frontiers in Neurology*; 2021.
- J5.** Uddin, M. N., Faiyaz, A., Wang, L., Zhuang, Y., Murray, K. D., Descoteaux, M., Tivarus, M. E., Weber, M. T., Zhong, J., Qiu, X., “A longitudinal analysis of brain extracellular free water in hiv infected individuals,” *Scientific Reports*, vol. 11, no. 1, pp. 1–12, 2021.
- J6.** Diba, T., Faiyaz, A., Akhlagi, N., Doyley, M., Alam, S. K., Zara, J., Garra, B., “Elastic modulus quantification from strain elastograms: Progress towards a low cost alternative to shear wave elastography,” *Journal of Ultrasound in Medicine*, vol. 39, no. S1, S26–S31, 2020.

- J7.** Korshunov, V. A., Smolock, E. M., Wines-Samuelson, M. E., **Faiyaz, A.**, Mickelsen, D. M., Quinn, B., Pan, C., Dugbartey, G. J., Yan, C., Doyley, M. M., “Natriuretic peptide receptor 2 locus contributes to carotid remodeling,” *Journal of the American Heart Association*, vol. 9, no. 10, e014257, 2020.
- J8.** Korshunov, V. A., Quinn, B., **Faiyaz, A.**, Ahmed, R., Sowden, M. P., Doyley, M. M., Berk, B. C., “Strain- selective efficacy of sacubitril/valsartan on carotid fibrosis in response to injury in two inbred mouse strains,” *British Journal of Pharmacology*, vol. 176, no. 15, pp. 2795–2807, 2019

Conference Proceedings

- C1.** **Faiyaz, A.**., Weber, M., Kabir, I., Doyley, M. M., Sack, I., Uddin, M. N., Schifitto, G., “Evaluating mre-tract integrity in hiv-csvd cohort: A comprehensive analysis with functionally defined atlases and neurocognitive assessment,” in Proc. Intl. Soc. Mag. Reson. Med. 32, 2024.
- C2.** **Faiyaz, A.**, Hoang, N., Finkelstein, A., Zhong, J., Doyley, M., Wang, H., Uddin, M. N., Schifitto, G., “Bayestextract: Automated Machine Learning based brain artery segmentation, anatomical prior annotation and feature-extraction in MR Angiography,” in Proc. Intl. Soc. Mag. Reson. Med. 30, 2022.
- C3.** **Faiyaz, A.**, Doyley, M. M., Schifitto, G., Zhong, J., Uddin, M. N., “Deep learner estimated isotropic volume fraction enables reliable single-shell noddii reconstruction,” in Proc. Intl. Soc. Mag. Reson. Med. 29, 2021.
- C4.** **Faiyaz, A.**, Kabir, I. E., Doyley, M. M., Sack, I., Uddin, M. N., Schifitto, G., “Preliminary mr elastography investigation on hiv+ cohort with cerebral small vessel disease,” in Proc. Intl. Soc. Mag. Reson. Med. 29, 2021.

- C5.** Faiyaz, A., Zhuang, Y., Doyley, M., Zhong, J., Descoteaux, M., MN, U., Schifitto, G., “Effect of free water correction in grey and white matter in cart treated hiv patients,” in 26th Annual Meeting of the Organization for Human Brain Mapping, 2020.
- C6.** Uddin, M. N., **Faiyaz, A.**, Finkelstein, A., Schifitto, G., “Myelin water imaging in an hiv population at risk of cerebral small vessel disease,” in Proc. Intl. Soc. Mag. Reson. Med. 30, 2022.
- C7.** Finkelstein, A., **Faiyaz, A.**, Uddin, M., Zhong, J., Schifitto, G., “Machine learning classification of hiv associated neurocognitive disorders (hand) based on fiber specific white matter change,” in 27th Annual Meeting of the Organization for Human Brain Mapping, 2021.
- C8.** Uddin, M. N., **Faiyaz, A.**, Schifitto, G., “Evaluation of white matter microstructure in an hiv population at risk of cerebral small vessel disease using microscopic fractional anisotropy,” in Proc. Intl. Soc. Mag. Reson. Med. 29, 2021.
- C9.** Murray, K., **Faiyaz, A.**, Sahin, B., Tivarus, M., Uddin, M. N., Venkataraman, A., Wang, H., Zhuang, Y., Zhong, J., Maggirwar, S., “Tract-based spatial statistics of cerebral small vessel disease in an hiv population,” in 26th Annual Meeting of the Organization for Human Brain Mapping, 2020.
- C10.** Uddin, M. N., **Faiyaz, A.**, Zhuang, Y., Tivarus, M., Zhong, J., Descoteaux, M., Schifitto, G., “Relationship between free water and neuroinflammation/neurodegeneration markers in hiv before and after combination antiretroviral therapy,” in Proc. Intl. Soc. Mag. Reson. Med. 28, 2020.

Abstract

This thesis presents a comprehensive study aimed at overcoming significant limitations in clinical diffusion MRI (dMRI), with a specific focus on enhancing the resolution of Q-space and the effective use of single-shell data for improved characterization of brain microstructures. The research addresses the problem of inadequate angular resolution in standard clinical diffusion MRI, which often leads to missing crucial clinical details. Additionally, it tackles the difficulty of characterizing neurite orientation dispersion and density, which is challenging without multi-shell data but is essential for probing biologically meaningful parameters in the brain.

Central to this research is the hypothesis that clinical dMRI can recover lost microstructural details from limited Q-space resolution in single-shell protocols. This recovery is achieved by integrating Diffusion Tensor Imaging (DTI) and Neurite Orientation Dispersion and Density Imaging (NODDI) with advanced Artificial Intelligence (AI) techniques, along with the use of relevant multi-modal clinical priors. The study aims to accomplish two primary objectives: first, to develop a sophisticated Q-space up-sampling technique that improves angular resolution using DTI without compromising clinical details; and second, to effectively address the ill-posed problem of single-shell NODDI, culminating in its reliable reconstruction validated through clinical applications.

The research methodology involves a combination of theoretical and practical

approaches, including the simulation of the single-shell ill-posed problem of NODDI and the identification of a key parameter, f_{ISO} , that is instrumental in resolving this issue. Additionally, the study explores the application of multi-modal MR priors for the estimation of f_{ISO} and investigates the feasibility of applying NODDI in both single- and multi-shell settings. This includes clinical validation in contexts of aging and cognitive performance in a cohort of HIV and Cerebral Small Vessel Disease (CSVD).

In conclusion, this thesis makes a remarkable contribution to the field of clinical diffusion MRI by proposing innovative methodology for enhancing Q-space resolution and effectively utilizing single-shell data, leading to more accurate and detailed characterization of brain microstructures. The findings and methodologies developed have the potential to influence future research and clinical practices in the realm of neuroimaging.

Contributors & Funding Sources

The thesis and associated research works was supported by the National Institute of Health (R01 MH118020; R01 AG054328; U54 MH091657; U01 AG052564; R01 HL123346; R21 NS113674), US and by the Hajim School of Engineering & Applied Sciences, University of Rochester. The dissertation committee consisted of the following members,

- **Professor Marvin M. Doyley, Ph.D.**
 - *Department:* Electrical and Computer Engineering
 - *Role:* Official advisor and mentor, providing guidance and support throughout the research process.
- **Professor Md Nasir Uddin, Ph.D.**
 - *Department:* Neurology
 - *Role:* Significantly contributed to the research by providing valuable guidance, expert advice, and assistance in understanding the intricate neurological aspects of the study.
- **Professor Giovanni Schifitto, M.D.**
 - *Department:* Neurology

- *Role:* Provided substantial funding for the research and offered invaluable clinical insights, significantly influencing the direction and outcomes of the study.

- **Professor Gonzalo Mateos Buckstein, Ph.D.**

- *Department:* Electrical and Computer Engineering
- *Role:* Served as a key member of the dissertation committee, offering critical evaluations and constructive feedback, contributing to the intellectual rigor of the thesis.

List of Tables

3.1	Classification of fundamental AI architectures with feature types.	38
3.2	Neuro-biophysical models with their key parameters and relevant unified AI applications in diffusion MRI is classified in blocks.	43
4.1	MICCAI Challenge 2022 (Quad'22) Results retrieved from Quad22 website	62
4.2	Comparison of visual metrics achieved through different methods. [5]	63
4.3	Number of subjects in each approach for training, validation, and testing, along with the loss function used for training procedure [5] . . .	67
5.1	Diffusion MR protocol & key parameter values for DWI simulation .	75
5.2	f_{ISO} determined as the bottleneck parameter in Rician Log-likelihood fitting of simulation data in experiment-3 where NDI, ODI was fitted parameters and f_{ISO} was known.	82

List of Figures

2.1	A) Molecular Diffusion of ink, a physical phenomenon hallucinated by DALL-E. B) Diffusion simulation in 2D, demonstrating Einstein's model of diffusion for a freely diffusing particle.	9
2.2	Demonstration of linear diffusion in the diffusion of a free particle; and, non linear diffusion in the diffusion of partial/completely restricted particles	10
2.3	Schematic depiction of how different diffusion properties may appear in different tissue types in the brain. The scanning Electron Microscopic image was adapted from [19]	11
2.4	Example MRI T1 magnitude reconstructed from the sampled complex MRI signals on the k-space, shown as Amplitude and Phase (in radian)	17
2.5	Schematic diagram of timing in PGSE sequence	19
2.6	Diffusion Length is inversely proportional to the diffusion signal from dMR. (A) and (B) adapted with permission from <i>John Wiley and Sons</i> [28]. (C) Demonstrates the non-linear relationship still holds for increasing b-value in partial/restricting compartments for Diffusion Length.	20
2.7	Multi-shelled Q-space in diffusion protocols, shown with their relationship to diffusion length.	21

2.8	Micro-structure with relative tissue volume fractions of (A) Gray Matter and (B) White Matter adapted from [30].	23
3.1	Example of diffusion scalar maps (FA, MD, AD, RD) derived from fitted diffusion tensors.	31
3.2	Schematic diagram for Neurite Orientation Dispersion and Density Model.	35
3.3	A) NODDI parameters (f_{ISO} , ODI , NDI) in combined HSV colorspace. B and C illustrates the color-map depiction.	36
3.4	dMRI based microstructural reconstruction in human brain: Schematics & Progress through AI: A) general schematics of microstructural reconstruction using biophysical model; B) Multishell diffusion protocol in q-space. C) shows radial summary of types of architectures AI approaches use; D) displays the number of AI approaches proposed over the last decade; D) shows the radial summary of biophysical models these AI approaches are applied to.	40
3.5	Example comparison of diffusion tensor and free water corrected tensor metrics (fwcDTI) using (a) TBSS and (b, c, d) GBSS analysis of HIV+ compared with age matched healthy controls at baseline. TBSS and GBSS Skeletons are in Green. TFCE corrected significance shown with blue(reduced) or red(increased).	46
3.6	Example of atlas based ROI analysis between HIV+ and Control groups where the stiffness modulus ($ G^* $), a parameter relating to brain tissue elasticity shows significantly reduced in the HIV group. JHU WM and HO cortical and subcortical atlases were used for the analysis. Significant ROIs ($p<0.01$) are overlaid on an MNI T1 image.	48

4.1	Axial Diffusivity difference in Chronic vs Episodic Migraine population (FW-corrected $p < 0.05$) top row with 61 and bottom row with 21 gradient directions, adapted with permission from Professor Santiago Aja-Fernández [4, 114]	52
4.2	Hemi-hex subsampling on Q-space, the center node is an unknown surrounded with 3 known and unknowns.	53
4.3	Schematics of angular upsampling of diffusion MR using contextual HemiHex sub-sampling in an optimized Q-space using HemiHex-based MLP/FCN.	54
4.4	The Multi-Layer Perceptron for Q-Space Upsampling is shown in a schematic diagram, The layers are FC- Fully Connected, tanh, DropOut(20%) with around 2500 learnable parameters. Red segments on five-tissue MRI map depicts patch based random sampling of training and validation ROIs.	56
4.5	Sequential three step optimization reduce mean squared loss linearly (y-axis shown in log-scale).	58
4.6	True and False Positive ROIs detected in Axial and Mean Diffusivity by different methods (Sorted by Ranking). Data for comparison were obtained from CDMRI'22 workshop. HemiHex-based MLP is our proposed approach [76], compared to other techniques, results reported from [5]	66
5.1	Single-shell data cannot reconstruct NODDI (NDI, ODI, f_{ISO}). Three parameters are merged in HSV space for combined viusalization . . .	72
5.2	NODDI parameter (NDI, f_{ISO} , ODI) distribution in three healthy control subjects from HCP	74

5.3	NODDI parameter (NDI, f_{ISO} , ODI) based simulated data inspired from the distribution in healthy human brain	75
5.4	Close Visualization of Constrained Spherical De-convolution based Spherical Harmonics (SH) representation of simulated diffusion data.	76
5.5	Schematic of the proposed DLpN. The stochastic dictionary learning framework (DictNet) estimates f_{ISO} prior and then used with NODDI Rician log-likelihood estimation steps for <i>NDI</i> and κ mapping. A) DictNet, B) DLpN.	78
5.6	Neurite Density Index Results with conditioned f_{ISO} . GT -Ground Truth.	83
5.7	Orientation Dispersion Index Results with conditioned f_{ISO} . GT - Ground Truth.	85
5.8	Invivo NDI estimation using multi-shell derived f_{ISO} using single shell protocol P1. Multishell derived NDI is shown for reference.	86
5.9	Estimation failure of f_{ISO} independently	87
6.1	Signal-to-noise ratio (SNR) of the dMRI data for Human Connectome Project with connectome research scanner and CSVD clinical data, shows the significant SNR differences as higher gradient strengths are in use.	93
6.2	Demonstration of minimum error with data sampling from two subjects. Training with higher number of subjects suggests over-fitting dictionary based network.	94
6.3	Comparison of DictNet with and without prior. Training for both cases involved identical optimization parameters and iterations.	97

6.4 Dictionary-based network (DictNet) estimation of f_{ISO} at ground-truth values A) 0, B) 0.12, C) 0.4, D) 0.75, E) 1 (indicated with a dashed line) on the simulation test set with defined protocols P1, P2, P3, P12, P13, P23 and Pall for different NDI ground-truth values provided in Figure 5.6. DictNet generated f_{ISO} are compared with other methods such as NODDI, PMEDN, and	98
6.5 Extreme case estimation distribution for NODDI and DLpN, with ground-truth parameters shown for single-shell protocol P1 (i.e., $b=1000 s/mm^2$) and multi-shell protocol P12 (i.e., $b=1000 s/mm^2$ and $b=2000 s/mm^2$). Left column represents high MD and high f_{ISO} cases corresponds to low NDI and normal f_{ISO} (i.e., $NDI = 0.2$, $f_{ISO} = 0.12$ in Figure 6.4) while right column represents normal MD and high f_{ISO} corresponds to the case of high NDI and high f_{ISO} (i.e., $NDI = 0.8$, $f_{ISO} = 0.4-0.75$ in Figure 6.4). Note GT: ground-truth.	100
6.6 Combined parameter maps (f_{ISO} , ODI & NDI) are shown per protocol in HSV colorspace (Section-3.2.2.1), demonstrating single-shell and multi-shell reconstructions from DLpN and NODDI.	101
6.7 A) A representative axial view of the f_{ISO} maps estimated with proposed DictNet and NODDI for different protocols. Note, $NODDI_{Pall}$ f_{ISO} is considered as pseudo-ground-truth f_{ISO} and used as training data for DictNet; B) Difference maps for DictNet f_{ISO} and NODDI f_{ISO} with respect to $NODDI_{Pall}$ f_{ISO} for defined protocols. Intensity scales are shown.	102

6.8 a) (A) A representative axial view of microstructural maps of NDI and (B) difference maps (with respect to $NODDI_{Pall}$) estimated with proposed DLpN and NODDI for different protocols on a human connectome project (HCP) subject. b) A representative axial view of microstructural maps of ODI and (B) difference maps (with respect to $NODDI_{Pall}$) estimated with proposed DLpN and NODDI for different protocols. Intensity scales are shown. Note, $NODDI_{Pall}$ is considered as pseudo-ground-truth for comparison.	103
6.9 A) A representative axial view of the NDI, ODI, and fractional isotropy (f_{ISO}) maps estimated with proposed DLpN and NODDI for different protocols in CSVD. Note, $NODDI_{Pall} f_{ISO}$ is considered as pseudo-ground-truth f_{ISO} and used as training data for DictNet; B) Corresponding difference maps for DLpN-derived maps with respect to $NODDI_{Pall}$ for defined protocols P1 and P2. Intensity scales are shown.	104
6.10 Log histograms for the objective values of DLpN P1, P2, P3 and $NODDI_{Pall}$ with (A) HCP and (B) CSVD test subjects. Positive direction along the x-axis corresponds to higher objective values. The goal for both NODDI and DLpN is to maximize the objective function. Region A is defined as the set of bins where the NODDI probability density function has lower objective values than DLpN	105
6.11 Qualitative SNR comparison between single shell and multishell NODDI	107
6.12 Comparison of DLpN derived NDI and f_{ISO} maps with $NODDI_{Pall}$ in CSVD	108

6.13 The estimation errors (%) from in vivo data in isotropic volume fraction f_{ISO} (A, B), neurite density index NDI (C, D) and orientation dispersion index ODI (E, F) for white matter (WM) and gray matter (GM) using DLpN single-shell protocols P1, P2, P3, and multi-shell protocols P12, P12, P23 and Pall. Errors were calculated with respect to the pseudo-ground-truth ($NODDI_{Pall}$) for six HCP test subjects.	110
6.14 Pearson correlation with 8 HCP subjects using JHU WM (68) and HO cortical/sub-cortical GM (48+21) ROIs	111
6.15 Correlation of mean f_{ISO} with aging from the combined JHU White Matter ROIs (squares) and combined Harvard-Oxford Cortical and Subcortical GM ROIs (circles)	113
6.16 Correlation of mean NDI with Aging from the combined JHU White Matter ROIs (squares) and combined Harvard-Oxford Cortical and Subcortical GM ROIs (circles)	115
6.17 Correlation of mean ODI with Aging from the combined JHU White Matter ROIs (squares) and combined Harvard-Oxford Cortical and Sub-cortical GM ROIs(circles)	116
6.18 Correlation of f_{ISO} with Cognitive Scores of HIV+ and Control subjects using the combined JHU White Matter ROIs (squares) as Global WM and combined Harvard-Oxford Cortical/ Subcortical GM as Global GM ROI (circles)	118
6.19 Correlation of NDI with Cognitive Scores of HIV+ and Control subjects using the combined JHU White Matter ROIs (squares) as Global WM and combined Harvard-Oxford Cortical/ Subcortical GM as Global GM ROI (circles)	120

6.20 Correlation of ODI with Cognitive Scores of HIV+ and Control subjects using the combined JHU White Matter ROIs (squares) as Global WM and combined Harvard-Oxford Cortical/Subcortical GM as Global GM (circles)	121
7.1 Zonal feature ($F_u(\theta_j)$) extraction from the Q-space using machine learner feature proposed by Karimi et al. [82]	133
7.2 Zonal feature block with a 3D CNN trained with three phase optimization to upsample diffusion signal.	134
7.3 Loss comparison indicates performance using Q-space zonal feature block based network is better compared to HemiHex-FCN.	134
7.4 Example of multimodal MRI shows functional connectivity analysis of Visuo-Spatial Network using Diffusion and MR Elastography, where connectivity maps are generated from diffusion tractography. 34 control and 30 HIV subjects are used in the analysis.	136

List of Acronyms

fISO Fractional Isotropy or Free Water.

AD Axial Diffusivity.

ADC Apparent Diffusion Coefficient.

ADL Atlas-powered Deep Learning.

AEME Adaptive Network with Extragradient for Diffusion MRI-Based Microstructure Estimation.

AI Artificial Intelligence.

ANOVA Analysis of Variance.

CM Chronic Migraine.

CNN Convolution Neural Network.

CSD Constrained Spherical Deconvolution.

CSF Cerebro-Spinal Fluid.

CSVD Cerebral Small Vessel Disease.

DKI Diffusion Kurtosis Imaging.

DL Deep Learning.

DLpN Deep Learning prior NODDI.

dMRI diffusion MRI.

DTI Diffusion Tensor Imaging.

DTI SR Diffusion Tensor Imaging Super Resolution.

DWI Diffusion Weighted Image.

EC Extra-cellular.

ED-RNN Encoder-Decoder Recurrent Neural Network.

EM Episodic Migraine.

FA Fractional Anisotropy.

FCN Fully Connected Network.

fODF Fiber orientation distribution function.

FP False Positive.

FW DTI based Free Water.

FWE-DT Free Water Eliminated Diffusion Tensor.

FWI Free Water Imaging.

GAN Generative Adversarial Network.

GBSS Gray matter Based Spatial Statistics.

GCN Graph Convolutional Network.

GCNN Graph Convolutional Neural Network.

GFA General Fractional Anisotropy.

GM Gray Matter.

GT Ground Truth.

HAR High Angular Resolution.

HC Healthy Control.

HCP Human Connectome Project.

HGT Hybrid Graph Transformer.

HH HemiHex.

HIV Human Immunodeficiency Virus.

HSV Hue, Saturation and intensity Value.

ICVF Intra-Cellular Volume Fraction.

IHT Iterative Hard Thresholding.

IMOC Iterative Maximum Overlap Construction.

IQT Image Quality Transfer.

IVIM Intravoxel Incoherent Motion.

LAR Low Angular Resolution.

LSTM Long Short Term Memory.

MD Mean Diffusivity.

MEDN Microstructure Estimation using a Deep Network.

MESC-Net Microstructure Estimation with Sparse Coding.

METSC Microstructure Estimation using Transformers and Convolutional networks.

ML Machine Learning.

MLE Maximum Likelihood Estimation.

MLP Multi-Layer Perceptron.

MNI Montreal Neurological Institute.

MRE Magnetic Resonance Elastography.

MRI Magnetic Resonance Imaging.

MSD Mean Squared Displacement.

NDI Neurite Density Index.

NMR Nuclear Magnetic Resonance.

NODDI Neurite Orientation Dispersion and Density Imaging.

ODI Orientation Dispersion Index.

PGSE Pulsed Gradient Spin Echo.

PMEDN Extended Microstructure Estimation using a Deep Network.

PSNR Peak Signal-to-Noise Ratio.

q-DL q-Space Deep Learning.

RD Radial Diffusivity.

RDT Residual Dense Transformer.

Residual Network Deep learning model using Residual connections.

RF Radiofrequency.

RMSE Root Mean Squared Error.

RNN Recurrent Neural Network.

ROI Region of Interest.

RTOP Return to the Origin Probability.

SANDI Soma And Neurite Density Imaging..

SCN Spherical Convolution Network.

SDnDTI Self-supervised deep learning-based denoising for diffusion tensor MRI.

SE Spin Echo.

SE-EPI Spin Echo- Echo Planar Imaging.

SEM Scanning Electron Microscope.

SGDM Stochastic Gradient Descent with Momentum.

SH Spherical Harmonics.

SHORE Simple Harmonic Oscillator based Reconstruction and Estimation.

SHResNet Spherical Harmonics Residual Network.

SMT Spherical Mean Technique.

SNR Signal-to-Noise Ratio.

SRDTI Super-Resolution Diffusion Tensor Imaging.

SRqDL Super-Resolved q-Space Deep Learning.

SSIM Structural SIMilarity.

TAGCN Topology Adaptive Graph Convolutional Network.

TBSS Tract Based Spatial Statistics.

TE Echo Time.

TFCE Threshold free cluster enhancement.

TP True Positive.

TR Repetition time.

U-net++ an advanced version of U-net.

VBA Voxel Based Analysis.

ViT Vision Transformer.

VRfRNet Volumetric ROI fODF Reconstruction Network.

WM White Matter.

WMHI White Matter Hyperintensity.

WMTI White Matter Tract Integrity.

Chapter 1

Motivation

“The goal is to turn data into information, and information into insight.”

- Carly Fiorina

1.1 Context

Medical Imaging has come a long way with Magnetic Resonance Imaging (MRI). Among all the non-invasive means of imaging, MRI has presented us with radiation-free, safe and reliable reconstruction of images modern medicine can offer [1]. Over the years, physicists have taken this approach further in different dimensions. One of this prominent dimension was achieved by incorporating diffusion sensitivity with MR. Although expensive and time consuming, diffusion MRI (dMRI) can non-invasively detect microstructural abnormalities in the brain by utilizing micrometer-scale displacement of tissue water [2]. This has now been *adapted* to become more common in clinical imaging protocols. Clinical diffusion protocols are usually acquired with a lower number of gradient directions leading to low angular resolution and lower clarity (Signal-to-Noise Ratio (SNR)) in order to reduce time burden of scanning [3]. As expected, this has reportedly led us to lose clinically meaningful information in

the process [4, 5].

Modeling conventional clinical data involves studying Diffusion Tensor Imaging (DTI) and in contrast, for modeling advanced biophysical models (e.g. Neurite Orientation Dispersion and Density Imaging (NODDI)) that mimic human brain micro-structure, data are often acquired with high gradient strengths and diffusion time, which is also known as multi-shell data. Clinical dMRI often lacks the physically required multi-shell information to probe into biologically meaningful compartmental parameters. Non-invasive visibility of neurite density, extracellular free water f_{iso} and orientation mapping through NODDI can help us investigate neuropathogenesis unlike ever before in clinical domain [6–8]. For example, histologically validated neurite density from NODDI model have shown to decrease in aging population (in both white and gray matter regions) confirming the expected neurological degeneration [9]. But retrieving this requires us to have a reasonable number of diffusion directions and multi-shell data, which introduces timing-complexity, and also makes previously acquired diffusion data in clinical populations unusable [8].

From this perspective, it is clear that we are missing a bridge that can support clinical dMRI gain more sensitivity and visibility in studying digital histology of the human brain. With the advent of computational power, now we can guide machines to learn complex tasks that were not possible before with an active progression of Artificial Intelligence (AI) techniques. Although these approaches are data-driven, there's no free lunch [10], and if used unconditionally, might result in biased conclusions [11]. The application of AI, particularly Deep Learning (DL) methods, significantly improved the visual quality of images and have enabled the generation of novel images from a constrained set of medical imaging data. It is however imperative to acknowledge that the predominant approaches for validating these DL techniques in the context of medical imagery have predominantly relied on visual metrics or quali-

tative assessments as opposed to comprehensive clinical study evaluations. [5] Thus, modeling clinical dMRI with clinically relevant validation techniques hold promise and potentials, yet to be yielded to substantially improve clinical dMRI.

This study is presented to act as a fundamental bridge in studying the dMRI with Artificial Intelligence (Deep/Machine Learning) techniques in order to retrieve biologically meaningful parameters effectively using clinical diffusion data.

1.2 Problem Statement

In general, processing of clinical dMRI includes normal (Gaussian) modeling of the Q-space often carried out without high angular resolution and multi-shell Q-space data. A Q-space is a set of directions for sampling diffusion. A lower angular resolution on the Q-space can miss important clinical details. The strength and time of applying diffusion at a particular direction of Q-space can be played with, and have shown to vary SNR and sensitivity to brain tissue [2,12], this is often termed as multi-shell data. Furthermore, characterization of neurite orientation dispersion and density in multi-compartmental setting has shown to be ill-posed without multi-shell data, which is clinically important to extract biologically meaningful features of the brain [8].

Since clinical dMRI data is limited due to data scarcity and constraints in Q-space, addressing these two aspects of the Q-space restricted by data scarcity —remains challenging in the field.

1.3 Thesis Objective

1.3.1 Hypothesis

Clinical dMRI has the potential to recover lost microstructural details from limited Q-space resolution in single-shell protocols with DTI and NODDI incorporating AI techniques with relevant multi-modal priors available clinically.

1.3.2 Objectives

Engineering multi-modal MRI & angular sampling geometry with AI, we aim -

- To establish a competitive Q-space up-sampling technique that recovers angular resolution without compromising clinical details using DTI.
- To identify and solve ill-posed single-shell NODDI problem and, establish single-shell reconstruction through clinical validation.

1.4 Structure of the Thesis

The thesis is organized into 7 chapters. Following the introductory motivation, problem statement and hypothesis in the **Chapter 1**, the remainder of the thesis is organized as follows:

Chapter 2 - offers a comprehensive understanding of diffusion & MRI, encompassing fundamental aspects such as molecular diffusion, detectable types of diffusion and diffusion observed in the human brain micro-structure; then it introduces the basics of Nuclear Magnetic Resonance (NMR) and highlights the encoding of diffusion measurements through MR non-invasively.

Chapter 3 - discusses general pre-processing, artifacts handling & modeling strategies of acquired diffusion signals on a Q-Space. Modeling expands to inference of brain microstructural configurations using AI (DL/ML) techniques.

Chapter 4 - explores the Q-space super-resolution problem in retaining clinical differences with single-shell clinical dMRI and proposes a solution with features based on Q-space geometry that outperforms state-of-the-art AI techniques.

Chapter 5 - focuses on simulating the single-shell ill-posed problem of NODDI following practical brain fiber configurations and identifies the bottleneck parameter, i.e. the extracellular free water (f_{ISO}) that shows promise in solving the problem.

Chapter 6 - applies clinically available multi-modal MR priors to enable estimation of the bottleneck parameter, f_{ISO} and investigates the application of NODDI in single- and multi-shell settings in the brain. Further extends to clinical validation with CSVD subjects in a White Matter Hyper-intensity case and an aging population.

Chapter 7 - summarizes the primary results obtained in this thesis and discusses future challenges in the field, providing insights to motivate further research.

Chapter 2

Background:

Diffusion, MRI & Brain Microstructure

“All science is either physics or stamp collecting.”

— Ernest Rutherford

2.1 Overview

This chapter intends to provide an overview of the fundamental principles underlying diffusion MRI. It starts with section-2.2, diving into water diffusion as the foundational physical phenomenon assessed by diffusion MRI and its capacity to reveal information about brain tissue microstructure. To measure non-invasive diffusion we move on to section-2.3 where the fundamental principles of MRI is discussed and section-2.4 follows to address the techniques employed to measure water diffusion within the tissue using MRI. In section-2.5, we highlight the schematic anatomy of the gray and white matter that undergo specific type of diffusion because of their underlying histological differences.

2.2 Diffusion

2.2.1 Basics of Molecular Movement

When we focus on molecular diffusion, it's essentially about molecules moving spontaneously. This occurs as long as we're not at absolute zero, or above 0 Kelvin [13]. This kind of motion, was spotted first by Robert Brown in 1827 when he was observing pollen grains under the microscope, is what we call Brownian motion [14]. The phenomenon is like watching tiny particles dancing randomly when suspended in a liquid or gas.

There are two main rules that explain how this dance happens on a larger scale: Fick's laws. The first one tells us how molecules spread out over time, and the second describes how the rate of this spreading changes. Imagine a crowd dispersing after a concert: initially, people move away quickly, but later, as they spread out, they slow down.

A formal mathematical expression of the above ideas are as follows [15]:

$$\vec{J}(\vec{L}, t) = -D \nabla C(\vec{L}, t) \quad (2.1)$$

$$\nabla \cdot \vec{J} = -\frac{\partial C(\vec{L}, t)}{\partial t} \quad (2.2)$$

where J is the flux of the particles, D is the diffusion coefficient and C represents concentration. In this equation \vec{L} is the position at time t . Movement of ink particles dropped in water is a good example of the phenomenon (Figure-2.1(A)).

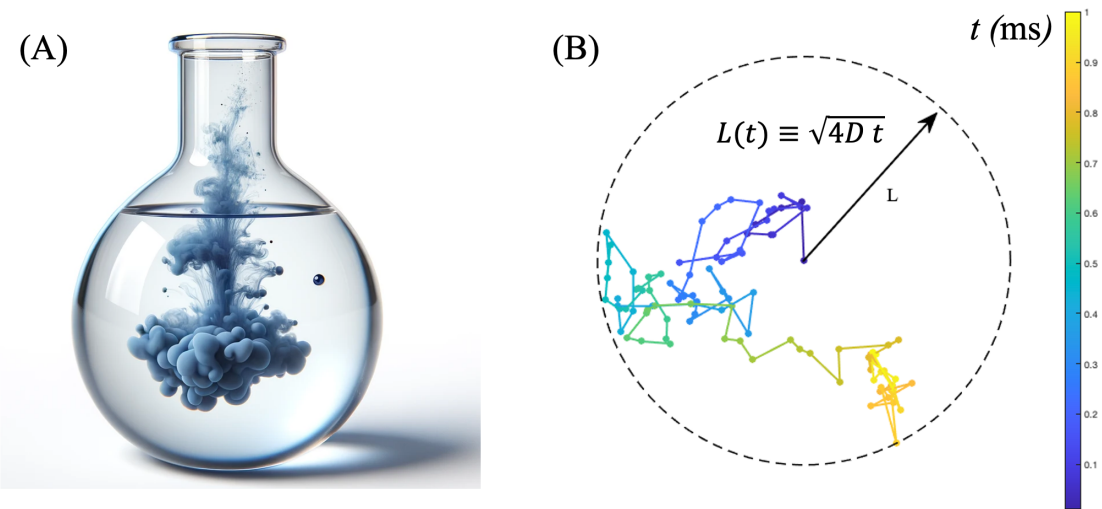


Figure 2.1: A) Molecular Diffusion of ink, a physical phenomenon hallucinated by DALL-E. B) Diffusion simulation in 2D, demonstrating Einstein’s model of diffusion for a freely diffusing particle.

2.2.2 Einstein's Model of Molecular Diffusion

Albert Einstein expanded Fick’s laws to better describe how molecules diffuse on a microscopic scale [16]. He posited that the average distance they travel over a certain period is proportional to the diffusion time. The proportionality is linked with a Diffusion coefficient (D)—a value that depends on molecular size, temperature, and the medium’s thickness [17].

This can be concisely expressed as:

$$\langle L(t) \rangle^2 = 2nDt \quad (2.3)$$

where n is degree of freedom for diffusion, t is diffusion time and $L(t)$ represents diffusion length at time t . Figure-2.1(B) represents free diffusion of a single particle in 2D ($n=2$).

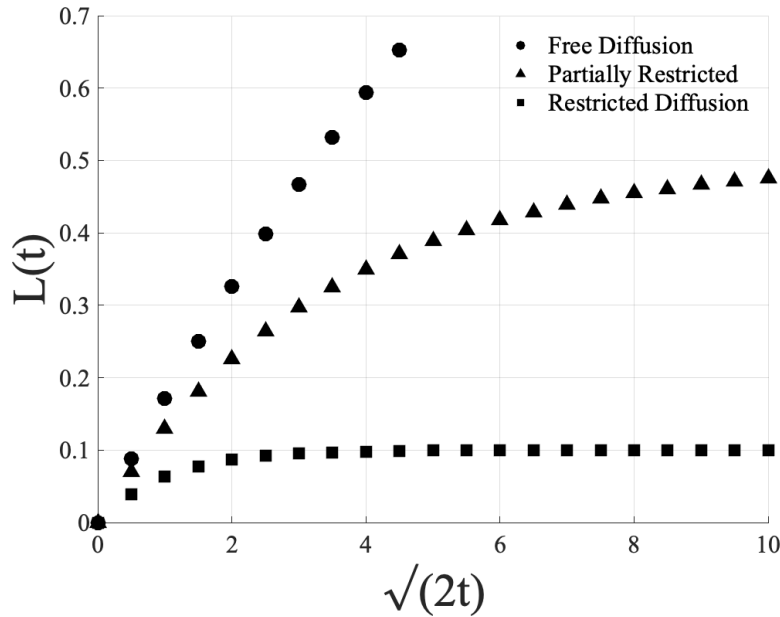


Figure 2.2: Demonstration of linear diffusion in the diffusion of a free particle; and, non linear diffusion in the diffusion of partial/completely restricted particles

2.2.3 Free, Partial & Completely Restricted Diffusion

In material science and medical imaging, studying diffusion patterns over time can reveal micro-structures of substances and tissues. Given if the microstructural configuration is restricting or not; or partially restricting, the diffusion length will vary in differentiating manner over time. Figure-2.2 illustrates three types of molecular diffusion.

For *free diffusion* (without any restriction) in the micro-domain, molecules move without significant obstacles, leading to a near-linear relationship between their displacement over time and the square root of time.

In *partially restricted* scenarios, molecules encounter some barriers, causing their displacement rate to increase more slowly compared to free diffusion, as indicated by the curve leveling off in Figure-2.2.

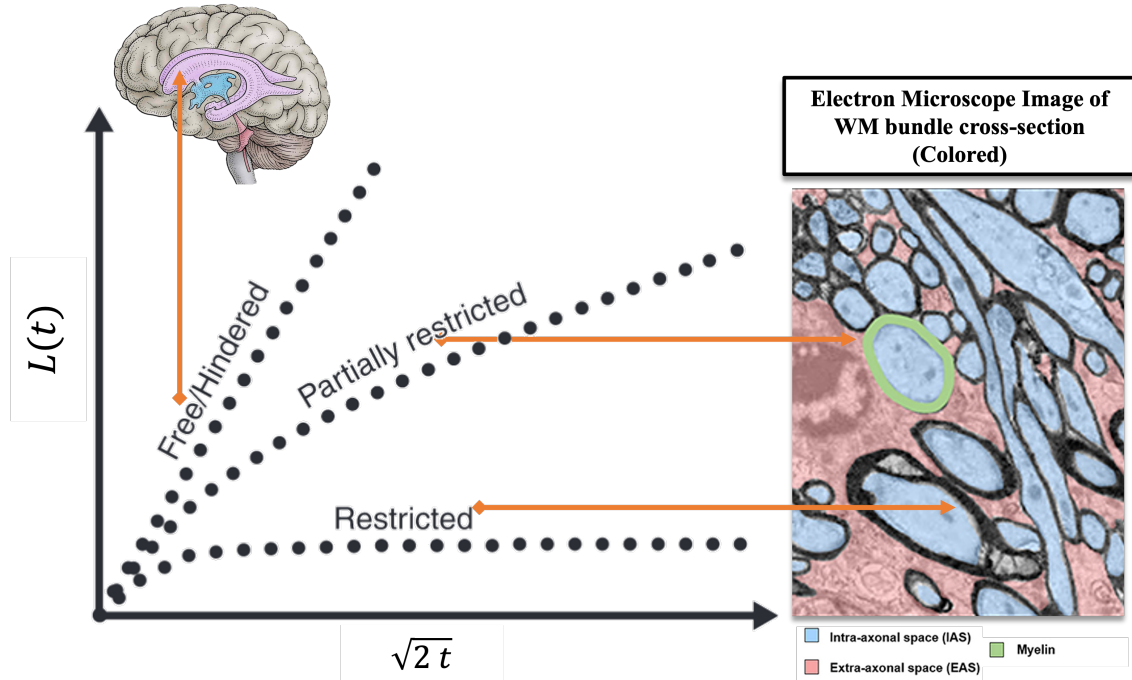


Figure 2.3: Schematic depiction of how different diffusion properties may appear in different tissue types in the brain. The scanning Electron Microscopic image was adapted from [19]

In *strictly restricting* micro-structures, molecules are confined within boundaries and their displacement over time plateaus, indicating they cannot move freely beyond certain limits.

2.2.4 Diffusion Reveals Microstructure

Human Brain and overall Body is almost 70-80% water which suggests, there is different distributions of restricted and non-restricted regions that will undergo diffusion differently over time. As water diffuses, it reveals the hidden landscape of tissue's inner structural integrity. The schematic figure-2.3 adapted from [18] shows how changing the diffusion pattern may detect pathogenesis and early structural changes in the human tissue.

This concludes the fundamental aspect of how diffusion can help in probing into the structural integrity of the tissue. But how can we measure diffusion in a non-invasive and safe manner? The answer lies with MRI. As MRI is sensitive to water contents in the tissue and this sensitivity can be controlled to instantiate diffusion in different directions.

2.3 Magnetic Resonance Imaging

2.3.1 Quick Introduction to MR

Magnetic Resonance Imaging is based on the quantum concept of NMR. This refers to protons absorbing energy at resonant frequency and then re-emitting the energy, a phenomenon first observed by Rabi and his team in 1938, when they measured the magnetic momentum of chemical elements. NMR was further explored in Bloch and Purcell's 1946 experiments. The critical development for MRI was the introduction of spatial encoding through magnetic field gradients, pioneered by Lauterbur and others. This innovation turned NMR from a physical phenomenon into the practical MRI systems used today in both clinical and scientific settings.

In the next sections, we cover the fundamentals of NMR in generating an MRI image. Initially, we explain how protons behave in a magnetic field and the methods for measuring their magnetic moments. Subsequently we detail the process of forming an MRI image.

2.3.1.1 NMR Basics

In the field of NMR, understanding the Larmor frequency is fundamental. It starts with a charged proton, which spins around its axis, creating a property known as

spin, represented by \vec{J} . This spin is intrinsically linked to a magnetic moment $\vec{\mu}$, a key feature of atomic nuclei. The magnetic moment and spin are related through the equation $\vec{\mu} = \gamma\vec{J}$, where γ is the gyromagnetic ratio, a unique characteristic of each type of nucleus.

The application of a strong external magnetic field, denoted by \vec{B}_0 , influences these magnetic moments. Under the influence of \vec{B}_0 , the magnetic moments $\vec{\mu}$ undergo precession, a type of rotational movement. This precession leads to the establishment of a net magnetization \vec{M} in the sample, which aligns with the magnetic field's direction.

In NMR analysis, we often define the direction of \vec{B}_0 as the z-axis. Consequently, terms like “longitudinal” refer to alignment along this z-axis, while “transverse” refers to orientations in the perpendicular xy-plane. Continuous exposure of the sample to \vec{B}_0 results in full magnetization, aligning the net magnetization \vec{M} entirely with the external field. This state maximizes longitudinal magnetization while eliminating any transverse magnetization.

Larmor frequency, denoted as ω , characterizes the rate of precession of the magnetic moments and is given by the formula:

$$\omega = \gamma|\vec{B}| \quad (2.4)$$

Here, \vec{B} represents the external magnetic field. This pivotal equation reveals that the Larmor frequency is a function of both the field strength $|\vec{B}|$ and the gyromagnetic ratio γ of the nucleus. For example, in hydrogen atoms of water molecules placed in a 1.5T, 3T and 7T magnetic field, the Larmor frequency is approximately 64, 128 and 298.67MHz respectively.

2.3.1.2 Inside the Magnet: Net Magnetization Detection

To detect the net magnetization vector \vec{M} , we consider its weak signal along the z-axis, aligned with the primary magnetic field. Detection requires rotating \vec{M} away from the z-axis using a Radiofrequency (RF) pulse. This causes \vec{M} to realign with the z-axis post-excitation, generating a detectable signal. The rotation angle is known as the flip angle, often set at 90 degrees.

The protons lose energy post-excitation, causing \vec{M} to reorient towards the z-axis, leading to two relaxation phenomena: spin-lattice relaxation along \vec{B}_0 and spin-spin relaxation perpendicular to \vec{B}_0 . T1 and T2 relaxation times vary across different tissues, influenced by their composition and the external magnetic field.

The relaxation dynamics follow the Bloch equations:

$$\frac{d\vec{M}}{dt} = \gamma\vec{M} \times \vec{B} - \frac{M_x\hat{i} + M_y\hat{j}}{T2} - \frac{M_z - M_0}{T1}\hat{k} \quad (2.5)$$

Here, M_0 is the equilibrium value of M_z , $\gamma\vec{M} \times \vec{B}$ denotes precession, $T1$ is the spin-lattice relaxation time, and $T2$ is the spin-spin relaxation time.

Spin-Lattice Relaxation: This process describes the exponential recovery of longitudinal magnetization. The equation for spin-lattice relaxation is:

$$M_z(t) = M_0 \left(1 - e^{-\frac{t}{T1}}\right) \quad (2.6)$$

Spin-Spin Relaxation: Known as transverse relaxation, this is represented mathematically in a uniform field B_0 as:

$$M_{xy}(t) = M_{xy}(0)e^{-\frac{t}{T2}} \quad (2.7)$$

In practical MRI with inhomogeneous external fields, the decay of transverse magnetization is characterized by $T2^*$, which is shorter than $T2$. The equation including this extra dephasing is:

$$M_{xy}(t) = M_{xy}(0)e^{-\frac{t}{T2^*}} \quad (2.8)$$

2.3.2 MR Image Generation

In order to generate MR image, the fundamental goal is 3D spatial encoding, which will generate a signal that inherently contains positional information. This process is broadly divided into two stages; Firstly, selecting a specific slice of the object in z-axis, and Secondly, pinpointing locations within that slice (xy-plane).

2.3.2.1 Slice Selection

As previously discussed, there's a direct correlation between the Larmor frequency of a proton and the strength of the external magnetic field. By applying a z-axis gradient \vec{G}_z , the Larmor frequency ω for each slice can be expressed as:

$$\omega = \gamma(B_0 + z|\vec{G}_z|) \quad (2.9)$$

Adjusting the RF pulse frequency allows for the selective excitation of protons in a specific slice by matching their Larmor frequency, which varies across the body due to the applied magnetic field gradient. This is the essence of slice selection in MRI.

2.3.2.2 Spatial Encoding within a Slice

To accurately encode positions within a slice, we employ a combination of frequency and phase encoding techniques. Frequency encoding is akin to the slice selection process. In contrast, phase encoding assigns unique phases to protons at different

locations by applying a gradient in phase encoding. Typically, this phase-encoding gradient is activated post slice selection and prior to frequency encoding, and the frequency encoding gradient is applied during signal measurement.

For instance, applying a y-axis gradient \vec{G}_y for a duration τ alters the phase ϕ of magnetization along the y-axis, which remains constant upon deactivation of \vec{G}_y :

$$\phi = \gamma |\vec{G}_y| y \tau \quad (2.10)$$

Similarly, applying an x-axis gradient \vec{G}_x causes the Larmor frequency to vary along the x-axis:

$$\omega = \gamma |\vec{G}_x| x \quad (2.11)$$

In summary, during and after the RF pulse, gradient magnets are used to create slight variations in the magnetic field at different locations within the body. These gradients are applied in three dimensions (x, y, and z axes) and allow each point in the body to have a unique frequency or phase. This spatial encoding is essential for determining from where in the body the MR signals originate. The reader is encouraged to watch the video cited on MRI signal localization to visualize the process [20].

2.3.2.3 K-Space to Anatomical Image Reconstruction

With the application of RF pulses, the hydrogen atoms emit signals as they return to their original state. These signals are detected and the combination of phase and frequency encoding allows for the determination of the origin of the signals in two dimensions within the selected slice. These signals are then placed into a spatial frequency domain known as k-space. Each signal fills a different part of k-space, with

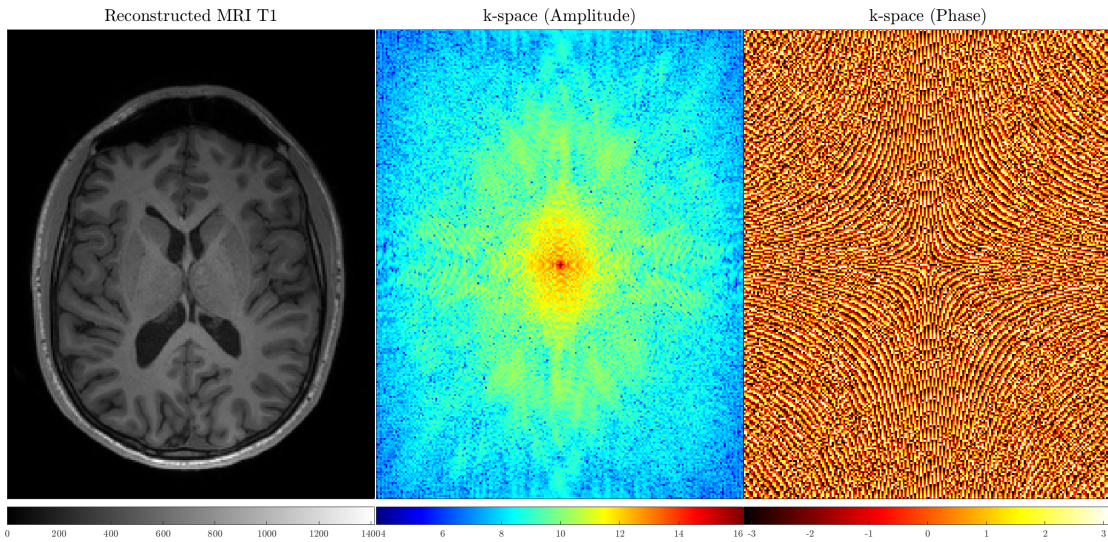


Figure 2.4: Example MRI T1 magnitude reconstructed from the sampled complex MRI signals on the k-space, shown as Amplitude and Phase (in radian)

different gradients contributing to different parts of k-space. The entire k-space must be filled to produce an image.

Once k-space is fully sampled with complex MR signals (with amplitude and phase shown in figure-2.4), it is reconstructed to spatial images using fourier transform. This transformation translates the complex frequency amplitude and phase (radian) information into a gray-scale image that represents the anatomy that radiologists can interpret. These images can be manipulated for better visualization and are often used for diagnostic purposes.

2.4 Encoding Diffusion using MRI

The discovery of MRI sensitivity to molecular self-diffusion dates back to 1950, when Hahn observed a signal reduction while using the Spin Echo (SE) sequence [21]. He proposed the idea that the diffusion coefficient could be measured. It wasn't until 1954, however, that Carr and Purcell [22] utilized Hahn's spin-echo sequence to create

a method for measuring this phenomenon. They observed that the magnitude of the SE signal is notably affected by random molecular diffusion. In 1956, these effects were incorporated into the Bloch Equation-2.5, creating the Bloch-Torrey Equation [23]:

$$\frac{d\mathbf{M}}{dt} = \gamma(\mathbf{M} \times \mathbf{B}_0) - \begin{pmatrix} \frac{M_x}{T_2} \\ \frac{M_y}{T_2} \\ \frac{M_z - M_0}{T_1} \end{pmatrix} + D\nabla^2\mathbf{M} \quad (2.12)$$

In this context, \mathbf{M} denotes the magnetization of a sample subjected to a static magnetic field \mathbf{B}_0 . The gyromagnetic ratio is represented by γ , and M_x, M_y, M_z symbolize the magnetization components along the x, y, and z axes, respectively. M_0 refers to the sample's magnetization under thermal equilibrium. T_1 and T_2 are identified as the longitudinal and transverse relaxation times, respectively, while D stands for the diffusion coefficient. The initial two components of Equation-2.12 originate from the original Bloch Equation, as noted in reference [23]. The third segment of Equation 2.12 is an addition made by Torrey. In terms of the Bloch-Torrey equation (Equation 1), the solution for magnetization within the transverse plane ($M_{xy} = M_x + iM_y$) post a 90° pulse is expressed as:

$$M_{xy} = M_0 e^{-\frac{t}{T_2}} e^{-bD} \quad (2.13)$$

$$S(0) = M_0 e^{-\frac{t}{T_2}} \quad (2.14)$$

Following this, in the 1960s, Stejskal and Tanner [24] developed the Pulsed Gradient Spin Echo (PGSE) sequence, characterized by short-duration gradient pulses.

The PGSE sequence operates on the principle that the gradient pulse duration (δ) is significantly shorter than the spacing between the two gradients (Δ). The net phase

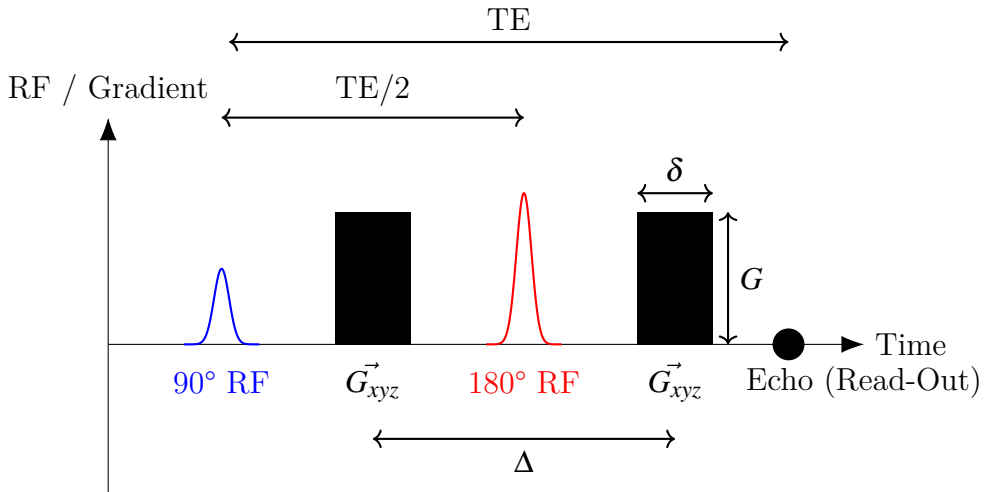


Figure 2.5: Schematic diagram of timing in PGSE sequence

difference of spins between these two gradients is dependent on their positions at two distinct time points. If the spins move during the interval between these gradient pulses, the resultant signal is weaker compared to when the spins remain stationary. The signal measured in diffusion MRI using the PGSE sequence is formulated as:

$$S(\vec{q}) = S(0) \int p(\vec{r}) e^{-i\vec{q} \cdot \vec{r}} d\vec{r} \quad (2.15)$$

In this equation, $S(\vec{q})$ and S_0 represent the signals acquired with and without the diffusion weighting gradients, respectively. Here, $p(\vec{r})$ is the probability density distribution of water molecule displacements, \vec{q} is defined as $\gamma\delta\vec{G}$, and \vec{r} denotes the diffusion displacement between the two diffusion-encoding gradient pulses.

2.4.1 Diffusion Gradient, Time & b-value

The “b-value” or “b factor” is a critical parameter in MRI for characterizing diffusion sensitivity [25, 26]. This factor, also known as the diffusion weighting factor, is

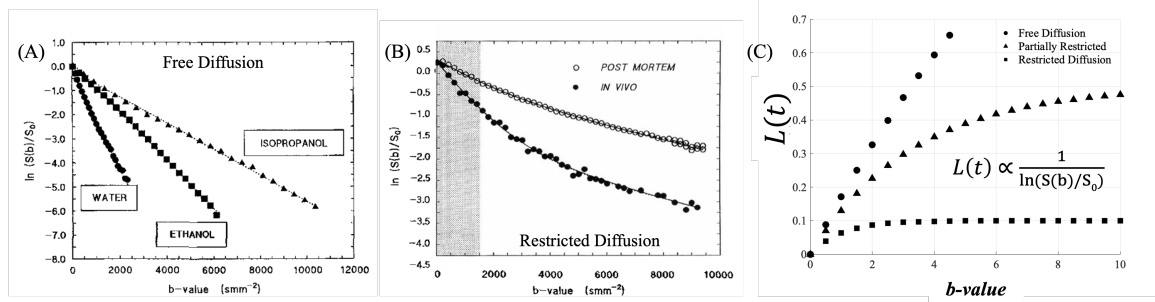


Figure 2.6: Diffusion Length is inversely proportional to the diffusion signal from dMR. (A) and (B) adapted with permission from *John Wiley and Sons* [28]. (C) Demonstrates the non-linear relationship still holds for increasing b-value in partial/restricting compartments for Diffusion Length.

expressed as:

$$b = q^2 \left(\Delta - \frac{\delta}{3} \right) = (\gamma \delta G)^2 \left(\Delta - \frac{\delta}{3} \right) \quad (2.16)$$

This relationship holds true specifically when δ is considerably smaller than Δ in a single diffusion encoding scenario. The more generalized definition of the b value is given by:

$$b = \gamma^2 \int_0^t \left| \int_0^{t'} G^*(t'') dt'' \right|^2 dt' \quad (2.17)$$

Here, G^* represents the effective diffusion gradient. Further details about the underlying physics can be found in [27].

2.4.2 Diffusion b-vectors & Q-space

For applying controlled diffusion, the b-value parameters is an important scalar; But it doesn't account for controlling the direction of the diffusion applied on a tissue fragment. Also, to solve for Equation-2.13 we need to have at least a number of directions equal to the unknown parameters in diffusivity matrix, further explained in Section-3.2.1. The sampling directions can be represented as unit vectors on a sphere with unit radius, which is known as the Q-Space. The Q-space refers to a unit

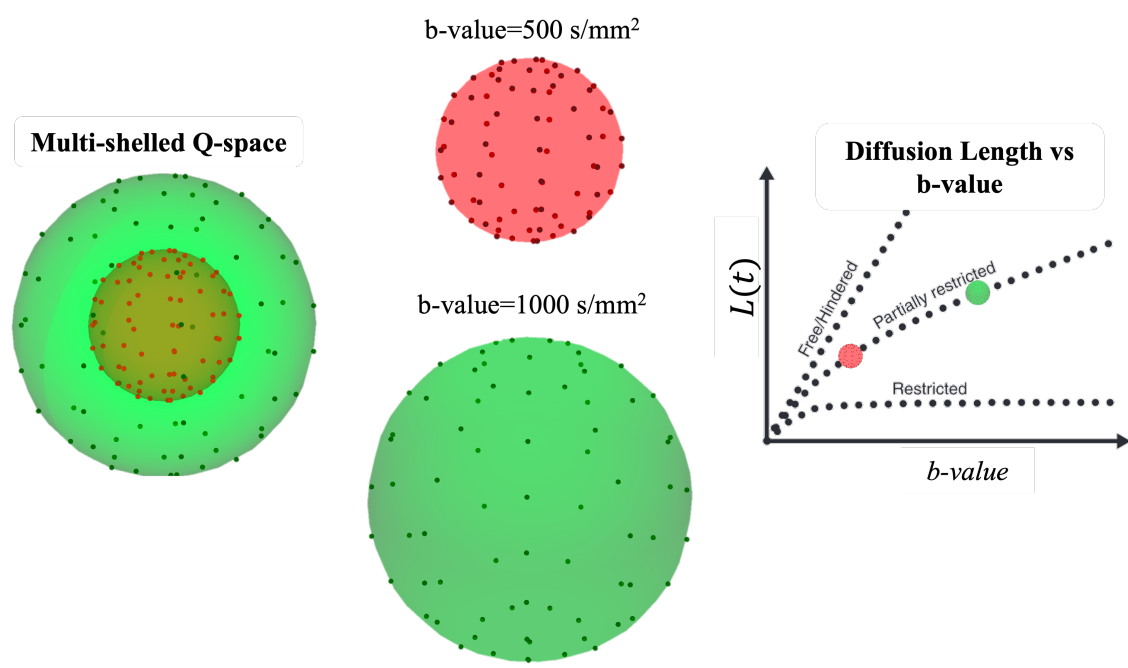


Figure 2.7: Multi-shelled Q-space in diffusion protocols, shown with their relationship to diffusion length.

$\text{SO}(3)$ sphere with a number of b-vector samples along which diffusion measurements are done. In summary, the b vector is the vector component of the applied b-value to sample a diffusion measurement. For uniform coverage on the Q-space, optimization techniques are recommended, which ensures reliable coverage to model the fiber orientation density [29].

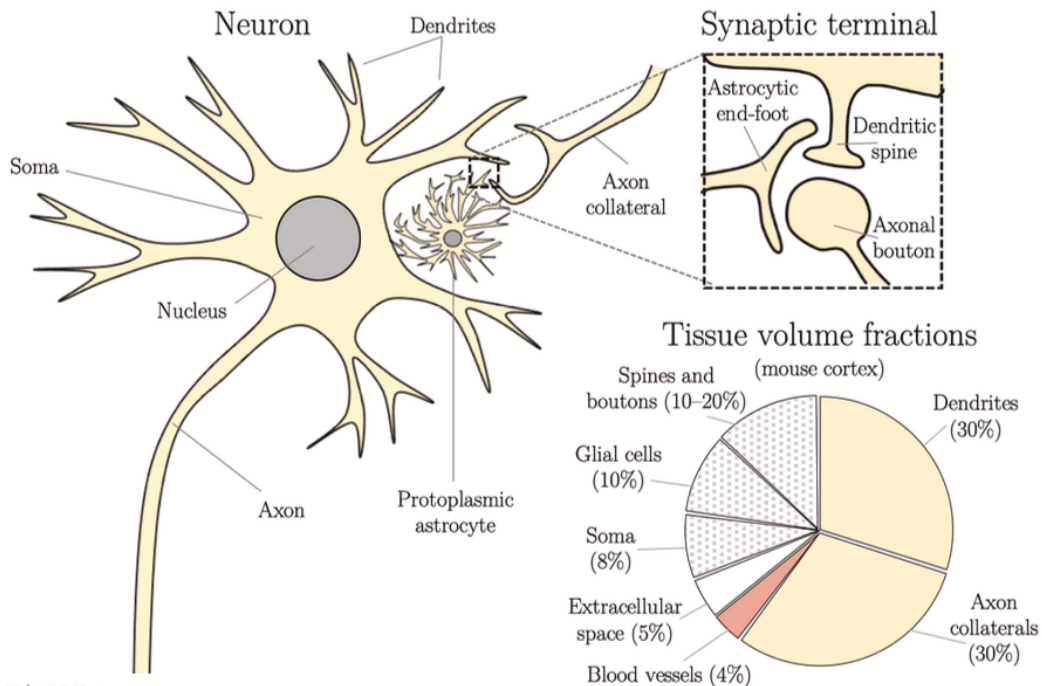
2.5 Human Brain

Depending on micro-structure of the underlying brain tissue, we would expect to observe different diffusion phenomena in these tissues. Since the brain can be grossly divided into two visibly different types of tissue, i.e. gray and white matter, this section aims to provide background information on their microstructural building blocks.

2.5.1 White Matter

White matter primarily consists of myelinated axons, which are composed of an internal space within the axon, encased by both an axonal membrane and myelin sheaths created by oligodendrocyte glial cells [31–34]. The size of this intra-axonal space varies, generally measuring between 0.2 and $10\mu\text{m}$ across in the human corpus callosum, typically around $0.6\mu\text{m}$ [31]. Oligodendrocytes, with a cell body diameter of $6\text{--}8\mu\text{m}$, extend several membranous processes that can form up to 60 myelin sheaths [32]. These sheaths are made of a repeatedly folded membrane, spiraling around the axon. This results in a compacted lipid layer and a thin water layer in between the membrane folds [33,34]. A single sheath can cover a length of 100–1700 μm along an axon, known as an internode, with nodes of Ranvier, measuring 1–5 μm wide, interspersed between them [33,34]. These nodes are in contact with fibrous

A) Gray matter



B) White matter

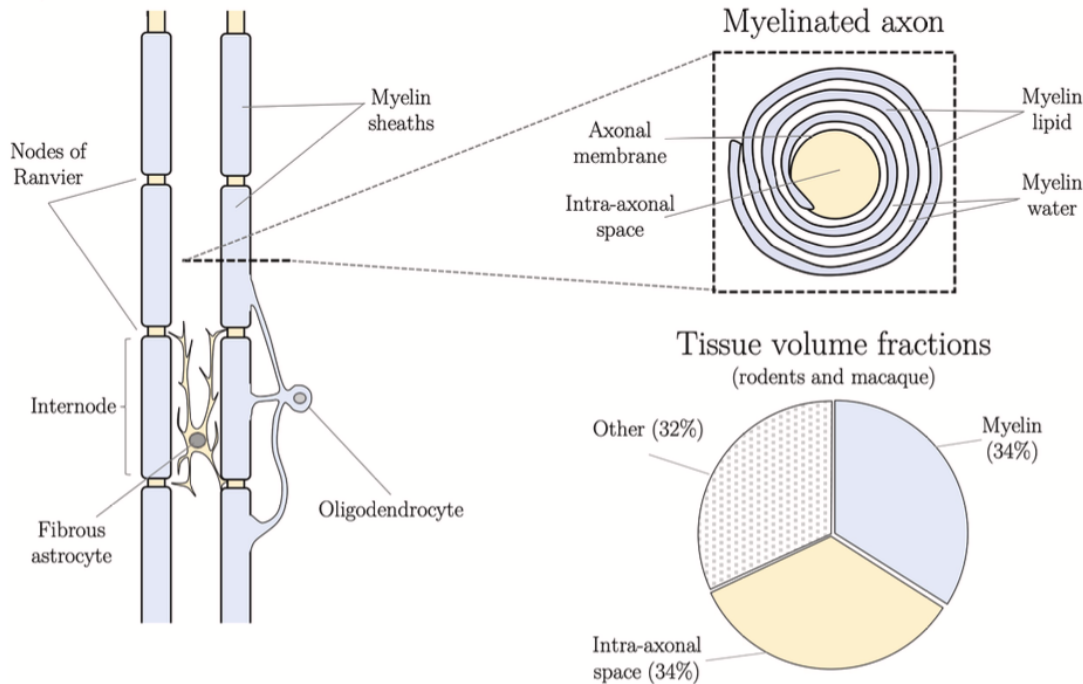


Figure 2.8: Micro-structure with relative tissue volume fractions of (A) Gray Matter and (B) White Matter adapted from [30].

astrocyte processes. Studies using electron and light microscopy on various animals, including guinea pigs, rats, macaques, and mice, have estimated the composition of white matter [35–38].

2.5.2 Gray Matter

The primary structure of gray matter is predominantly made up of neuron cell bodies, dendrites, unmyelinated axons, glial cells, and capillaries.

Neurons

Each neuron has a cell body, or *soma*, measuring 10 to 100 μm in diameter. These neurons feature multiple dendrites for receiving incoming signal and an axon for signal transmission.

Dendrites generally have a diameter of about 1 μm and extend to a length of 3 to 4 mm in a single neuron, divided across branching segments of 60 to 70 μm in length. Dendrites are covered with dense spines, they are tiny protrusions measuring 1 to 3 μm and characterized by a large head and thinner neck [39].

Un-myelinated Axons consist mostly of branching collaterals, varying in diameter from 0.3 to 1.6 μm , and ending in ‘boutons’ at their distal ends [40].

Synaptic Terminals

Synaptic terminals, the sites of electrochemical communication between neurons, are formed where the ending feet of protoplasmic astrocytes meet dendritic spines and axonal boutons [41].

2.5.3 Probing Brain Microstructure with dMRI

Using electron microscopy on mouse cortex and white matter tissue, the volume fractions of various microstructural components are measured and reported in Figure-2.8 [30].

For white matter, approximately two-thirds is made up of myelinated axons, evenly divided between the intra-axonal space and myelin. The rest of the white matter consists of various elements, including the intra-axonal space of unmyelinated axons, astrocyte and oligodendrocyte cells and processes, and a small percentage of extracellular space [35, 38]. Various diffusion models such as AxCaliber [42], NODDI [8, 12] has been proposed for neurite quantification.

In a multi-compartmental scenario, for cortices (gray matter), neurites occupy around two-thirds of the volume, evenly split between the axon and dendrites. The rest of the space is filled with 10–20% of axonal boutons and dendritic spines, 10% of astrocytes and other glial cells , around 8% soma, 5% extracellular space, and 4% blood vessels. [43–45]. Diffusion models are specifically designed with high b-values to characterize various elements of gray matter independently using Soma And Neurite Density Imaging. (SANDI) [46].

Additionally, according to imaging data, blood vessels constitute about 2–3% of white matter’s composition [47]. Recent advancement in Intravoxel Incoherent Motion (IVIM) based DTI show promise in quantifying perfusion for blood vessels in the brain [?, 48]. The generalized and specific models relevant to this thesis are organized in the next chapter and summarized in Table-3.2.

Chapter 3

General Models, AI & Analysis in dMRI

“All models are wrong, but some are useful.”

— George E. P. Box

3.1 Overview

In the previous chapter we have built on the physics of diffusion, MRI and encoding diffusion with MRI. In this chapter, we aim to highlight the required processing steps after data acquisition and approaches to model these signals using the context of Q-Space to be able to interpret micro-configuration of the tissue under investigation. Then the chapter discusses general Artificial Intelligence (Deep/Machine Learning) frameworks and strategies used in this thesis to infer brain microstructural configurations using such techniques. Since the data-driven strategies come with warnings, we highlight them and discuss the types of features that are appropriate to model diffusion MR signals.¹

¹This chapter was partly published in **Faiyaz, A.**, Doyley, M. M., Schifitto, G., & Uddin, M. N. (2023). *Frontiers in Neurology*, 14, 116833.

3.2 Representing Diffusion MR Signals

Sparse diffusion signals need to be summarized in order to get meaningful diffusion parameters. Through diffusion we generally investigate the directionality and how anisotropic the diffusion process was in the tissue. This is well achieved by mathematically modeling the signals. Mathematical modeling includes modeling the diffusion process on the Q-space using a 2D tensor (Section-3.2.1) and spherical harmonic basis representation through Constrained Spherical Deconvolution (Figure-5.4).

Advanced characterization of diffusion signal is also possible by using biophysical representation, which takes a practically useful approach in modeling brain tissue compartments.

In short, mathematical representations are formulas, and biophysical models are pictures. [2]

3.2.1 Mathematical modeling

For the PGSE protocol highlighted in Section-2.4, solution to Equation-2.15 can be written simply as follows

$$S = S_0 e^{-bg^T D g} \quad (3.1)$$

where, S_0 refers to T2-weighted measure for reference, b as b-value and g as b-vector. To summarize diffusion in 3-dimension, the D matrix is defined as the 2D tensor.

Diffusion Tensor Imaging

DTI is a specialized form of MRI that captures the directional movement of water molecules in tissue, based on the principles of diffusion and the assumption of Gaussianity in the diffusion process.

1. Tensor Matrix (D):

$$D = \begin{bmatrix} D_{xx} & D_{xy} & D_{xz} \\ D_{xy} & D_{yy} & D_{yz} \\ D_{xz} & D_{yz} & D_{zz} \end{bmatrix}$$

This equation represents the diffusion tensor matrix D , which is a 3×3 symmetric matrix. The elements of the matrix ($D_{xx}, D_{xy}, D_{xz}, D_{yy}, D_{yz}, D_{zz}$) represent the diffusion coefficients along and across different axes (x, y, z). This matrix is key in DTI, as it characterizes the diffusion of water molecules in tissue, which is anisotropic in biological tissues like brain white matter.

2. Least Squares Fit (f_{LLS}):

$$f_{LLS}(\gamma) = \frac{1}{2} \sum_{i=1}^n \left(y_i - \sum_{j=1}^7 W_{ij} \gamma_j \right)^2$$

This equation is used in the context of linear least squares fitting. Here, f_{LLS} is a function representing the sum of squared differences between observed values (y_i) and values predicted by a linear model. W_{ij} are weights and γ_j are model parameters. This method is often used in DTI to solve for the tensor elements.

3. Tensor Decomposition:

$$D = \begin{bmatrix} D_{xx} & D_{xy} & D_{xz} \\ D_{yx} & D_{yy} & D_{yz} \\ D_{zx} & D_{zy} & D_{zz} \end{bmatrix} = [\vec{v}_1 \vec{v}_2 \vec{v}_3] \begin{bmatrix} \lambda_1 & 0 & 0 \\ 0 & \lambda_2 & 0 \\ 0 & 0 & \lambda_3 \end{bmatrix} [\vec{v}_1 \vec{v}_2 \vec{v}_3]^{-1}$$

This equation shows the eigenvalue decomposition of the diffusion tensor. The matrix D is decomposed into eigenvectors (v_1, v_2, v_3) and eigenvalues ($\lambda_1, \lambda_2, \lambda_3$). The eigenvectors represent the principal directions of diffusion, and the

eigenvalues represent the magnitude of diffusion in those directions.

Computing DTI Metrics

Tensor decomposition leads to computation of DTI metrics, designed specifically to study the characteristics of Gaussianity of the 2D tensor.

1. Fractional Anisotropy (FA):

$$FA = \sqrt{\frac{(\lambda_1 - MD)^2 + (\lambda_2 - MD)^2 + (\lambda_3 - MD)^2}{2(\lambda_1^2 + \lambda_2^2 + \lambda_3^2)}}$$

FA measures the degree of diffusion anisotropy. It's a scalar value between 0 and 1, indicating how directional the water diffusion is. A high FA value indicates that diffusion is highly directional (anisotropic), common in areas like white matter tracts.

2. Axial Diffusivity (AD):

$$AD = \lambda_1$$

AD refers to the diffusion along the principal axis of diffusion. It's simply the first eigenvalue (λ_1) of the diffusion tensor and represents diffusion along the main direction of fibers, such as nerve axons in the brain.

3. Mean Diffusivity (MD):

$$MD = \frac{\lambda_1 + \lambda_2 + \lambda_3}{3}$$

MD is the average of the eigenvalues and represents the average diffusion rate irrespective of direction. It's a measure of the overall mobility of water molecules.

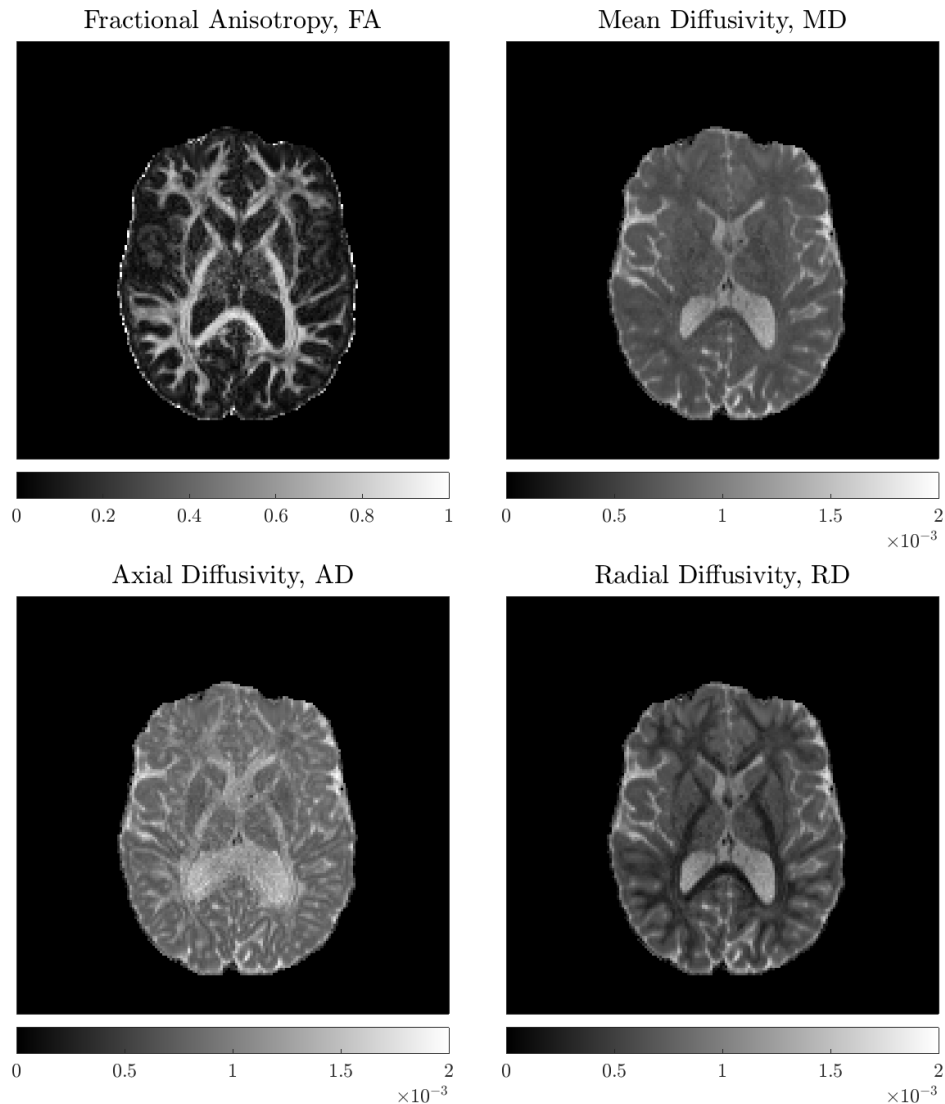


Figure 3.1: Example of diffusion scalar maps (FA, MD, AD, RD) derived from fitted diffusion tensors.

4. Radial Diffusivity (RD):

$$RD = \frac{\lambda_2 + \lambda_3}{2}$$

RD represents diffusion perpendicular to the principal diffusion direction and is the average of the second and third eigenvalues. It's particularly useful in assessing myelin integrity in nerve fibers.

In summary, these equations form the mathematical foundation for analyzing and interpreting the data obtained from DTI scans, which are crucial in studying brain tissue, particularly white matter structures.

3.2.2 Biophysical modeling

Neurite Orientation Dispersion & Density Imaging

DTI fitting assigns one apparent diffusion coefficient (ADC) for a single voxel while the NODDI tissue model hypothesizes three different micro-environments, where the ADC in each hypothesized compartment is different. So, for an MR signal in a given voxel, the associated micro-environments are extracellular, intra-cellular and free-standing water in different configurations. The related diffusion coefficients for three compartments are intrinsic parallel diffusivity (d_{\parallel}), perpendicular diffusivity (d_{\perp}) and isotropic diffusivity (d_{ISO}). In the NODDI model, the diffusivities are assumed to be fixed in-vivo [42, 49]: $d_{\parallel} = 1.7 \times 10^{-3} \text{ mm}^2 \text{s}^{-1}$ and $d_{ISO} = 3.0 \times 10^{-3} \text{ mm}^2 \text{s}^{-1}$, whereas the perpendicular diffusivity d_{\perp} is related to NDI and d_{\parallel} by the mean-field tortuosity model as $d_{\perp} = (1 - NDI)d_{\parallel}$. Therefore, the NODDI tissue model is stated as-

$$A_Q = (1 - f_{ISO})(NDI \cdot A_{IC} + (1 - NDI) \cdot A_{EC}) + f_{ISO}A_{ISO} \quad (3.2)$$

where Neurite Density Index (NDI) is defined as Neurite Density Index which is

the intracellular volume fraction and Fractional Isotropy or Free Water (f_{ISO}) is the fractional isotropy or free water. For the intracellular (IC) compartment,

$$A_{IC} = \int_{S^2} f_M(\vec{n}) e^{-bd_{||}(q \cdot n)^2} d\vec{n} \quad (3.3)$$

where b = b-value, q = b-vector, n = samples of directions on a sphere on which the integration is done. Probability of finding orientation directed along n when μ and κ is known,

$$f_M(\vec{n} | \vec{\mu}, \kappa) = M \left(\frac{1}{2}, \frac{3}{2}, \kappa \right)^{-1} e^{\kappa(\vec{\mu} \cdot \vec{n})^2} \quad (3.4)$$

where M is defined as Kummer's confluent hypergeometric function. For the extracellular (EC) compartment,

$$A_{EC} = e^{-bqq^T D_{EC}(f, NDI)q} \quad (3.5)$$

$$D_{EC}(f, NDI) = \int f_M(\vec{n}) D_h(\vec{n}, NDI) d\vec{n} \quad (3.6)$$

Details for Equation (3.5) and (3.6) can be found in the previous report [8].

For the isotropic compartment,

$$A_{ISO} = e^{-b.d_{ISO}} \quad (3.7)$$

ODI is dependent on κ , known as the concentration parameter associated with the Watson distribution defined in Equation 3.4 and calculated as follows

$$ODI = \frac{2}{\pi} \arctan \left(\frac{1}{\kappa} \right) \quad (3.8)$$

We use multi-shell protocol with ground-truth parameters to synthesize the diffusion weighted signal based on the defined model and Rician noise with signal to noise

ratio (SNR) of 20 dB is added to the synthesized signal.

3.2.2.1 Multi-parameter Visualization of NODDI

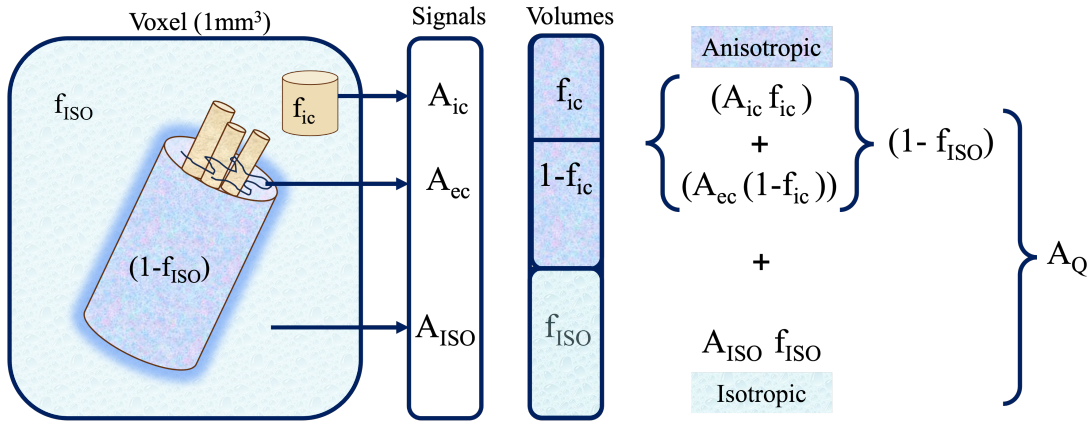
The NODDI model focuses on the estimation of the following parameters:

Neurite Density Index(NDI): This parameter quantifies the volume fraction of the intracellular space, so it is also termed as intracellular volume fraction Intra-Cellular Volume Fraction (ICVF), reflecting the density of neurites (axons and dendrites) in brain tissue. A higher NDI/ICVF indicates a higher density of neurites.

Orientation Dispersion Index (ODI): ODI measures the dispersion of neurite orientations within a voxel. It reflects the degree of alignment or coherence of neurites. A low ODI indicates highly aligned neurites, whereas a high ODI suggests more dispersed or isotropic orientations.

Free Water (f_{ISO}): This parameter represents the fraction of the diffusion signal that is isotropic, which is often attributed to extracellular and/or Cerebro Spinal Fluid spaces, so this is also termed as Fractional Isotropy or Isotropic Volume Fraction. It can provide insights into changes in the brain's extracellular environment.

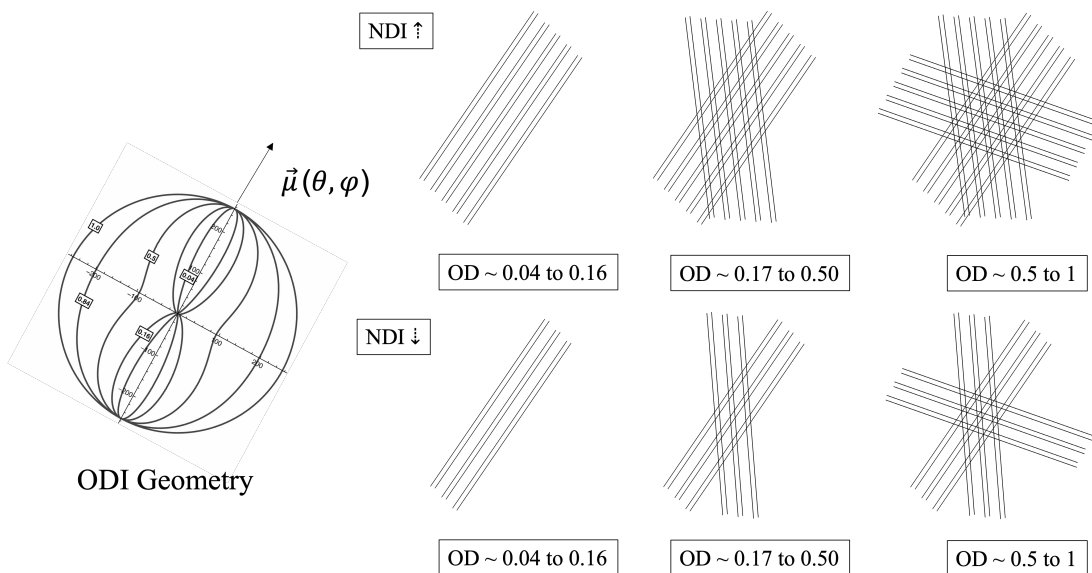
These parameters together provide a more comprehensive understanding of the brain's microstructural environment compared to conventional DTI, which primarily focuses on overall diffusion magnitude and directionality. NODDI's ability to differentiate between neurite density and orientation dispersion makes it a valuable tool in neuroscience and clinical research, particularly in studies related to brain development, aging, and neurodegenerative diseases. To accommodate combined visualization of these three parameters, we can use the Hue, Saturation and Intensity Value (HSV) colorspace in the following order where Hue represents f_{ISO} , Orientation Dispersion is shown with Saturation and NDI is characterized with Intensity Value(V), the colormap is further shown in Figure-3.3(B,C). Figure-3.3A shows com-



f_{ic} = NDI = Intracellular Volume fraction or Neurite Density Index

f_{ISO} = Free Water Volume Fraction

(a) Compartmental volume fractions of NODDI, i.e.. NDI and f_{ISO}



(b) Geometrical parameter (i.e. ODI) of NODDI in higher and lower NDI conditions. ODI Geometry is adapted from [8]

Figure 3.2: Schematic diagram for Neurite Orientation Dispersion and Density Model.

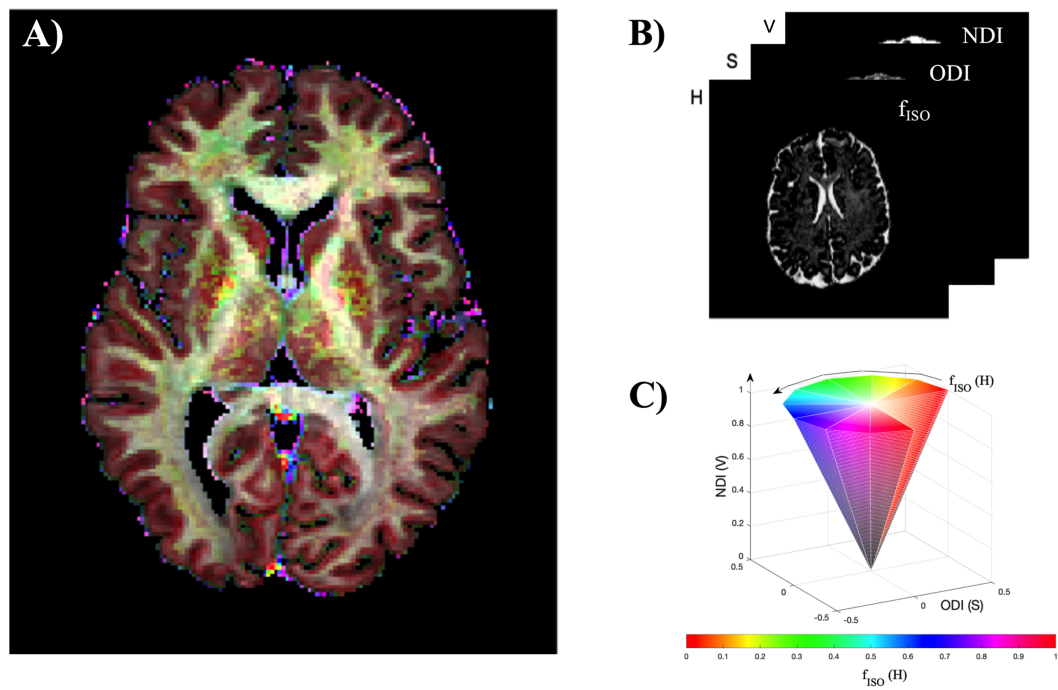


Figure 3.3: A) NODDI parameters (f_{ISO}, ODI, NDI) in combined HSV colorspace. B and C illustrates the color-map depiction.

bined parameters of NODDI in HSV space generated through plot-noddi-combined.m function here.

3.3 Artificial Intelligence (DL/ML) for dMRI

The fuel of data-driven AI models are clean data. At first, the data is curated and prepared for feature extraction. Based on the learning objective and data structure itself, feature engineering is done, which plays an important role in the learning process. Learning process also relies on the optimization criteria used, training model and evaluation function. For clinical data such as dMRI, clinical evaluation must be taken under consideration. Figure-3.4(A) illustrates the three fundamental components used to extract microstructure from scanner-derived dMRI data: a mathematical or biophysical model, an optimization algorithm, and an objective function. These components are essential for voxel or volume-wise processing of DW data. Historically, before the rise of DL tools, algorithms such as Gradient Descent, Newton's method, and the Levenberg-Marquardt algorithm were widely used for solving inverse problems [50]. These algorithms typically utilized objective functions designed to mimic the noise distribution in the data, such as Gaussian or Rician noise commonly found in MRI. The objective was often to maximize the log-likelihood of the measured DW data considering these noise distributions. Additionally, in some instances, the problems were reformulated within a sparse dictionary framework [51], and regularization terms were frequently added to the objective functions to address the challenges posed by ill-posed problems. Regularization techniques such as Lasso (L1), Ridge (L2), and Tikhonov were employed to stabilize these problems [51–53]. One limitation of the maximum likelihood estimation (MLE) frameworks was their tendency to converge to local minima, heavily influenced by the initial parameters set for the biophysical

Feature Type	Methods	Specialty
Sparse	MLP	Maps Sparse inputs to Sparse outputs
Spatial 2D/3D/4D	CNN	Extract spatial features to map to an output
	AutoEncoders	Extract spatial features in a unsupervised manner
	U-Net (Supervised AutoEncoder)	- Extract Spatial features in supervised task to map output to an image
Sequential	RNN	Short-term memory mapped to an output
	LSTM	Long- and short term memory mapped to an output
	Transformers	Attention to map a sequence to an output

Table 3.1: Classification of fundamental AI architectures with feature types.

model [8, 54]. To address this, grid search methods were commonly used to find a suitable starting point, though these methods were computationally intensive [55, 56]. Despite reducing computational redundancy, sparse dictionary representation of such models often compromised accuracy [51].

The field of imaging reconstruction, particularly the use of optimizers, is increasingly embracing DL/ML techniques (as shown in Figure-3.4D). A significant benefit of these techniques is their ability to generalize, though this is not without inherent biases [11]. Nevertheless, promising strategies have emerged to mitigate these biases. One such strategy is Data Engineering, which aims to minimize training-data bias by enhancing data priors. This is achieved either by leveraging problem geometry or by utilizing different available modalities as priors, a process akin to 'prior regularization'. This approach not only helps in moving solutions away from local minima but also improves objective values and reduces bias. This improvement is particularly notable when the starting points for MLE are determined through adapted multi-layer

perceptrons (MLP) [12, 54].

The utilization of DL/ML architectures is growing, but the field faces challenges in standardizing nomenclature and identifying underlying generic architectures. Monitoring these architectures is vital due to their specific limitations and the distinct biases they introduce. For instance, CNN/U-net/GAN architectures tend to create complex structures that might be clinically misleading [53, 57–59], while general MLPs, when overparameterized with noise, tend to produce outcomes that average the training data [11].

3.3.1 General AI (DL/ML) Models

The landscape of Artificial Intelligence, particularly in Deep Learning (DL) and Machine Learning (ML), is marked by a variety of architectures, each specialized for handling different types of features. These architectures have been introduced over time, reflecting the evolution of the field.

1. Sparse Feature Processing:

Multi-Layer Perceptron (MLP): This architecture is designed to handle sparse inputs and map them to sparse outputs. The strength of MLP lies in its ability to process features that have a large number of dimensions but are sparsely populated, making it effective for tasks like recommendation systems.

2. Spatial Feature Processing (2D/3D/4D):

Convolution Neural Network (CNN): Introduced in the 1980s with significant developments in the 1990s, CNNs are adept at extracting spatial features from images or video data. They map these features to an output, making them pivotal in image and video recognition tasks.

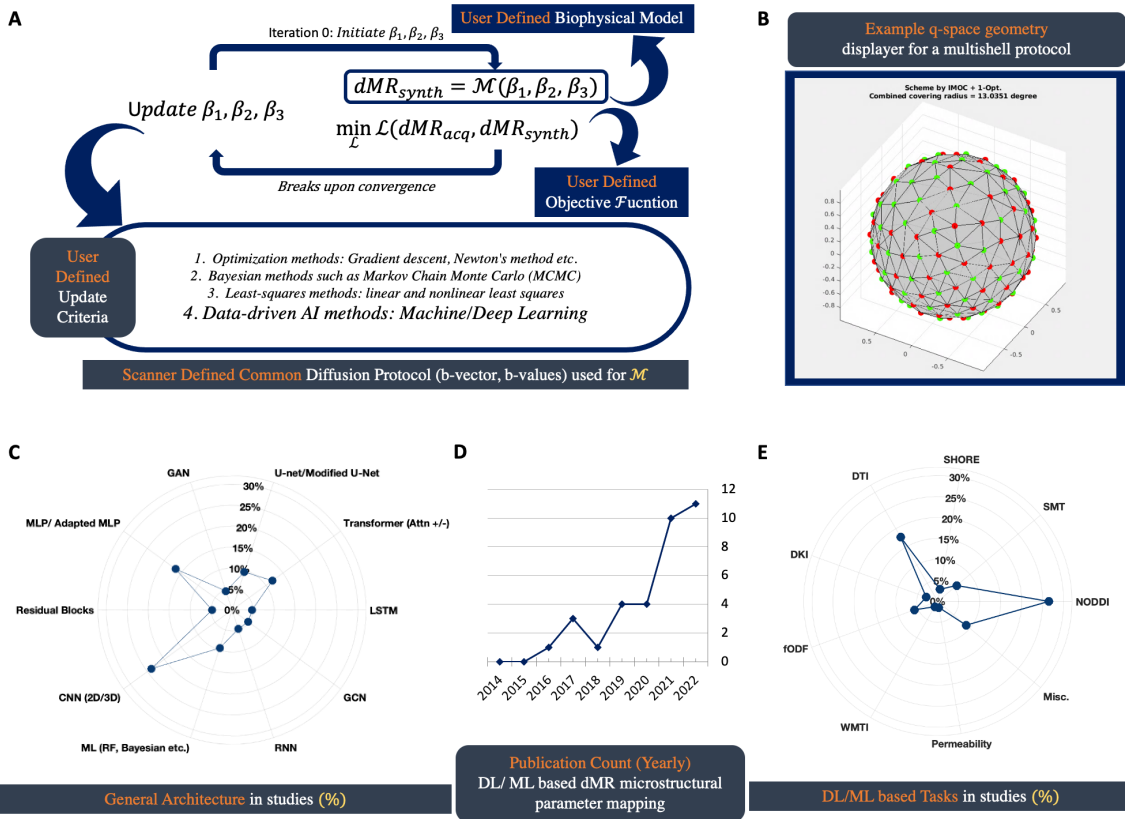


Figure 3.4: dMRI based microstructural reconstruction in human brain: Schematics & Progress through AI: A) general schematics of microstructural reconstruction using biophysical model; B) Multishell diffusion protocol in q-space. C) shows radial summary of types of architectures AI approaches use; D) displays the number of AI approaches proposed over the last decade; E) shows the radial summary of biophysical models these AI approaches are applied to.

AutoEncoders: These are used for unsupervised learning of efficient codings. They are particularly useful for dimensionality reduction and feature learning in spatial data.

U-Net (Supervised AutoEncoder): An advancement in the AutoEncoder design, the U-Net architecture is specialized for image segmentation tasks. It's designed to work in a supervised learning setting, providing precise mapping from spatial features to segmented images.

3. Sequential Feature Processing:

RNN (Recurrent Neural Networks): RNNs, introduced in the 1980s, are designed to handle sequential data with short-term memory, mapping sequences to outputs. They have been fundamental in processing time-series data.

LSTM (Long Short-Term Memory): An extension of RNNs, LSTMs were introduced in 1997 to overcome the limitations of RNNs in handling long-term dependencies. They are effective in sequential tasks that require understanding both long-term and short-term dependencies.

Transformers: Introduced in 2017, Transformers marked a significant shift in handling sequential data. Unlike RNNs and LSTMs, Transformers use attention mechanisms to map sequences to outputs. They have been revolutionary in natural language processing tasks.

Each of these architectures has contributed to the advancement of AI, addressing specific challenges and paving the way for sophisticated applications in various fields such as natural language processing, computer vision, and beyond.

Combinatorial Approaches in AI Architectures: Alongside these individual models, there is an increasing trend in combining different architectures to leverage

the strengths of each for more complex tasks. These hybrid models integrate various architectures like CNNs with LSTMs or Transformers with AutoEncoders, enabling them to process multiple feature types simultaneously. This approach enhances the model's capability to understand and interpret complex data that exhibits a combination of spatial, sequential, and sparse features. Such integrations are pushing the boundaries of AI applications, allowing for more nuanced and sophisticated data analysis and interpretation.

3.3.2 AI(DL/ML) Strategies for Microstructure Reconstruction

Based on how the DL/ML algorithms are applied to analyze dMRI data, we have divided them into three categories found in Table-3.2(Block B, C and D).

3.3.2.1 AI Agnostic to Q-Space Features

First category of AI algorithms focuses on direct DWI signal mapping, and is generally agnostic to q-space geometry or how the sampling scheme is oriented for the signal. Some of these algorithms are analogous to the Natural Language Processing (NLP) algorithms which are often used in speech data processing. Examples include Recurrent Neural Network (RNN), Long Short-Term Memory (LSTM), Generative Adversarial Networks (GAN), Attention mechanisms, etc [97–100]. The Memory/Forget block in some of these architectures allows for the development of signal orientation priors that are not directly sensitive to the geometry of the sampling scheme [87]. It is not impossible that these artificially generated priors might be misleading when there is substantial noise [53]. As it has been noted in the literature that with lower SNR, the AI algorithms are more prone to training data bias [11].

Block A: Neuro-biophysical Models with Key Parameters			Block B: AI Agnostic to Q-Space Geometry		
Biophysical Models	Protocol feasibility	Microparameters	AI Models	General Architecture	Task
2009 FWI [60]	Single/Multishell	FW, FWE-DT	2022 AEME [61]	LSTM	NODDI
2012 NODDI [8]	Multishell	NDI, ODI, f_{SO}	2022 METSC	Transformer	NODDI
2015 SHORE [63]	Multishell	RTOP, MSD	2022 (Adapted from VIT) [62]	(Encoder- Decoder)	DTI denoising
2016 SMT [65, 66]	Multishell	$\lambda_{\perp}, \lambda_{\parallel}$	2022 SDnDTI [64]	Modified U-net	DTI
2018 Standard Model [2]	Multishell	$f, D_a, D_e^{\perp}, D_e^{\parallel}$	2022 Transformer [67]	Transformer (Attention)	FA, ODI
2020 SANDI(Ball, Stick, Sphere) [46]	Multishell	$f_{in}, f_{ec}, f_k, D_{in}$, D_{ec}, r_s (b-value>3000s/mm ²)	2022 ADL (Atlas Powered DL) [68]	U-net++	fODF
Block C: AI with Active Q-Space Geometry			2022 VRIRNet* [69]	GAN	NODDI
Models	General Architecture		2022 DLpN [12]	Adapted MLP	NDI
	RNN based Encoder- Decoder	Two different stages:	2021 IQT with Auto-Encoder [70]	Residual Network	SR
2023 ED-RNN [71]	HGT (based on	NODDI	2021 SRDTI [72]	CNN (3D)	DTI SR
2022 TAGCN [73]+RDT) [74]	TAGCN and Transformer (Attention)	DTI	2021 Multimodal SRqDL [75]	CNN (3D)	NODDI, SMT
2022 HemiHex-MLP [76]	Adapted MLP	NODDI Super angular resolution	2021 Super resolved Q-Space DL (SRqDL) [77]	CNN	SR
2021 Spherical CNN** [78]	CNN	DTI, Ball & Stick, IVIM, SMT, NODDI	2021 SuperDTI(70)	U-Net	DTI
2021 Bottleneck DL* [79]	CNN + Residual Block	fODF	2020 DeepDTI [83]	CNN + Residual Block	DTI
2021 Adapted SHResNet and M-heads [80]	MLP	NODDI, SHORE, DKI, fODF	2019 SHResNet [85]	CNN + Residual Block	DTI
2021 Q-Space feature-MLP [82]	Q-Space Conditioned DWI Generator [84]	U-Net, GAN	2019 MESC-Net [87]	LSTM	DWI harmonization
2020 GCNN [86]	GCN	fODF	2019 CNN-NODDI [89]	CNN	SMT, NODDI, SHORE
2019 CNN* [88]	CNN (3D)	fODF	2018 Deeper IQT with RevNet [90]	ML	NODDI
Block D: Models Leveraging AI & Maximum Likelihood Estimation (MLE) Frameworks			2017 MEDINPMEDN [91]	Adapted MLP	Permeability
Recent trends in AI models			2017 IQT [93]	ML (Regression Forest)	DKI, NODDI
2021/2022 DL prior NODDI [12, 92]	Single Shell NODDI	NODDI	2017 Trained Random Forest [94]	ML (Regression Forest)	
2022 DL-MLE [54]	Modified MLP initializes MLE	DTI	2016 q-DL [96]	MLP	
2023 dtIRM [95]	Modified RNN calculating MLE gradient				

Table 3.2: Neuro-biophysical models with their key parameters and relevant unified AI applications in diffusion MRI is classified in blocks.

3.3.2.2 AI with Angular Q-Space Features

Second category of algorithms is much more diverse in use of the geometry of the q-space. Inherent property of some of the architectures in this group helps to preserve this preceding geometry information, for example, graph and spherical convolutional (GCN/SCN) approaches extract features that are relevant to the geometry of the acquisition schemes [74, 78]. As the geometry of the q-space is incorporated, the mapping algorithms in the first category have been shown to be used in parallel to further enhance their performance [71]. Q-space dMRI regression is yet another unexplored area shown promising result when used with optimized protocol and a subsampling scheme [76, 101]. Furthermore, embeddings specifically designed over the q space analogous to zonal features have shown to map fODF using adapted MLPs [82]. Thus, we believe q-space is a natural characteristic of diffusion protocol that holds enough potential to be exploited.

3.3.2.3 AI and MLE Integrated Frameworks

Third category of algorithms embrace the recent trend in enhancing the Maximum Likelihood framework performances through Deep Learners. Gradient update computation and initialization are challenging areas due to which MLE algorithms often gets stuck in the local minima [54]. Advent of DL/ML has contributed in generalizing the gradient update framework for processing variant forms of data. Previously, signals and systems being analyzed with a forward model contributed in system specific gradient computation either analytically or numerically, which often pose computational and tedious derivation challenges, specifically with complex biophysical models and this complexity increased with new parameters introduced to the system. With that said, system specific derivatives with good choice of optimization framework in MLE

can be more powerful to rid bias and ensure specificity, which is important clinically. As spatial networks such as CNN, U-net, GAN based models often contributes to hallucination and systemic bias, this is often a risky bet in clinical implementation and this recent shift in deep learner-based instructions in improving MLE can help overcome such issue effectively [12, 54, 95].

3.4 Statistical Evaluation Frameworks

In this section, we highlight general statistical approaches used in neuroimaging research. These statistical frameworks generally has two primary goals for investigation. One is to retrieve group differences to understand pathological changes and second to investigate correlating factors to probe insights into relevant features and biomarkers responsible for neural pathogenesis. The statistical tests (like t-tests, Analysis of Variance (ANOVA)) are commonly used for group comparisons and involves controlling for multiple comparisons and confounding factors.

In general, statistical evaluation comprises of the handling of large data-sets commonly encountered in neuroimaging studies, and hypothesis testing which involves evaluation of p-values that enables investigation for statistical significance. Selecting appropriate data handling strategy and representation is the key for the accurate interpretation from the statistical evaluation (hypothesis testing).

3.4.1 Voxel Based Analysis

Representing the data voxel by voxel is the simplest and general exploratory approach to statistical evaluation, either through group comparisons or correlation analysis [102]. For exploratory studies that lack predefined hypotheses, conducting a voxel-based analysis (VBA) on the entire white matter of the brain is highly suitable.

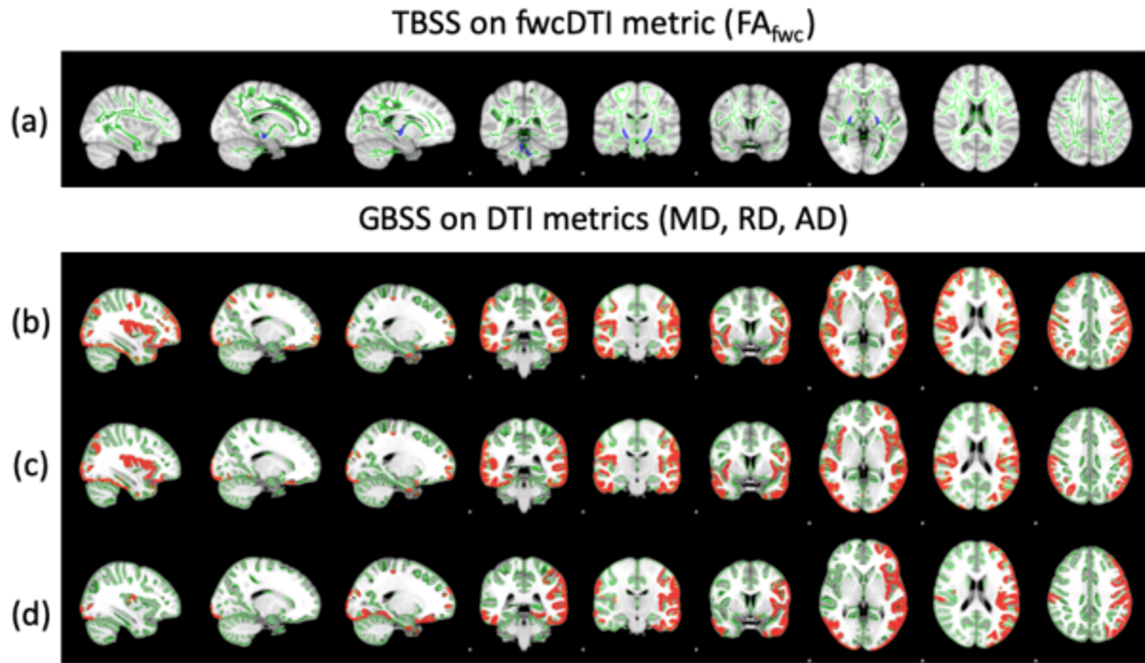


Figure 3.5: Example comparison of diffusion tensor and free water corrected tensor metrics (fwcDTI) using (a) TBSS and (b, c, d) GBSS analysis of HIV+ compared with age matched healthy controls at baseline. TBSS and GBSS Skeletons are in Green. TFCE corrected significance shown with blue(reduced) or red(increased).

While VBA is broadly beneficial in dMRI applications, it also demonstrates certain limitations.

3.4.2 Tract Based Spatial Statistics (TBSS)

Tract Based Spatial Statistics (TBSS) is a specialized method used in the analysis of dMRI data [103] by utilizing a skeleton derived from FA focusing on white matter tract. Similar analysis for gray matter is called Gray matter Based Spatial Statistics (GBSS). TBSS provides a voxel-wise analysis of multi subject diffusion data, focusing on the alignment of white matter tracts across different subjects for comparison. The advantages of TBSS over traditional voxel-based approaches includes improved sensitivity and objectivity in detecting white matter differences. TBSS is generally used

to study various neurological conditions and disorders, particularly those affecting white matter integrity, such as multiple sclerosis, migraine, traumatic brain injuries, etc. An example comparison is highlighted in Figure-3.5.

3.4.3 ROI Analysis

Region of Interest (ROI) analysis is a fundamental approach to understanding group differences for pathological effect in neuroimaging. In particular, the idea is to focus on specific brain areas for detailed examination. The process of selecting ROIs involves registration to anatomical landmarks or functional criteria, and then statistical analysis of data within these regions is carried out. Example shown in Figure-3.6

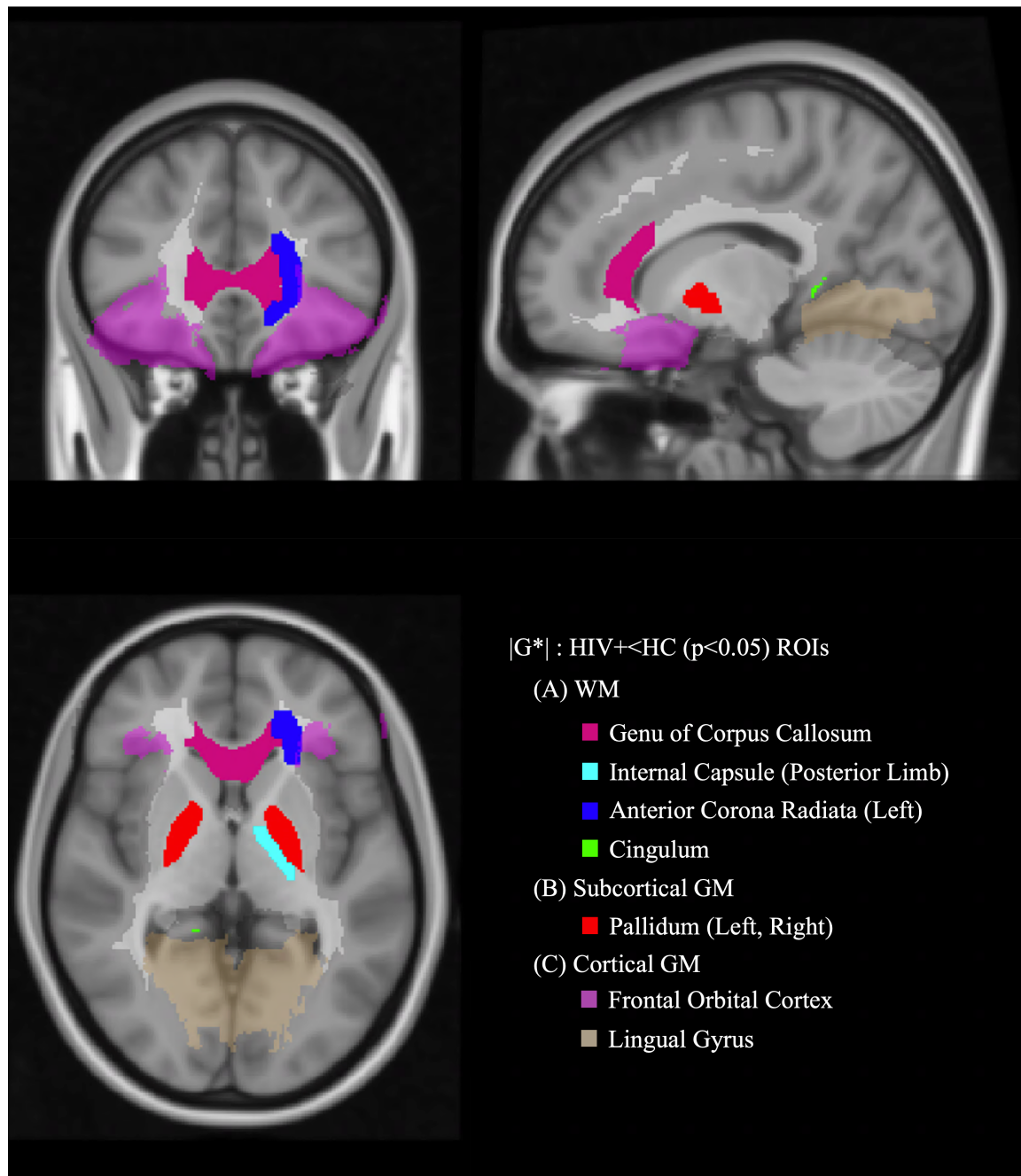


Figure 3.6: Example of atlas based ROI analysis between HIV+ and Control groups where the stiffness modulus ($|G^*|$), a parameter relating to brain tissue elasticity shows significantly reduced in the HIV group. JHU WM and HO cortical and subcortical atlases were used for the analysis. Significant ROIs ($p<0.01$) are overlaid on an MNI T1 image.

Chapter 4

AI in Q-Space Up-Sampling: Recovering Lost Clinical Details¹

4.1 Motivation

The application of Artificial Intelligence (AI), and particularly Deep Learning (DL) methodologies, in the realm of medical imaging has initiated a paradigm shift, catalyzing the emergence of a multitude of innovative applications. These advancements have significantly enhanced the quality of images and have enabled the generation of novel images from a constrained set of medical imaging data. It is, however, imperative to acknowledge that the predominant approaches for validating these DL techniques in the context of medical imagery have predominantly relied on visual or qualitative assessments, as opposed to comprehensive clinical study evaluations.

This precipitates a critical inquiry into the effects of these technological interventions on the preservation of vital quantitative clinical information within medical images. A pivotal consideration is whether the pursuit of high-quality imagery, as

¹The chapter was presented in MICCAI Challenge 2022 (QuaD'22) and partially published in Aja-Fernández, S., Martín-Martín, C., Planchuelo-Gómez, Á., **Faiyaz, A.**, Uddin, M. N., Schifitto, G., ... & Pieciak, T. (2023). *NeuroImage: Clinical*, 39, 103483.

facilitated by AI techniques, might inadvertently lead to the compromise of essential clinical data. Following this context, the efficacy of traditional image quality metrics, such as the Peak Signal-to-Noise Ratio (PSNR), Structural Similarity Index (SSIM), and Root Mean Squared Error (RMSE), becomes a salient factor in the assessment of AI-generated images. The fundamental criterion for these AI-enhanced images extends beyond mere visual similarity to the original; they must also ensure the retention of all critical clinical information while precluding the introduction of any erroneous data.

dMRI is instrumental in evaluating the microstructural characteristics of the brain and other organs [104, 105]. The integration of Deep Learning (DL) methodologies within this domain represents an emerging and promising area of study. Notably, DL applications in dMRI encompass several aspects of the data processing pipeline. This includes the rectification of phase discrepancies in multishot dMRI acquisitions [106], automated detection and elimination of image artifacts [107,108], as well as the application of noise reduction techniques [109].

In this research, Q-space resolution of dMRI has been specifically targeted. Angular resolution of the Q-space in dMRI plays a crucial role in identifying details in diseased processes of the brain [110]. For example, Figure-4.1 demonstrates the loss of clinical details in axial diffusivity with decreased Q-space resolution [4]. Thus, in this chapter, we focus on developing an AI strategy that aims to recover Q-space resolution relevant to clinical details. We hypothesized that if the up-sampling procedure can be guided through an equidistant delaunay triangulation sampling scheme, the nearest-neighbor geometry could potentially generalize diffusion signal at the original diffusion gradient direction, thus enabling us to estimate the signals, sensitive to clinical changes. The hypothesis was based on the interpolation techniques to estimate the signals for fiber orientation density estimation and tractography that had shown

positive result in simulation and *in-vivo* [111–113].

To corroborate the hypothesis, we generated the training and validation samples through a publicly (partially) available data-set from MICCAI Challenge held in the CDMRI workshop 2022 (QuaD22) [101]. The clinical data only included single-shell diffusion signals, that constrained our investigation only in DTI derived micro-structural features. The clinical differences were particularly significant with axial and mean diffusivity metrics from DTI when high angular resolution was being used. (Family-Wise Corrected p-value <0.05)

Performance evaluation included a dual-track validation approach. Firstly, mean squared error was employed at the training and validation stage when developing our model. Test data did not include high angular resolution data for the participants of the challenge & workshop before method submission, thus first blind evaluation was done on test data with lower angular resolution. The Tract Based Spatial Statistics (TBSS) approach was selected to assess clinical differences, which were family-wise error corrected, across a generalized Fractional Anisotropy (FA) skeleton mapped onto standard brain space [5]. This evaluation was conducted using high angular resolution test data, in collaboration with the organizers of the challenge. Finally, various AI methodologies within this field were evaluated and scored based on their performance in Tract Based Spatial Statistics (TBSS) and Region of Interest (ROI) analyses. The performance metrics employed for this evaluation were specifically designed to penalize false positive outcomes to ensure clinical evaluation of the compared AI techniques.

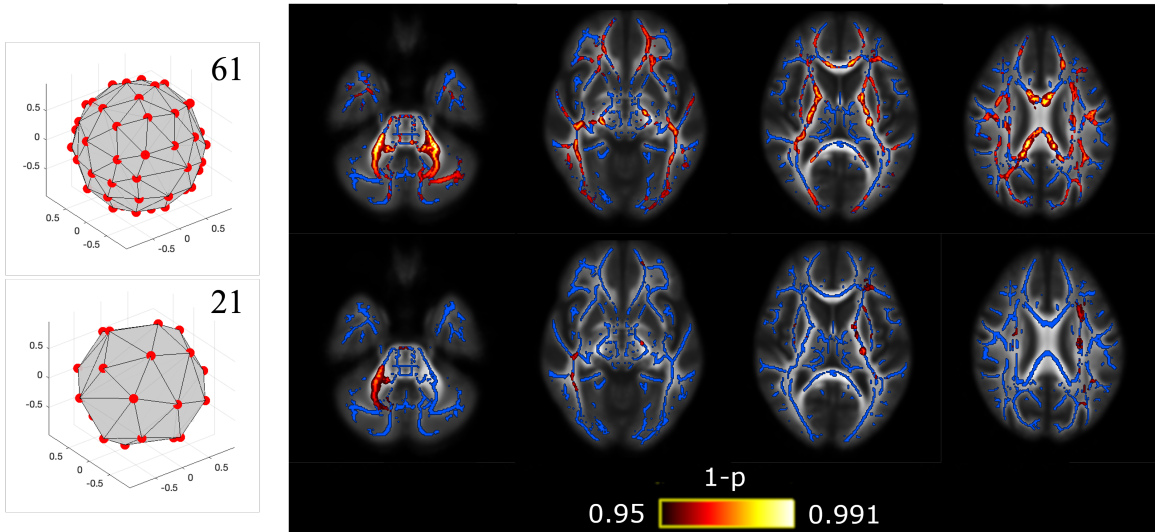


Figure 4.1: Axial Diffusivity difference in Chronic vs Episodic Migraine population (FW-corrected $p < 0.05$) top row with 61 and bottom row with 21 gradient directions, adapted with permission from Professor Santiago Aja-Fernández [4, 114]

4.2 Optimized Sampling of Q-space

We have utilized Iterative Maximum Overlap Construction (IMOC) and 1 Opt greedy method for optimizing gradient directions. [115, 116] The gradient directions in Lower Angular Resolution (LAR) were optimized to represent the uniformly distributed angular coverage. A similar approach was chosen to estimate the higher angular resolution nodes (HAR). The optimization of the protocol was performed using dMRItool in MATLAB. [29]

4.2.1 HemiHex Sub-Sampling in Q-space

HemiHex (HH) Subsampling can be regarded as subsampling the Q-space centering on an unknown node in such a way that the known and unknown Q-space nodes fall on approximated hexagon nodes, alternating knowns and unknowns. Hemi-Hex interpolation refers to the regression of an unknown center node on a hemi-hex sample.

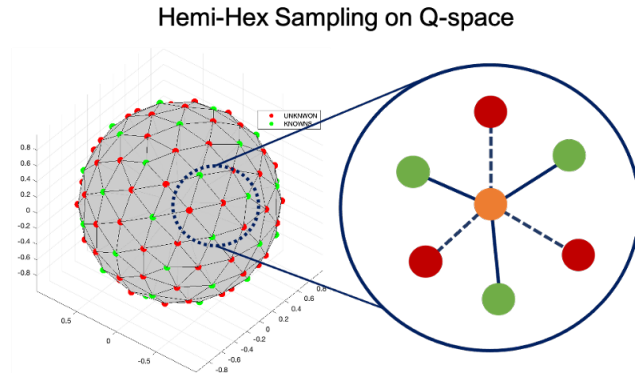


Figure 4.2: Hemi-hex subsampling on Q-space, the center node is an unknown surrounded with 3 known and unknowns.

The subsampling scheme results in more training data points per subject and thus requires fewer subjects to be trained contextually. (Figure-4.2)

4.2.1.1 HemiHex Subsampling Prerequisites

- Both the LAR and HAR images must have optimized sampled schemes in Q-space for diffusion protocol. Optimization makes sure that the gradients are equidistant and the hexagonal formation is possible between the known and unknown samples.
- The LAR gradients used must be common to HAR gradients and should be a subset of HAR grads. Number of gradients in LAR must be 3 times the number of gradients in the HAR.

4.2.2 Fully Connected Multilayered Perceptron

A fully connected Multi-Layer Perceptron (Figure-4.4) was used with 27×3 input layer and one node for diffusion weighted signal output for each gradient in the Q-space upsampling problem. The schematic diagram of the approach is elaborated in the next

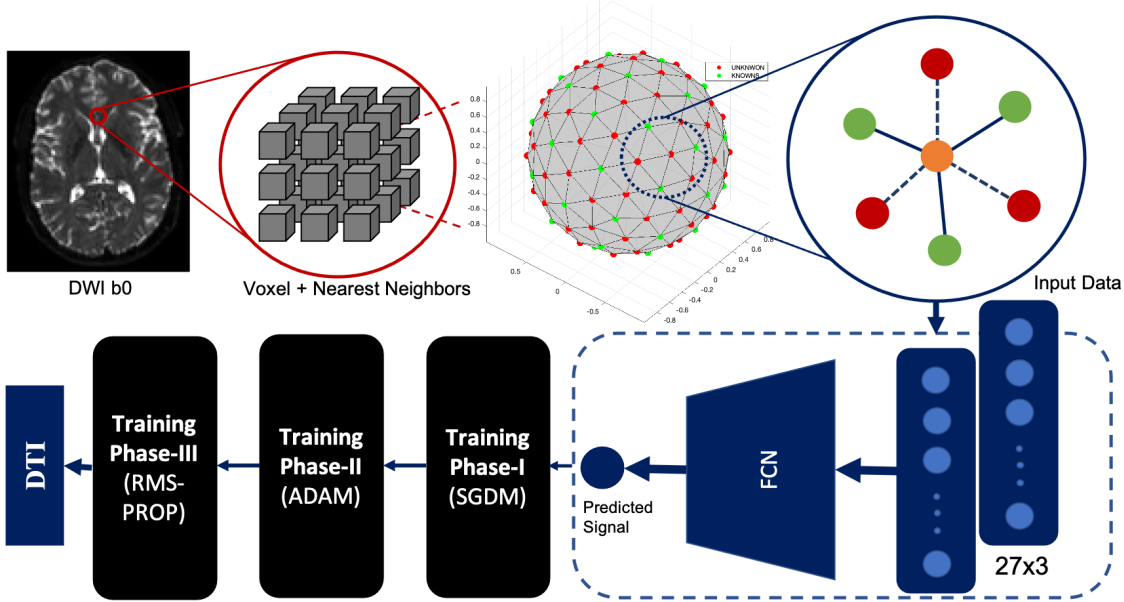


Figure 4.3: Schematics of angular upsampling of diffusion MR using contextual Hemi-Hex sub-sampling in an optimized Q-space using HemiHex-based MLP/FCN.

chapter in Figure-4.3. The input samples are 27 dimensional, as each centering voxel possesses 26 neighbors. Based on Delaney triangulation geometry, for each unknown signal, we always have 3 knowns on the sphere. The architecture is expected to be rotation invariant because the training being generalized on the sphere due to the inherent sampling geometry of the provided data. For each voxel, diffusion gradient signals for 40 unknown gradients are estimated.

Further, the second dimension of the inputs were obtained by HemiHex subsampling (Section-4.2), which generates training and validation data based on randomly sampled patches on a five-tissue segmented map. Five-Tissue segmentation was generated using the *fsl-fast* algorithm and was done to choose differentiating ROIs that are unique in nature. The expectation was that the local spatial information would be encoded and learnt by the network with relevant nearest angular diffusion signals. This was done using three subjects to finalize the training data. Validation data was

extracted similarly from five different subjects. In total, eight subjects are used for training and validating the network for DWI signal prediction. Since the training takes place in regressing the fourth dimension (the dwi signals with different directions but at the same spatial position), sufficient training data is sampled from eight healthy subjects.

The network is trained in three different phases with stochastic gradient descent with momentum (SGDM), adam and rmsprop algorithms respectively. Successive iterations and details on the requirement of three phase optimization is reported in the next chapter (Figure-4.5).

4.2.3 Hemi-Hex Features with Machine Learning Model

A fully connected network (FCN) is used with 27x3 input layer and one node for diffusion weighted signal output for each gradient. The schematic diagram of the approach is shown in Figure-4.3. HemiHex subsampling generates training and validation data required for training the FCN. Spatial neighbors are incorporated in the input domain of the learner.

The network is trained in three different phases with stochastic gradient descent with momentum, adam and rmsprop algorithms respectively. Successive iteration and details are reported on Figure-4.5.

ROIs were selected from GM, WM and merging areas from three subjects to obtain the training data. Validation data was similarly extracted from five other subjects. In total, eight subjects are used for training and validating the network for DWI signal prediction. Since the training takes place in regressing the fourth dimension (the dwi signals), sufficient training data is sampled from eight healthy subjects.

The input samples are 27 dimensional as each centering voxel posses 26 neighbours.

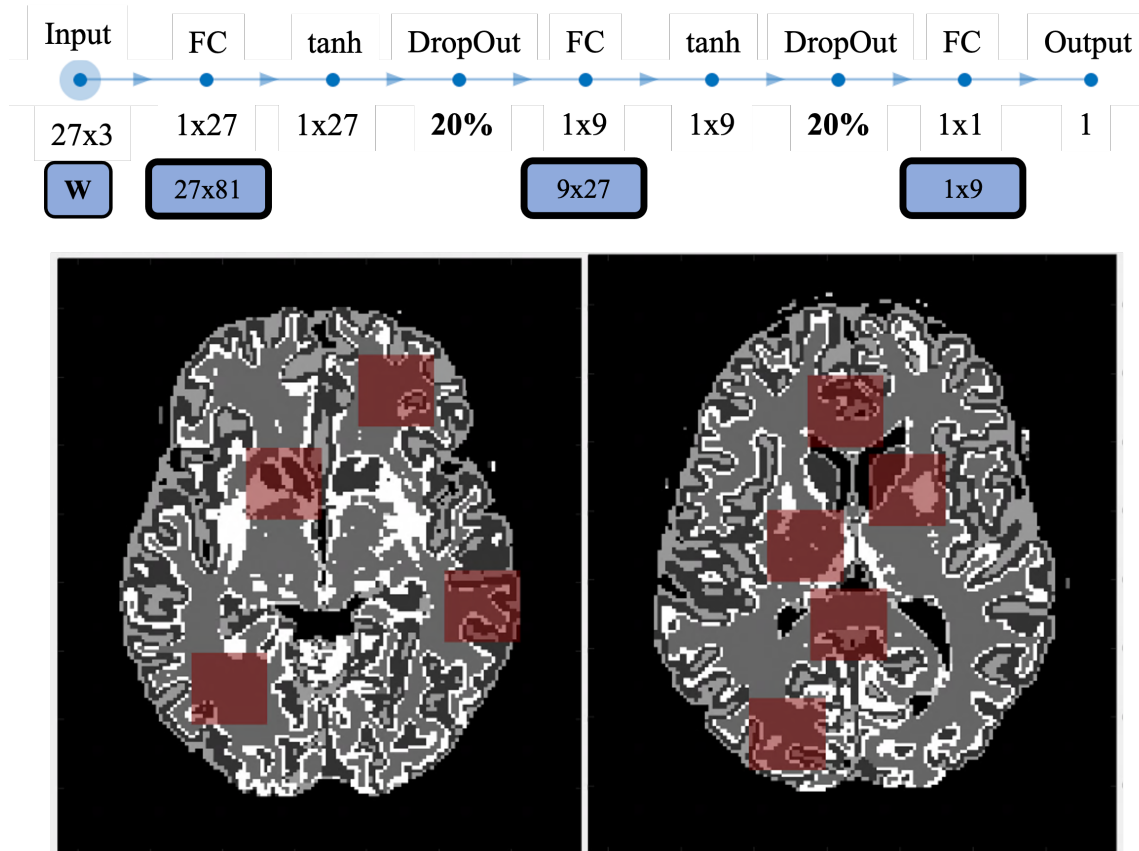


Figure 4.4: The Multi-Layer Perceptron for Q-Space Upsampling is shown in a schematic diagram, The layers are FC- Fully Connected, tanh, DropOut(20%) with around 2500 learnable parameters. Red segments on five-tissue MRI map depicts patch based random sampling of training and validation ROIs.

Based on Delaney triangulation geometry, for each unknown signal we always have 3 knowns on the sphere. The architecture is expected to be rotation invariant because the training being generalized on the sphere due to the inherent sampling geometry of the provided data. For each voxel, diffusion gradient signals for 40 unknown gradients are estimated.

Estimation Philosophy The network estimates DW signals for the unknown directions trained on the variable yet close geometric patterns. The final metric of evaluation are the DTI metrics. Once the data is upsampled, DTI is applied on the data and the final result is generated.

4.2.4 Optimization

For training the nearest neighbor regression network, we have used three different optimization algorithms. Stochastic gradient descent with momentum (sgdm), adam and rmsprop algorithms successively were applied on independent training data points to minimize the loss function. Three phase training had the same objective function for minimization,

$$MSE = \sum_{i=1}^D (x_i - y_i)^2$$

where, D is the number of total gradient directions for a voxel in x-space. x_i denotes the original gradient signal and y_i is the predicted gradient signal inferred from the subsampled input.

4.3 Metrics for Evaluation

This statistical investigation utilized datasets from two distinct migraine categories, Chronic Migraine (CM) and Episodic Migraine (EM). These datasets were ana-

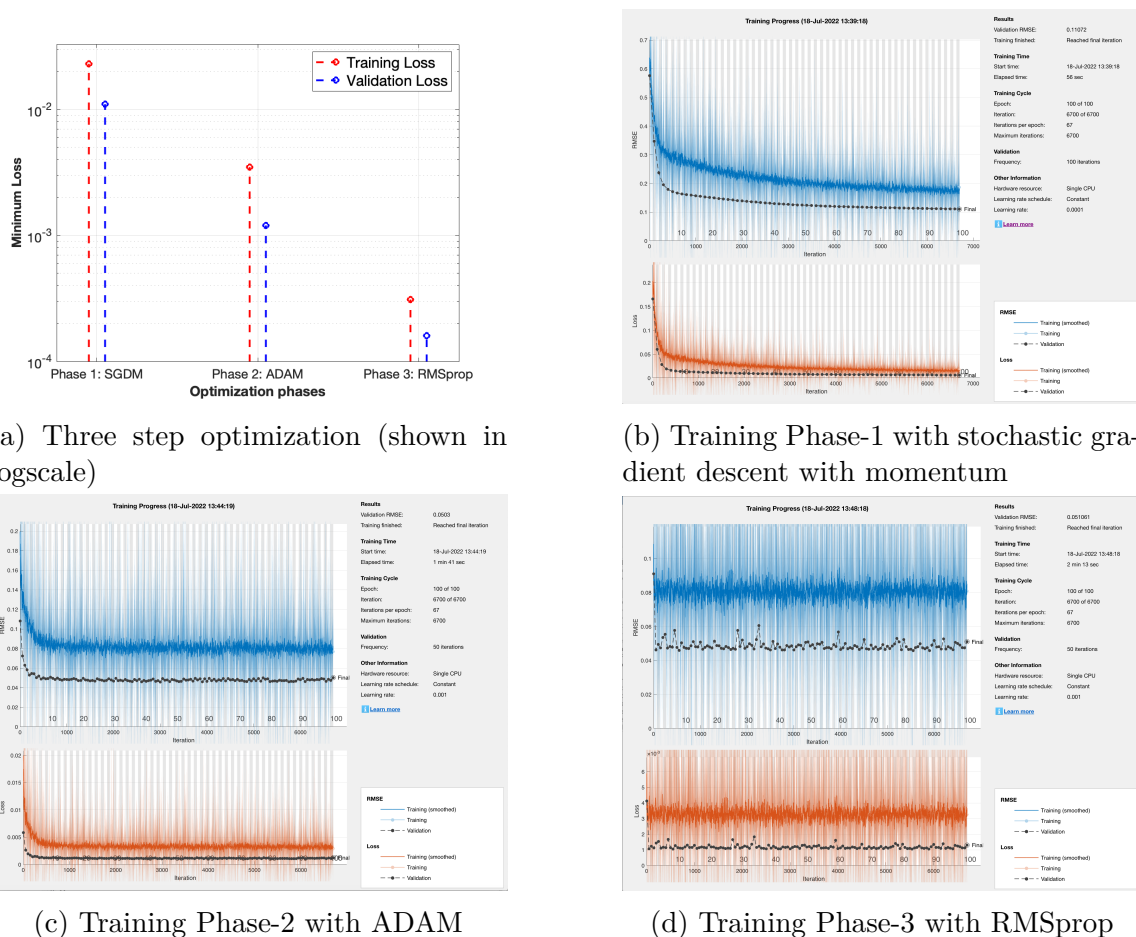


Figure 4.5: Sequential three step optimization reduce mean squared loss linearly (y-axis shown in log-scale).

lyzed through the tract-based spatial statistics (TBSS) technique as delineated by Smith and colleagues in 2006. The analysis focused on three key metrics: Fractional Anisotropy (FA), Mean Diffusivity (MD), and Axial Diffusivity (AD). To ensure impartiality, the study participants were not informed about the patient distribution across the CM and EM groups. Both the original and group-provided datasets underwent the same TBSS procedure. The FA images extracted were non-linearly aligned to the FMRIB-58 template within the Montreal Neurological Institute (MNI) space, which consists of averaged FA maps. This alignment employed b-spline based registration warp fields using the FNIRT tool from FSL [117]. Post-registration, a white matter skeleton was delineated through the thinning of an average FA image, applying an FA threshold of 0.2 for differentiating white from gray matter. The subjects' aligned FA images were then projected onto this white matter skeleton. The MD and AD maps were similarly registered to the MNI space and projected onto the skeleton using the same warp transformations as the FA images. For identifying regions with significant statistical differences, the Johns Hopkins University ICBM-DTI-81 White-Matter Labels Atlas was used [118]. A minimum region volume of 30 mm³ was set for statistical significance. To reduce variability, registration was performed with fully sampled data (61 gradient directions) and then applied to the group-provided data. The FA mask from the 61 gradients scheme was utilized for all groups. Voxel-wise differences in FA, MD, and AD between CM and EM were evaluated using the randomise permutation-based inference tool with non-parametric statistics in FSL, taking into account the threshold-free cluster enhancement (TFCE) results [119,120]. This method was applied to both original and group-provided maps, using 5000 permutations and a statistical significance threshold of $p < 0.05$ after family-wise error (FWE) correction for multiple comparisons. Two measures, True Positives (TP) and False Positives (FP), were used for comparative purposes. TP refers to voxels iden-

tified in the 61-gradients reference analysis, considered the benchmark. In contrast, FP denotes voxels marked as significantly different in the improved maps provided by participants but not in the 61-gradients reference analysis. Additionally, sensitivity and specificity metrics were calculated based on TP and FP ratios:

Sensitivity,

$$\text{Se}_i = \frac{\text{TP}_i}{\text{TP}_i + \text{FN}_i} = \frac{\text{TP}_i}{\text{TP}_i(\text{Ref})} \times 100(\%) \quad (4.1)$$

Specificity,

$$\text{Sp}_i = \frac{\text{TN}_i}{\text{TN}_i + \text{FP}_i} = \frac{\text{TN}_i}{\text{TN}_i(\text{Ref})} \times 100(\%) \quad (4.2)$$

Precision,

$$\text{Pr}_i = \frac{\text{TP}_i}{\text{TP}_i + \text{FP}_i} \times 100(\%) \quad (4.3)$$

False positive rate (FPR),

$$\text{FPR}_i = \frac{\text{FP}_i}{\text{FP}_i + \text{TN}_i} = \frac{\text{FP}_i}{\text{TN}_i(\text{Ref})} \times 100(\%), \quad (4.4)$$

Accuracy (ACC),

$$\begin{aligned} \text{ACC}_i &= \frac{\text{TP}_i + \text{TN}_i}{\text{TP}_i + \text{FP}_i + \text{TN}_i + \text{FN}_i} \\ &= \frac{\text{TP}_i}{\text{TP}_i(\text{Ref}) + \text{TN}_i(\text{Ref})} \times 100(\%) \end{aligned} \quad (4.5)$$

Here, $\text{TP}_i(\text{Ref})$ indicates the number of TP.

To evaluate the improvement over the analysis conducted with 21-gradients maps, which were not enhanced by any methods, whether AI-based or otherwise, following criteria was used:

$$\text{Comparing 21(Method)} = \frac{\sum_i (\text{TP}_i(\text{Method}) - \text{FP}_i(\text{Method})) - \sum_i (\text{TP}_i(21 \text{ g}) - \text{FP}_i(21 \text{ g}))}{\sum_i \text{TP}_i(61 \text{ g}) - [\sum_i (\text{TP}_i(21 \text{ g}) - \text{FP}_i(21 \text{ g}))]} \times 100[\%] \quad (4.6)$$

Here, $\text{TP}_i(21\text{g})$ and $\text{FP}_i(21\text{g})$ represent the counts of True Positives and False Positives, respectively, for the i -th metric, as determined by the reference analysis conducted with 21 gradient directions.

4.4 Results & Discussion

Angular Upsampling is an ill-posed inverse problem which can be made stable with the help of tessellated geometries designed in this work through sampling. Tessellated geometries ensure rotation invariant learning on the sphere (Q-space). And the neighboring voxels provide local spatial prior to learn the tissue property for a specific gradient. This makes sure high resolution counterpart can retain clinically relevant information through upsampling.

The implemented approach requires significantly less computational resources than general CNN based architectures. (We have used core i7 CPU with 16GB memory used for training). Which took less than 10 minutes for training.

The approach is highly efficient with training resources which yields important advantage for clinical applications and research. As less as 2/3 subjects is enough for training and acquire the contextual information for the gradients.

MICCAI Challenge 2022 (QUAD'22) Results					
Teams	University	TBSS	ROI	Total	Ranking
AF	University of Rochester	25.60%	15.79%	21.30%	1
ZJUWULAB	Zhejiang University	31.80%	5.26%	20.20%	2
LfB	Aachen University	26.30%	10.53%	19.40%	3
AINI	Harvard University	28.10%	5.26%	18.10%	4
UCL-CMIC	University College London	26.30%	5.26%	17.10%	5
Ucair	University of Utah	23.20%	5.26%	15.30%	6
ZJUT_IAISRC	Zhejiang University	25.30%	-5.26%	12.00%	7
uiowa_v2	University of Iowa	15.20%	0.00%	8.50%	8
uiowa	University of Iowa	8.20%	5.26%	6.90%	9
Diffusioneers	Universidade de São Paulo	14.10%	-5.26%	5.60%	10
Luschka	Tianjin University	-1.80%	-5.26%	-3.30%	12
SNU_AIML	Shiv Nadar University	1.40%	-10.53%	-3.80%	13
SaPaSt	New York University	-13.10%	-5.26%	-9.60%	14
314_JUNIORS	Zhejiang University	-56.10%	-78.95%	-66.10%	15
SNAC	The University of Sydney	-56.10%	-105.26%	-77.60%	16

Table 4.1: MICCAI Challenge 2022 (Quad'22) Results retrieved from Quad22 website

4.4.1 MICCAI Challenge 2022 Score & Standings

The challenge score and standings is shown in the Table-4.1. TBSS and ROI scores are averaged to report the final ranking. Proposed HemiHex-based MLP preserved angular context of the Q-space, thus presumed to have resulted better than the competing techniques. The method in average restored 21.30% of clinical differences previously lost when using 21 directions for evaluating clinical differences in Figure-4.1.

4.4.2 Image Quality Metrics (SSIM & PSNR)

The evaluation of image quality metrics, specifically the Structural Similarity Index (SSIM) and the Peak Signal-to-Noise Ratio (PSNR), plays a pivotal role in comparing the effectiveness of various image processing methods. These metrics are instrumental in assessing the quality and fidelity of images processed by different algorithms, providing a quantitative basis for comparison.

REFERENCE (21 grad)	SSIM			PSNR		
	FA	AD	MD	FA	AD	MD
CNN	0.23	0.01	1.00	26.4	13.2	13.0
HemiHex-MLP	0.97	1.00	1.00	31.5	81.0	83.3
MESC-SD	0.97	1.00	1.00	30.8	80.6	82.7
CNN+Residual Learning	0.97	1.00	1.00	31.4	80.8	83.3
U-Net	0.97	1.00	1.00	31.5	81.1	83.4
AutoEncoder_SH	0.97	1.00	1.00	31.5	68.8	71.1
AutoEncoder	0.96	1.00	1.00	30.4	79.9	81.6
AEME (Modified MESC)	0.96	1.00	1.00	29.1	80.2	82.8
Gated U-Net	0.96	1.00	1.00	29.8	76.2	78.6
U-Net + Angular Distance	0.88	1.00	1.00	22.4	68.9	70.7
3D U-Net	0.96	1.00	1.00	29.1	79.3	80.8
SARDU-Net (Cascaded MLP)	0.97	1.00	1.00	31.4	83.2	83.2
Transformer	0.97	1.00	1.00	30.7	78.3	79.3
U-Net	0.95	1.00	1.00	28.4	78.4	80.1

Table 4.2: Comparison of visual metrics achieved through different methods. [5]

SSIM is a metric that measures the perceptual difference between two similar images. Unlike traditional methods that focus on pixel-level differences, SSIM evaluates changes in structural information, luminance, and contrast, offering a more comprehensive and human-vision-centric assessment. A higher SSIM value, with a maximum of 1, indicates greater similarity to the reference image, thus implying better image quality.

PSNR, on the other hand, quantifies the quality of a reconstructed image compared to its original version. It is widely used in the field of image compression, where it measures the ratio of the maximum possible power of a signal to the power of corrupting noise. High PSNR values suggest a low level of noise and error, indicating higher image fidelity.

The provided table presents a comparative analysis of various image processing methods using these two metrics. The methods range from traditional approaches

like Convolutional Neural Networks (CNN) to more sophisticated architectures like U-Net and its variants.

The SSIM values in the table reveal significant insights. For instance, methods like MLP, MESC-SD, and various U-Net implementations demonstrate near-perfect SSIM scores, highlighting their superior ability to maintain structural integrity and visual similarity to the reference images. This is particularly important in applications where preserving the original structure of the image is critical, such as medical imaging or satellite image analysis.

In terms of PSNR, we observe a wide range of values across different methods. The higher PSNR scores achieved by techniques like MLP, U-Net, and SARDU-Net suggest their effectiveness in minimizing distortion and noise in the processed images. These high scores are indicative of the methods' efficiency in accurately reconstructing images, making them suitable for applications where image clarity and detail are paramount.

In summary, the comparative analysis using SSIM and PSNR metrics provided a valuable insight that all the methods except CNN based approach performed well in reconstructing visually similar results. It is important to note that visual similarity does not conform to clinical evaluations.

4.4.3 TBSS & True and False Positive Scores

The bar chart (Figure-4.6) contrasts the performance of various image processing methods in terms of their true and false positive detections concerning Axial Diffusivity (AD) and Mean Diffusivity (MD). A true positive reflects the method's ability to correctly identify regions of interest (ROIs) that are genuinely affected by changes in diffusivity, a key aspect in applications such as medical imaging, where accurate

detection can be critical. False positives, however, indicate regions incorrectly flagged as affected, which could lead to misinterpretation of the condition being studied.

In the context of AD, the MLP method demonstrates a high number of detected ROIs with a balance skewed towards true positives, suggesting a high specificity. In contrast, methods like the U-Net with Angular Distance show a lower count of detections but with a high proportion of false positives, indicating a tendency towards overestimation of affected areas.

For MD, the chart indicates that methods such as Gated U-Net and SARDU-Net (Cascaded MLP) have a relatively high detected ROI count with a favorable ratio of true positives, indicating effective detection capability for mean diffusivity changes. The U-Net (3D) and AutoEncoder_SH also show substantial true positive detections, albeit with some false positives, suggesting a need for further refinement to reduce over-detection while maintaining sensitivity.

We speculate that, spatial architectures are prone to hallucinations, thus more false positives results in clinical evalution. On the other hand the contextual sampling of features on Q-space with hemihex MLP doesn't rely on spatial learning, which is likely the reason for showing better performance in retrieving diseased ROIs accurately.

4.4.4 Training Resources & Efficiency in Clinical Applications

In the realm of clinical applications, the judicious use of training resources is crucial, particularly due to the limited availability of annotated datasets and the pressing need for swift development of diagnostic models. The table delineates image processing methods into three categories: sparse, spatial, and sequential, each reflecting a different approach to resource utilization and training strategy. This categorization is

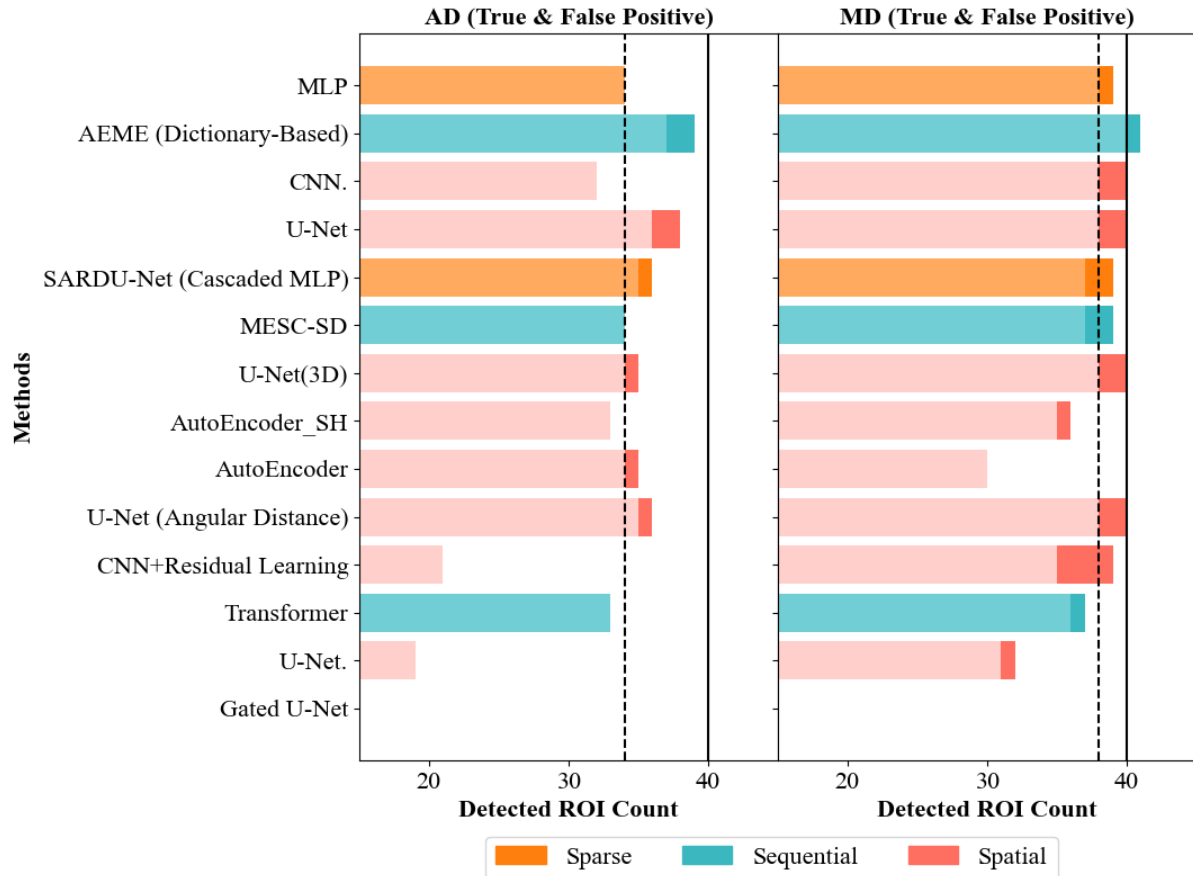


Figure 4.6: True and False Positive ROIs detected in Axial and Mean Diffusivity by different methods (Sorted by Ranking). Data for comparison were obtained from CDMRI'22 workshop. HemiHex-based MLP is our proposed approach [76], compared to other techniques, results reported from [5]

Methods	TRAINING	VALIDATION	TESTING	Loss Function (Training)
CNN	45	5	10	MSE
HemiHex-MLP	3	5	105	RMSE
MESC-SD	36	9	15	MSE
U-Net + Angular Distance	50	5	5	Perceptual loss
U-Net	54	3	3	MSE
AutoEncoder_SH	5	5	50	MSE
AutoEncoder	5	5	50	MSE
AEME (Modified MESC)	7	1	2	MSE
Gated U-Net	60	60	60	MAE
CNN+Residual Learning	44	10	6	normalized RMSE
3D U-Net	40	20	20	PSNR
SARDU-Net (Cascaded MLP)	48	6	6	MSE
Transformer	32	8	5	RMSE
U-Net	40	10	10	FA: MSE / AD, MD: MAE

Table 4.3: Number of subjects in each approach for training, validation, and testing, along with the loss function used for training procedure [5]

vital in clinical contexts where the scarcity of data and the immediacy of application are key concerns.

Sparse Methods: The MLP (HemiHex) method is a prime example of a sparse approach, using a remarkably small number of training subjects (3), but extensively tested on a larger set (105 subjects). This method, which employs RMSE as the loss function, is particularly advantageous in clinical scenarios where data is a premium and the focus is on validating the algorithm's effectiveness across a broad spectrum of cases with minimal training resources.

Spatial Methods: Spatial methods are typified by Gated U-Net, which employs an evenly distributed dataset for training, validation, and testing (60 subjects each). The choice of MAE as the loss function points to an emphasis on reducing errors across the image space. While this approach demands a more substantial dataset, it is suited for scenarios where spatial precision is imperative, and ample data is at hand.

Sequential Methods: Sequential methods, such as AEME (Modified MESC), adopt a training regime that is characterized by a sequential progression through phases with a modest number of subjects, as evidenced by its 7 subjects for training and very limited numbers for validation and testing. Utilizing MSE as the loss function, this method is optimized for scenarios where sequential learning from a small dataset is necessary, which is often the case in clinical settings where patient data is subject to stringent privacy regulations and may not be readily accessible.

The MLP (HemiHex) as a sparse method and AEME (Modified MESC) as a sequential network stand out for their efficiency in resource utilization. The sparse nature of MLP (HemiHex) underscores its potential in clinical settings where it's critical to maximize learning from a minimal amount of data. On the other hand, the sequential approach of AEME (Modified MESC) reflects the method's adaptability to the stepwise availability of data, which is a common scenario in ongoing clinical studies. Both approaches are indicative of the strategic use of resources, ensuring that despite data limitations, the development and validation of diagnostic models can be carried out effectively and expediently, catering to the urgent demands of clinical application.

4.5 Limitations & Future directions

We proposed a fully connected regression network integrating the philosophy of geometric distribution and interpolation of DWI data. The low resource need and ease of computation makes the approach more suitable for use in single-shell dMRI clinical studies.

The proposed approach only up-samples diffusion signals for protocols with uniformly distributed directions that is optimized with IMOC algorithm, whereas in most real clinical scenarios the diffusion directions are often un-optimized. Our future objective involves accounting for un-optimized clinical protocols by incorporating zonal Q-space features in our model.

Chapter 5

Single-Shell NODDI Reconstruction: Simulation Study¹

5.1 Motivation

NODDI was proposed as one of the practical biophysical models which can probe deeper into different compartments of tissue system that co-exist together in brain at mesoscale. One of the prerequisite to identify different compartments is to have the knowledge for the behaviour of diffusing particles at a particular direction over time. In chapter-2 (Section-2.4), we have showed that the diffusing relationship with time still holds, and can be proxied by sampling of sets of Q-spaces with different b-values. Sets of Q-spaces are also termed as shells. Thus, diffusion protocol with multiple sets of Q-space with different b-values are called multi-shelled protocols. In clinical diffusion data, we are required to use single-shell data to characterize multiple compartments, which is deemed an ill-posed problem for NODDI [8].

In this chapter, we focus on understanding the ill-posed-ness of the single-shell

¹The chapter was presented in Proc. Intl. Soc. Mag. Reson. Med. 29, 2021 and published in **Faiyaz, A.**, Doyley, M., Schifitto, G., Zhong, J., & Uddin, M. N. (2022). *NMR in Biomedicine*, 35(2), e4628.

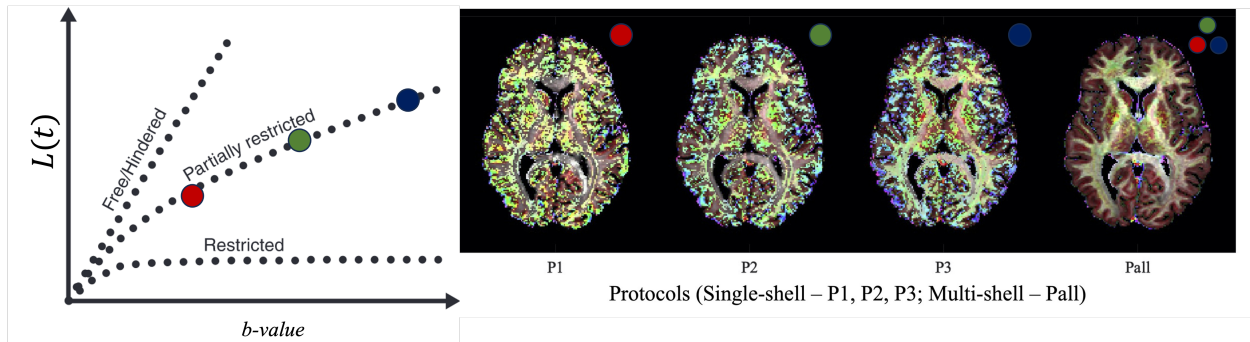


Figure 5.1: Single-shell data cannot reconstruct NODDI (NDI, ODI, f_{ISO}). Three parameters are merged in HSV space for combined viusalization

problem in simulation. We conditioned the free NODDI parameters in order to investigate if the problem can be stabilized in simulation.

Performance evaluation included a dual-track validation approach. Firstly, mean squared error was employed at the training and validation stage when developing our model. Test data did not include high angular resolution data for the participants of the MICCAI challenge & workshop [101] before method submission, so blind evaluation was done on test data with lower angular resolution. Then, Tract Based Spatial Statistics approach was opted to evaluate the family wise corrected clinical differences on a generalized FA-skeleton on standard brain space [5] based on the high angular resolution test data in collaboration with the host of the challenge. Finally, different AI approaches in the field was scored based on the TBSS results. The performance metrics for evaluation was tailored to penalize false positives outcomes by any methods.

5.2 Simulation Study Design

This section outlines the comprehensive approach used in our study to evaluate the DLpN framework in conjunction with NODDI. This methodology closely mirrors the

original NODDI study, but incorporates additional cases to explore a wider range of micro-structural effects.

5.2.1 NODDI Distribution in Healthy Human Brains

For this investigation, MRI scans from three anonymized participants, randomly chosen from the Human Connectome Project (HCP) dataset, were utilized. This dataset is publicly accessible and is provided by WU-Minn HCP (release-Q3 32). All individuals involved in the study gave their written consent, and the research received approval from the appropriate institutional review board (https://db.humanconnectome.org/data/projects/HCP_1200).

The acquisition of multi-shell dMRI (dMRI) images was carried out using a Siemens 3T Connectome scanner located in Erlangen, Germany. The images were obtained using the Spin Echo- Echo Planar Imaging (SE-EPI) technique, characterized by a repetition time (TR) of 5520 ms and an echo time (TE) of 89.5 ms. The imaging parameters included a field of view measuring 210 x 180, an isotropic voxel size of 1.25mm, a multiband factor of 3, and the collection of 90 gradient directions across each shell at b-values of 1000, 2000, and 3000 s/mm^2 , along with 18 $b=0\ s/mm^2$ reference images. The duration for scanning each shell was approximately 9:50 minutes. Subject data underwent corrections for bulk motion, susceptibility-induced distortions, and eddy currents as outlined in [121]. More details about the scanning parameters and protocols are available at <http://protocols.humanconnectome.org/>.

In this investigation, the computation of microstructure parameters, including Neurite Density Index (NDI), Orientation Dispersion Index (ODI), and fractional isotropy f_{ISO} , was performed using the NODDI toolbox. These calculations were based on a complete set of 270 diffusion gradients (denoted as Pall) and were treated

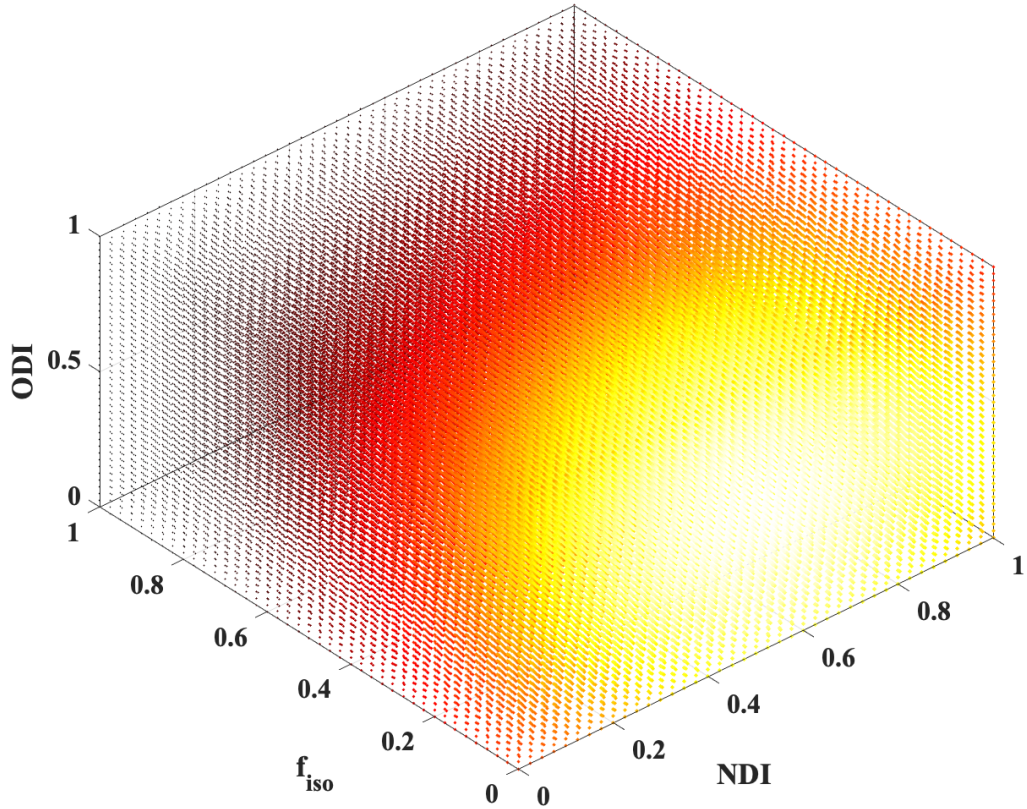


Figure 5.2: NODDI parameter (NDI, f_{iso} , ODI) distribution in three healthy control subjects from HCP

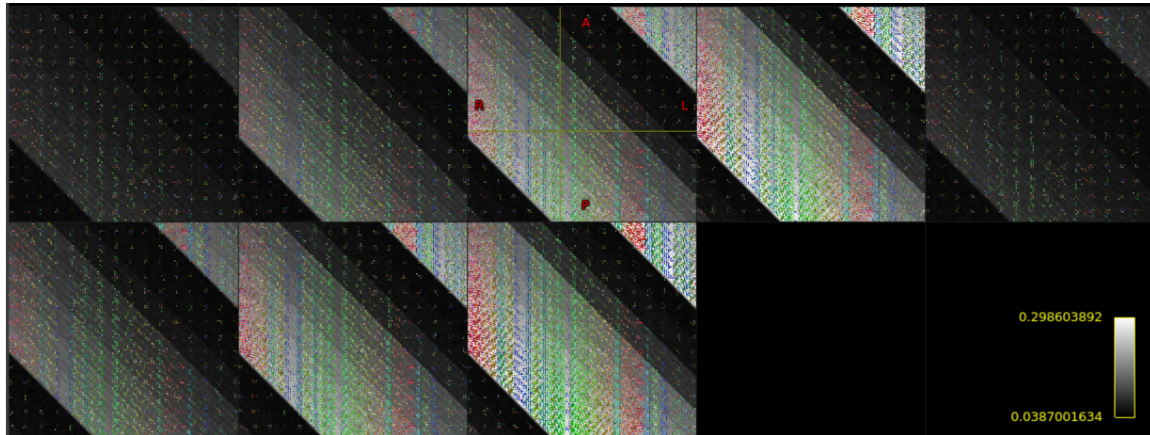
as quasi-ground truth for the study. The distribution for three healthy subjects is observed in Figure-5.2 with the help of a 3D Gaussian colormap ranging from 0 to 1. The probabilistic distribution motivated the later simulation performed in selection of microparamters (Section-5.2.2).

5.2.2 Microstructure Parameters for Simulation

The core of our simulation involved synthesizing MR signals based on known ground-truth tissue micro-structures. Key parameters included the isotropic volume fraction

Protocols	b-values (number of gradients)	Parameters	Ground-truth values
P1	b1000 (90)	NDI	0.2, 0.4, 0.6, 0.8
P2	b2000 (90)	f_{ISO}	0, 0.12, 0.25, 0.4, 0.5, 0.75, 1
P3	b3000 (90)	$a(\text{radii})$	0.5, 1, 2, 4 μm
P12	b1000(90) + b2000 (90)	$\kappa(ODI)$	0, 0.25, 1, 4, 16
P13	b1000(90) + b3000 (90)	$\mu(\theta, \phi)$	254 Q-space directions
P23	b2000(90) + b3000 (90)		
Pall	b1000(90) + b2000 (90) + b3000 (90)		

Table 5.1: Diffusion MR protocol & key parameter values for DWI simulation

Figure 5.3: NODDI parameter (NDI , f_{ISO} , ODI) based simulated data inspired from the distribution in healthy human brain

(f_{ISO}), which is generally negligible in white matter (WM) but significant in gray matter (GM) and regions contaminated by free water. To this end, we simulated f_{ISO} values of 0, 0.12, 0.25, 0.4, 0.5, 0.75, and 1, allowing for a comprehensive examination of both WM and GM structures. For each tissue type, representative model parameters were chosen, encompassing 640 different micro-structural configurations across 254 uniformly sampled Q-space directions. Example healthy human brain inspired f_{ISO} distributions and CSD configurations of simulated diffusion signals from the distributions are shown in Figure-5.3 and 5.4 respectively.

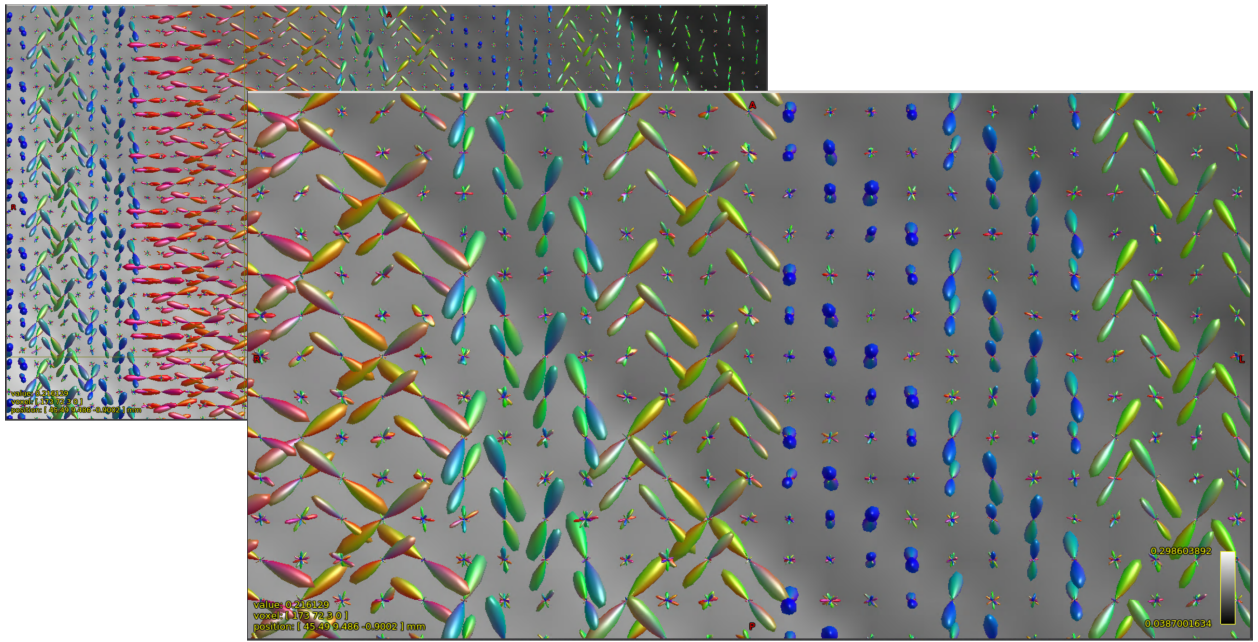


Figure 5.4: Close Visualization of Constrained Spherical De-convolution based SH representation of simulated diffusion data.

5.2.3 Simulation Protocols

The simulation strategy, as previously detailed in [8], involved the use of the publicly available NODDI toolbox (version 1.01), accessible at <http://mig.cs.ucl.ac.uk/index.php?n=Tutorial.NODDImatlab>. We customized the initialization of this toolbox to meet our specific requirements, particularly focusing on varying axonal diameters, denoted as a .

The comprehensive set of protocols selected for these simulations, which encompassed 90 directions on the Q-space for each of three b-value sampling, is detailed in Table 5.1. For reference in Table-5.1, b1000 indicates a b-value of 1000 s/mm^2 and so on. The number of gradient directions determined the length of the diffusion signal being simulated. Multi-shell protocols used in the simulation are P12, P23, P13 and Pall as referenced in Table-5.1

For the quantitative analysis of the synthesized signals, the 'dtifit' tool from FSL was employed. This tool facilitated the computation of the Mean Diffusivity (MD) and the baseline signal S_0 (i.e. T2w signal) of the synthesized data. Finally, the Signal-to-Noise Ratio was set at 20dB by incorporating Rician noise, to mimic realistic MRI conditions in the diffusion signal.

5.3 Proposed Architectures for Single-Shell NODDI

Dictionary-based Learning prior NODDI (DLpN)

Figure-5.5 illustrates the schematic of the proposed DLpN network. The DLpN approach separates the estimation of f_{ISO} adopting a dictionary based learning strategy termed as “DictNet” (Section-5.3), and then fits for the other non-linear parameters posed in the NODDI problem with a Rician noise model. In this framework, the NODDI toolbox was modified to use f_{ISO} as a known parameter [8]. Once we have an approximation of the f_{ISO} , the Rician log-likelihood framework can be employed to solve the inverse problem of identifying NDI and ODI. Considering the estimated likelihood based on the dMRI signal, the initial parameters are selected from the grid search. Since f_{ISO} is already approximated from the dictionary framework, the grid search complexity is reduced. We fit the parameters by minimizing the negative of Rician log-likelihood defined as follows:

$$L(\text{NDI}, \kappa, \theta, \phi | f_{ISO}, d_{\parallel}, d_{ISO}) = -\log \prod_{i=1}^N \frac{M_i}{\sigma^2} e^{-\frac{(M_i^2 + A^2)}{2\sigma^2}} I_0\left(\frac{AM_i}{\sigma^2}\right) \quad (5.1)$$

which is similar to the NODDI problem, except that the initial f_{ISO} prior is estimated with DictNet. In the Equation 5.1, A is synthesized and M is the measured signal, NDI is the neurite density index, κ term is inversely proportional to ODI

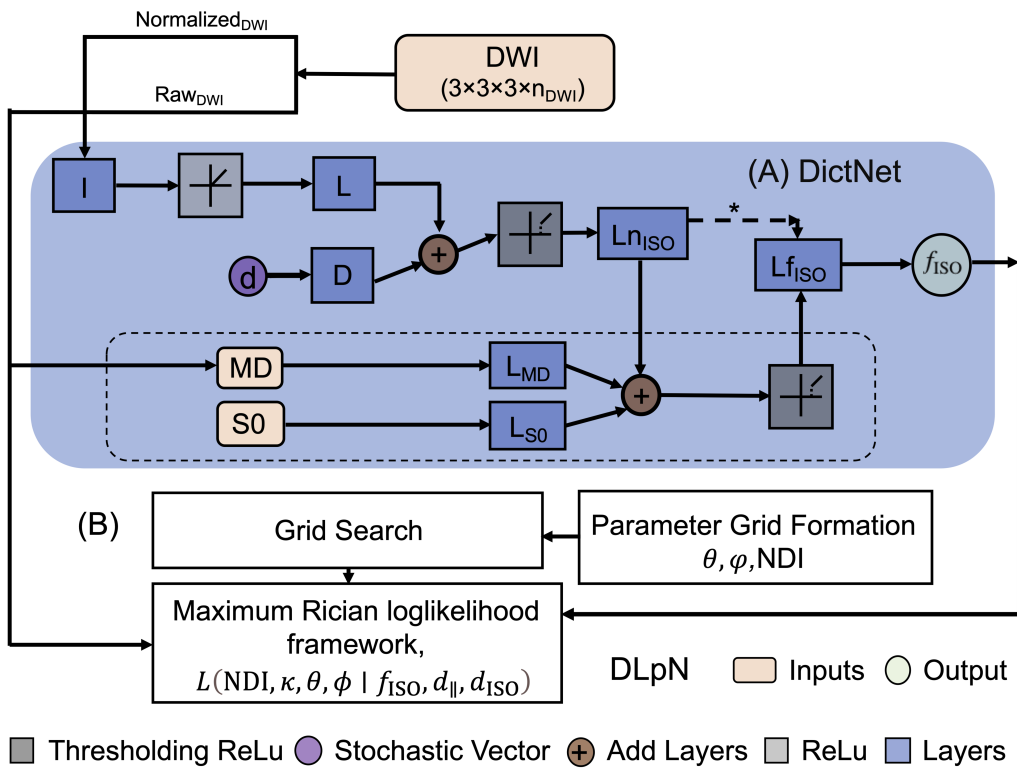


Figure 5.5: Schematic of the proposed DLpN. The stochastic dictionary learning framework (DictNet) estimates f_{ISO} prior and then used with NODDI Rician log-likelihood estimation steps for NDI and κ mapping. A) DictNet, B) DLpN.

(Equation 3.8), f_{ISO} is the isotropic volume fraction, and σ is the estimated standard deviation from the measured signal per voxel, θ and ϕ are the fiber directions initially estimated from the weighted least squared DTI fitting, then fitted with NDI and κ in the NODDI framework.

Adapted Multilayered Perceptron: **DictNet** is a sparse dictionary based learning strategy that has been devised based on previous deep learner models [87,122] to estimate f_{ISO} . Typically, with a known sparse dictionary ϕ , the coefficients f can be assessed by an l_1 -norm regularized least squares problem

$$\hat{f} = \arg \min_{f \geq 0} \|\phi f - y\|_2^2 + \lambda' \|f\|_0 \quad (5.2)$$

where y is the ground-truth parameter. λ' is an adjustable parameter to control the sparsity level of f . This was resolved using the IHT algorithm [123] by the following formulation used in Microstructure Estimation using a Deep Network (MEDN) [122].

$$f^{t+1} = H_\lambda(Ld_{in} + Df^t) \quad (5.3)$$

where t is the iterative index, L and D are layers determined by the sparse dictionary ϕ , and $H_\lambda(\cdot)$ is a thresholding function with $\lambda > 0$.

$$H_\lambda(x) = \begin{cases} 0, & x < \lambda \\ x, & x \geq \lambda \end{cases} \quad (5.4)$$

The thresholding function is defined by a parameter λ , which is related to λ' . d_{in} is the normalized diffusion signal cascaded with $3 \times 3 \times 3$ spatial data.

Previously proposed deep architecture models, such as MEDN, Advanced MEDN

(PMEDN) (Ye, 2017) and Microstructure Estimation with Sparse Coding Network (MESC-Net) [87] used 8 iterations of IHT in its original and modified forms. However, this redundant iterative process can be reduced by seeding a stochastic vector to resemble a generative model. By replacing the iterative scheme with a constant stochastic layer, we can eliminate unnecessary weight vectors, thereby saving memory and training time, as follows, for the estimation of f^I of a voxel without hindering performance.

$$f^I = H_\lambda (Ld_{\text{in}} + Dd) \quad (5.5)$$

This is illustrated in Equation (5.5), where d is the constant stochastic vector, the basis on which the dictionary ϕ is built. Now, to incorporate important f^I priors such as MD and $S0$ in the dictionary ϕ , the following layers were added, accounting for Equation (5.5).

$$f = H_\lambda (MD \cdot L_{MD} + S0 \cdot L_{S0} + f^I \cdot L_{nISO}) \quad (5.6)$$

where, L_{MD} , L_{S0} , and $L_{(nISO)}$ weigh MD , $S0$, and f^I respectively in single-shell f^I learning. The generated coefficient vector f contributes to a fully connected feedforward network to estimate f^I . The final contribution was thresholded with a thresholding ReLU function, similar to PMEDN defined in Equation 5.4. However, Equation (5.6) is only valid for single-shell cases; for multishell cases, the f_{ISO} of Equation (5.5) contributes to the fully connected feedforward network for the estimation of f^I .

The DictNet differs from other conventional deep learners (e.g., PMEDN [91], MLP [96]) in several key aspects:

- Conventional deep learners for NODDI focused on reducing only the diffusion gradients without changing multi-shell configuration of the protocol, whereas

our proposed network mimics the behavior of these conventional deep learners with the seeding of a constant stochastic vector and focuses on generating f_{ISO} with single-shell.

- Seeding of the constant stochastic vector guides the in vivo training, and we sensitize the model on the simulated data in the process, which is not done in previous approaches (PMEDN or MLP).
- Our model accounts for T2w i.e., non-diffusion weighted signal S0 (inherently collected as b0 images) and MD in training. We provide empirical evidence in the NODDI simulation that the use of S0 and MD allows the model to estimate single-shell f_{ISO} more accurately than other approaches.
- It requires 8-fold less memory and reduced time compared to conventional approaches, as the stochastic vector initialization helps in quick learning.

5.4 Results

We reconstructed the NODDI parameters from synthesized dMRI signals with protocols defined in Table 5.1 by initializing the model with a known f_{ISO} introduced with random 0 to 5% error. The simulation results obtained with $f_{ISO}=0$ were the same as in the original NODDI paper [8] (not shown). However, with additional f_{ISO} cases, we found different results, and our precursory investigation with synthetic data simulation supports that NDI and ODI can be reconstructed reliably from single-shell dMRI imaging data if f_{ISO} is used as a prior. The estimation results for NODDI with $f_{ISO}=0$ and additional f_{ISO} cases are described below.

Simulations	DWI protocol	NDI	ODI	f_{ISO}	Fitted Results
Experiment-1	Single-shell	known	unknown	unknown	Ill-posed
Experiment-2	Single-shell	unknown	known	unknown	Ill-posed
Experiment-3	Single-shell	unknown	unknown	known	Approx. GT

Table 5.2: f_{ISO} determined as the bottleneck parameter in Rician Log-likelihood fitting of simulation data in experiment-3 where NDI, ODI was fitted parameters and f_{ISO} was known.

5.4.1 Conditioning Single-Shell NODDI Problem

5.4.1.1 f_{ISO} as the Conditioning Parameter

Figure 5.6 illustrates the NDI reconstruction for different protocols with DLpN and original NODDI fittings. However, using the synthetic data generated with additional f_{ISO} plausible cases, we show that NODDI fitting resulted in NDI deviation (upward bias) from the ground-truth with multi-shell protocols for NDI ground-truths of ≤ 0.4 (Figure 5.6). We also found the downward bias with high variance for single-shell protocols reconstructed with NODDI model except at the ground-truth NDI=0.2. In contrast, we observed that f_{ISO} prior reconstruction in DLpN can result in NDIs with markedly improved accuracy and precision in both single- and multi-shell cases. This illustrates that independent estimation of f_{ISO} may lead to a better estimation of NDI. However, some deviations from the ground-truth values were observed in the case of protocol P2 and P3 at lower NDI. This could probably be because measurements at high b -values may not support tortuosity constraints (in the GM or lower NDI region) posed by the NODDI model~35 or lower SNR for higher b -values.

Figure 5.7 illustrates that ODI reconstruction with proposed DLpN and NODDI fittings for different protocols and ground-truth values. We found similar trends in ODI for both DLpN and NODDI fittings, however DLpN had a lower variance for all protocols. Consistent with previous NODDI reports, bias and variance are low for the

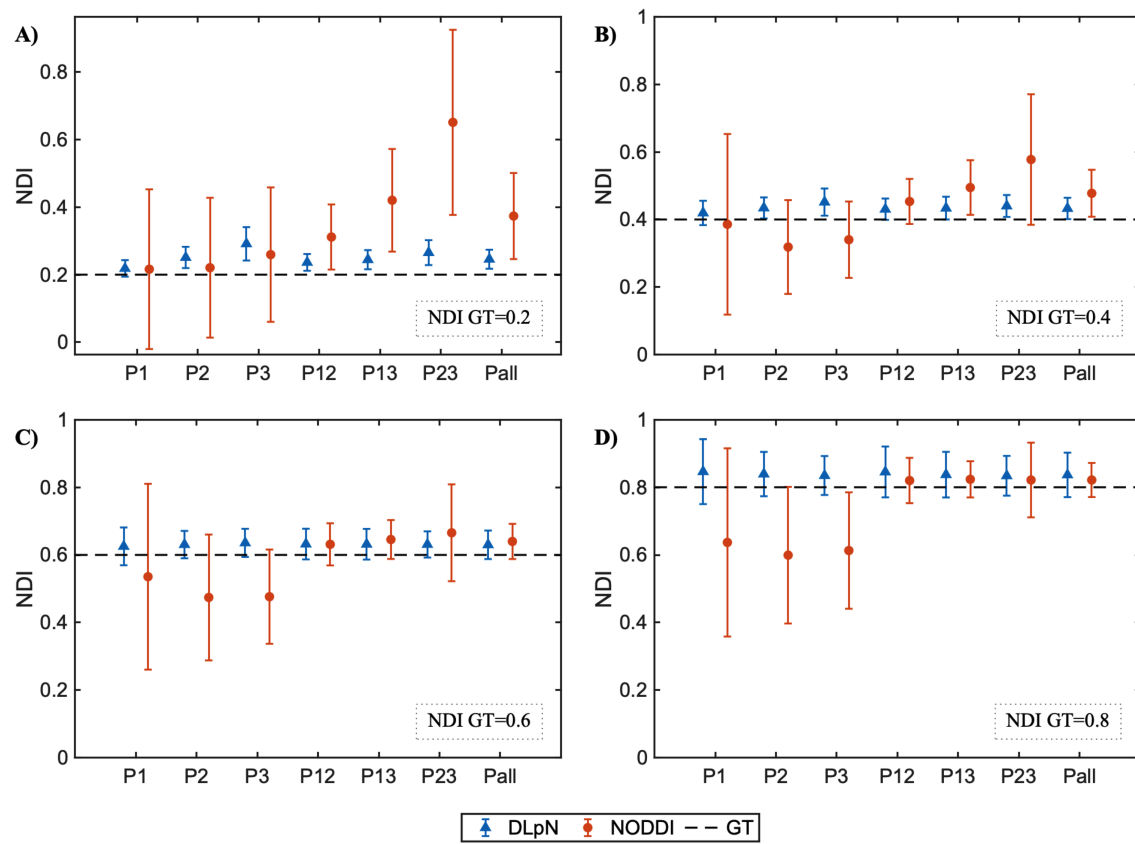


Figure 5.6: Neurite Density Index Results with conditioned f_{ISO} . GT -Ground Truth.

ground-truth values of ODI less than 0.5. Variability of ODI for higher ground-truth values is related to the ODI itself. Physically, orientation distributions corresponding to large ODIs (e.g., 0.5 to 1) are not very different from one another and the high variance reflects the lack of difference due to its inherent mathematical definition. More details can be found in the original NODDI report [8]. It should be noted that a higher ODI corresponds to highly dispersed neurites, mainly residing in GM and has been previously shown to improve with the number of gradient directions used without any dependency on the number of shells [8].

5.4.1.2 f_{ISO} Conditioned Result In-vivo

To prove the concept from the observed result of the simulation, we performed the conditioning experiment on one of the HCP subjects acquired with protocols detailed in 6.2.1. f_{ISO} used in conditioning the single shell estimation of NDI was obtained from the multi-shell NODDI fitting. The map obtained was similar to multi-shell derived NDI demonstrated in Figure-5.8.

5.4.2 Estimation of Independent f_{ISO} with Single-Shell

The findings from the previous sections indicated that, estimation of fractional isotropy or f_{ISO} is the key to get Neurite Density and Orientation Dispersion sensitivity.

In this section we have utilized DictNet (Section-5.3), which is an adapted multi-layered perceptron without any prior information to compare the single- and multi-shell derived results with NODDI.

Dictionary-based network (DictNet) with no priors estimated f_{ISO} at ground-truth values A) 0, B) 0.12, C) 0.4, D) 0.75, E) 1 (indicated with a dashed line) on the simulation test-set with defined protocols P1, P2, P3, and Pall for different NDI

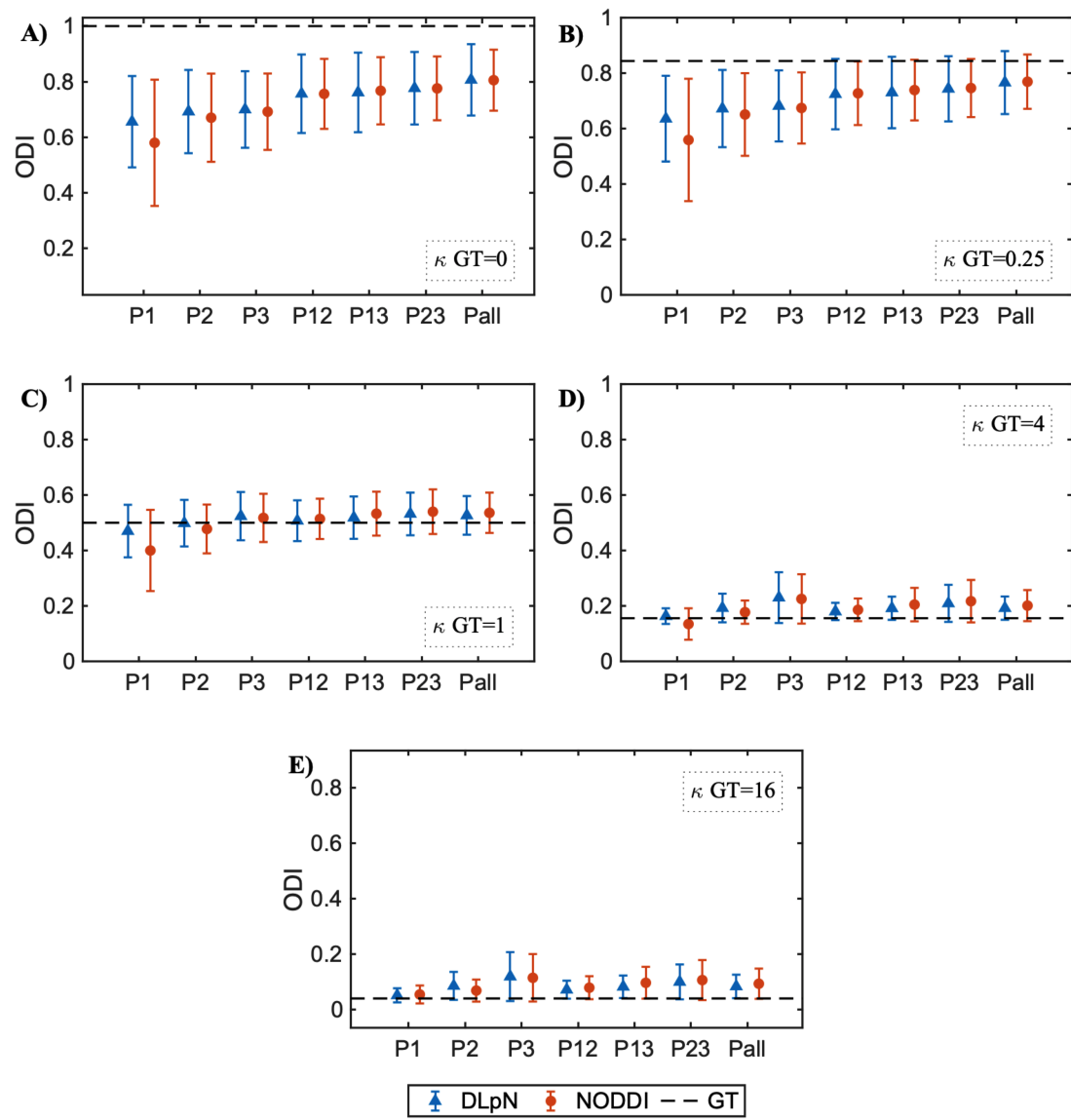


Figure 5.7: Orientation Dispersion Index Results with conditioned f_{ISO} . GT - Ground Truth.

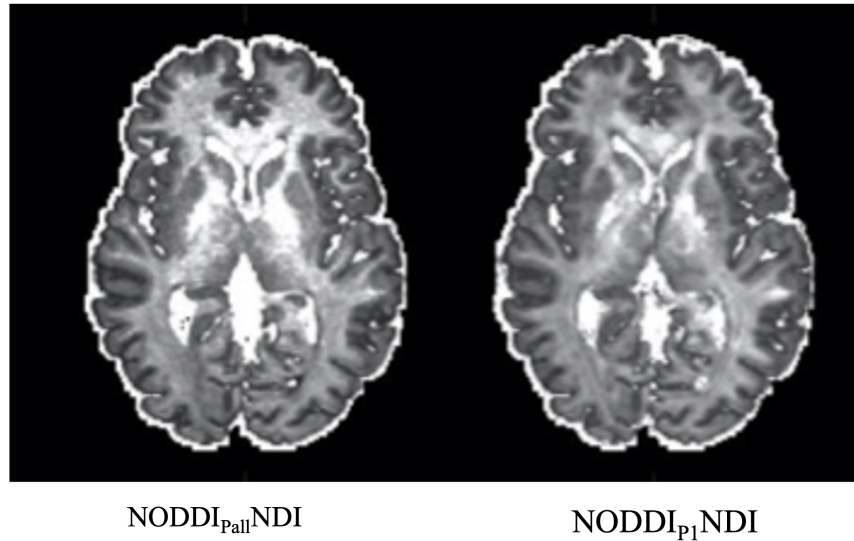


Figure 5.8: Invivo NDI estimation using multi-shell derived f_{ISO} using single shell protocol P1. Multishell derived NDI is shown for reference.

ground-truth values provided in Figure-5.9. We found evidence that, the f_{ISO} values derived from DLpN (without priors) outperforms single-shell NODDI ($NODDI_{P1}$, $NODDI_{P2}$, $NODDI_{P3}$) but was not close to the ground truth values defined in the synthetic simulated data. Thus, single-shell reconstructed f_{ISO} with DictNet(no priors) failed to estimate accuracy neurite density in simulation.

5.5 Discussion

In this work, we demonstrate that NODDI parameter maps such as NDI and ODI were reconstructed from single-shell diffusion data using a dictionary-learner-estimated f_{ISO} as a prior with high accuracy.

In order to generate f_{ISO} values from the single-shell data, we devise a network that takes advantage of the IHT strategy used in previous studies. [87, 91]. We propose a non-iterative scheme of IHT where a constant stochastic layer determines the learning of dictionary coefficients by the spatial-angular sparse data from the

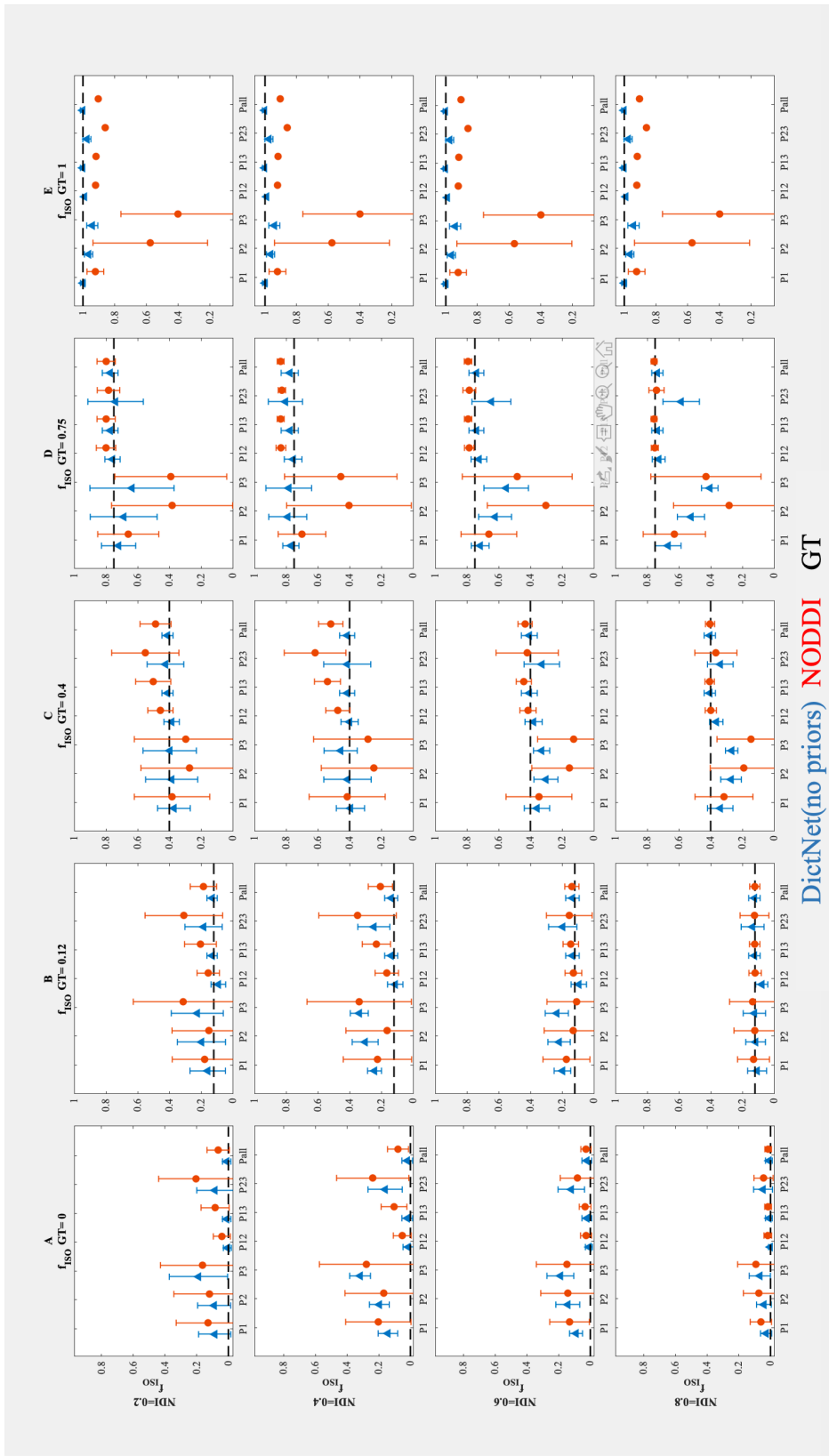


Figure 5.9: Estimation failure of f_{ISO} independently

simulated data-set based on the protocol obtained from the *in-vivo* data 5.3. The generated coefficient vector contributes to a fully connected feed-forward network to estimate the f_{ISO} . The network did not incorporate any additional imaging modalities when estimating f_{ISO} . In this work we saw, single-shell alone with an estimator was not sufficient to independently generate f_{ISO} .

5.6 Limitation & Future Direction

Our simulation experiment revealed that single-shell NODDI was possible if and only if the f_{ISO} parameter could be accurately estimated or known. But even with rigorous training with simulation data using a dictionary-based machine learning model, we were unable to estimate single-shell f_{ISO} .

To our knowledge, we are the first to study NODDI in a single-shell setting. Although the experiment revealed a promising workaround, it was limited by the estimation of f_{ISO} . This limitation has been addressed in the next chapter.

Chapter 6

AI in Single-Shell NODDI: Application & Clinical Validation¹

6.1 Motivation

In Chapter-5, it was observed that by conditioning fractional isotropy (f_{ISO}) parameter of NODDI, we can stabilize the single-shell problem. However, this approach necessitated independent estimation of the f_{ISO} . However, we observed from the simulation that, estimation of f_{ISO} was not straightforward with Multi-Layer Perceptron or dictionary-based networks.

In this chapter, we hypothesized that any multi-modal MR contrast that accounts for tissue water density holds the potential to estimate f_{ISO} when integrated to the tested machine learning framework. So, clinically available contrasts i.e. T2-weighted MRI and mean diffusivity contrast were integrated to test our hypothesis, first in simulation and then applied *in-vivo* for further investigation. Objective validation was performed with a Rician log-likelihood function and evaluated with ROI-based

¹The chapter was partly published in **Faiyaz, A., Doyley, M., Schifitto, G., Zhong, J., & Uddin, M. N. (2022). *NMR in Biomedicine*, 35(2), e4628.**

correlation analysis and error values.

Postmortem studies have established that one of the most noticeable changes in brain anatomy and size occurs due to aging, which initiates and advances atrophy in gray and white matter [124]. Aging is correlated with an increase in the overall amount of cerebrospinal fluid (CSF), as well as the fluid found within the brain's ventricles, known as intraventricular CSF (iCSF), as reported in the research by Giorgio et al. [125] and Statsenko et al. [126]. Therefore, our *in-vivo* investigation included evaluation of the sensitivity of single-shell derived neurite density, free water (fractional isotropy), and neurite orientation dispersion in aging and also in the cognitive performance of clinical and control subjects.

6.2 Data Acquisition & Quality Comparison

In this section, datasets with different quality are utilized to compare reconstructions in different signal-to-noise scenarios.

6.2.1 High Quality Data: Human Connectome Project

De-identified MRI images from 8 subjects selected randomly from the publicly available Human Connectome Project (HCP) dataset provided by WU-Minn HCP (release-Q3 32) were used. All subjects provided written informed consent and the study was approved by the institutional review board (https://db.humanconnectome.org/data/projects/HCP_1200).

Multishell dMRI images were acquired using a 3T Connectome scanner from Siemens in Erlangen, Germany using the SE-EPI sequence with a repetition time of 5520 ms and echo time of 89.5 ms. The field of view was 210 x 180, the voxel size was isotropic at 1.25 mm, the multiband factor was 3, and 90 gradient directions

were acquired for each shell with b values of 1000, 2000 and 3000 s/mm^2 and 18 $b=0\ s/mm^2$ reference images. Each shell took around 9:50 min to scan. The subject data was corrected for bulk motion, susceptibility-induced, and eddy current distortions [121]. Further information on the scan parameters and study protocols can be found at <http://protocols.humanconnectome.org/>. In this study, microstructure parameters (NDI, ODI, f_{ISO}) were computed using the NODDI toolbox with a full set of 270 diffusion gradients (i.e., Pall) and considered as the pseudo ground-truth.

6.2.2 Clinical Data: Cerebrovascular Small Vessel Disease

In addition, we tested our approach to HIV participants with cerebrovascular small vessel disease (CSVD) from an ongoing study at the University of Rochester. The participants provided written informed consent prior to the scans, and the study was approved by the University of Rochester’s Research Subject Review Board (RSRB). Briefly, 66 subjects (34 Controls and 32 HIV+ subjects) were used to test our approach. Two healthy subjects were used for training and rest as test data. The dMRI scan was performed using 2D SE-EPI sequence (TR=4300ms; TE=69.0ms; FOV=256×256; resolution=1.5mm isotropic, 64 gradients per shell with $b=1,000$ and $2,000\ s/mm^2$ with 7 $b=0\ s/mm^2$ reference images). In order to facilitate the training of our model, we scanned two volunteers with the same protocol as above along with an additional $b=3000\ s/mm^2$ for the same 64 gradient directions.

Synthetic data In order to evaluate the DLpN framework together with NODDI, we utilized known ground-truth tissue micro-structures for different protocols and synthesized MR signals, as similar to the approach used in the original NODDI study [49], with $f_{ISO} = 0$ as well as with additional f_{ISO} cases reported in Table-5.1. The f_{ISO} is negligible in WM [127], but to investigate the underlying effect of

GM structures and free water contaminated ROIs, additional f_{ISO} cases of 0.12, 0.4, 0.75, 1 were added in the simulation experiment. The simulation strategy is described previously [8]; we have used the publicly available NODDI toolbox (version 1.01, <http://mig.cs.ucl.ac.uk/index.php?n=Tutorial.NODDImatlab>) and modified the initialization to fit the simulation needs for different diameters, a . To simulate tissue configurations of WM and GM, model parameters were set to representative values for both tissue types. The selected set of parameters in simulation is reported in Table-5.1. The parameter set accounts for 400 different microstructure configurations in 254 uniformly sampled Q-space directions, termed as mean orientation, $\mu(\theta, \phi)$. Different mean orientations were used to create synthetic training and test datasets. FSL’s “dtifit” tool was used to calculate the MD and S_0 of the synthesized signals. Note that Rician noise of 20dB was added to the synthetic data.

6.2.3 Data Analysis

Harvest-Oxford (subcortical GM) and JHU-ICBM (WM) atlases were used to calculate regional averages in the standard space (1mm) in predefined ROIs. Pearson correlation tests were used to test the associations between two variables. A p-value of < 0.05 was considered statistically significant.

All the data processing and analysis were performed using Python (v2.7.16), Keras (v2.0.5), MATLAB 2019a (MathWorks Inc., Natick, MA, USA), FSL (v6.0.0) and ANTs (v2.1.0).

6.3 Training, Validation & Test

Initially, the DicNet network is trained with the simulated data. The synthetic simulated dMRI data (Section-6.2.2) with Rician noise (20dB) accounts for a greater

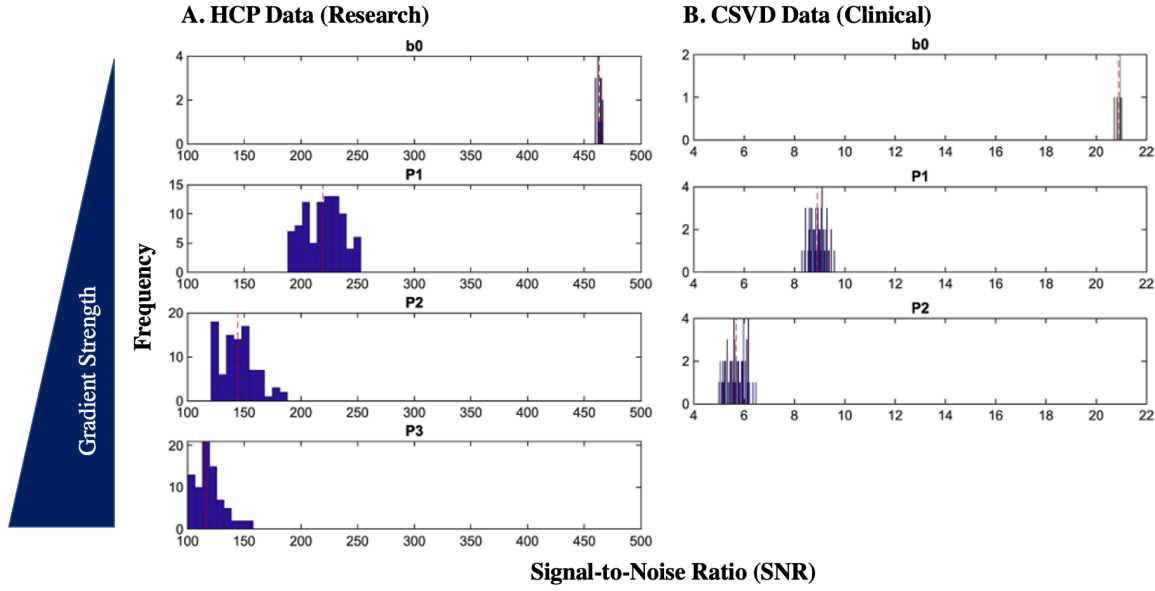


Figure 6.1: Signal-to-noise ratio (SNR) of the dMRI data for Human Connectome Project with connectome research scanner and CSVD clinical data, shows the significant SNR differences as higher gradient strengths are in use.

number of tissue configurations than the tissue configurations expected from a single brain. The initial state of the network is obtained by minimizing the error in the simulated data for the stochastic vector d .

$$N_0 = \Upsilon_S \left[\min_d N(d, S) \right] \quad (6.1)$$

Let S be the synthetic training set, N the current network state, N_0 the updated state obtained at the end of the current epoch, and Υ_S denote training based on the minimized network state by d with data S . Seeding is performed 10 times (chosen empirically), and the state that minimizes the error is updated as the current state of the network and further trained with the synthetic training set. If the d vector cannot result in a minimized state for the current epoch, training takes place with the current state of the network. The training and validation loss per epoch for f_{iso}

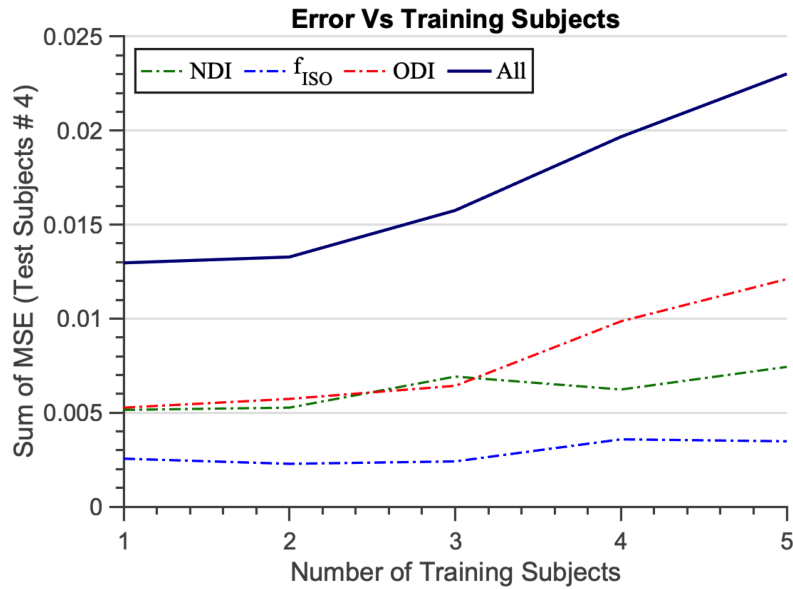


Figure 6.2: Demonstration of minimum error with data sampling from two subjects. Training with higher number of subjects suggests over-fitting dictionary based network.

with DictNet and PMEDN are available in Faiyaz et al [12].

In-vivo training starts from the final N_0 . With 8 randomly selected subjects, we used HCP dMRI data from 2 subjects as the training set, and the remaining subjects were used for testing. The number of training subjects was chosen based on results reported in Figure 6.2. We found that if the number of training subjects is greater than three, the network is more prone to overfitting. Overfitting after training with 3 subjects is seemingly because the training was performed voxel-wise and for any brain in general, the number of possible tissue configurations are limited. So, the increment of training subjects indicates the increment of additional sets of similar data samples, which the network is already familiar with. For two subjects, we had masked brain voxels (each around $145 \times 174 \times 145$ samples minus the background) for training where 15% subjects was used for cross-validation in each epoch, with a maximum of 10 epochs. In the train/test phase, the dMRI signal was normalized with the mean

non-diffusion weighted b_0 image and used as input for the network.

For the in-vivo training, the pseudo-ground-truth microstructure parameters (NDI, ODI, and f_{ISO}) were calculated using the NODDI method with the complete set of 270 diffusion gradients. The focus of the DLpN reconstruction was on retrieving the f_{ISO} prior, so the f_{ISO} prior was trained and estimated using the DictNet. To evaluate the DLpN NDI and ODI reconstructions, the other pseudo-ground-truth parameters (NDI and ODI) were used based on the percentage differences and by maximizing the objective function. To make the dictionary stable for single-shell cases, the mean diffusivity (MD) and the non-diffusion weighted signal intensity (S0) were obtained for both the synthetic data and the in-vivo data using a single-shell protocol, and were used in constructing the f_{ISO} dictionary. The same procedures were followed for the CSVD dataset.

6.4 Results & Discussion: Incorporating T2-w and MD Priors

In order to test our hypothesis of using T2-weighted (aka S0) and Mean Diffusivity (MD) priors, we integrated them with DictNet. The performance evaluation was done initially in simulation where DictNet training with and without priors were performed keeping the training parameters identical and then their usefulness was demonstrated in estimating f_{ISO} compared to state-of-the-art free water f_{ISO} estimators, and in extreme parametric scenarios. Finally, the approach was evaluated *in-vivo* in both high quality and clinical quality dMRI.

6.4.1 Simulation

6.4.1.1 Performance with & without T2-w (S0) and MD Priors

Dictionary-based network (DictNet) estimation of f_{ISO} with and without T2-w (S0) and MD at ground-truth values A) 0, B) 0.12, C) 0.4, D) 0.75, E) 1 (indicated with a dashed line) on the simulation test set with defined protocols P1, P2, P3, and Pall for different NDI ground-truth values provided in Table-5.1. We found evidence that, the f_{ISO} values derived from DLpN (with or without S0 and MD initialization) outperforms single-shell NODDI ($NODDI_{P1}$, $NODDI_{P2}$, $NODDI_{P3}$). Further, using T2-w (S0) and MD prior improves the performance of DictNet, and f_{ISO} values are closer to ground-truth values as illustrated in Figure 6.3.

6.4.1.2 Comparison of State-of-the-art Free Water f_{ISO} Estimators

Comparison of the simulation of DictNet derived f_{ISO} with bi-tensor model-based FW (both for single- and multi-shell), deep learner based PMEDN and NODDI with different protocols show that DictNet derived f_{ISO} estimation is stable with single-shell P1 and P2 protocols, compared to that of other approaches (Figure 6.4). It is evidently because these approaches do not incorporate either priors (T2-w (S0), MD), and dictionary accounted for the simulated complex tissue microstructures as done for DictNet.

6.4.1.3 Evaluation of extreme parametric scenarios

Evaluation of extreme cases was carried out with two cases-

- Low NDI and normal f_{ISO} .
- High NDI and high f_{ISO} .

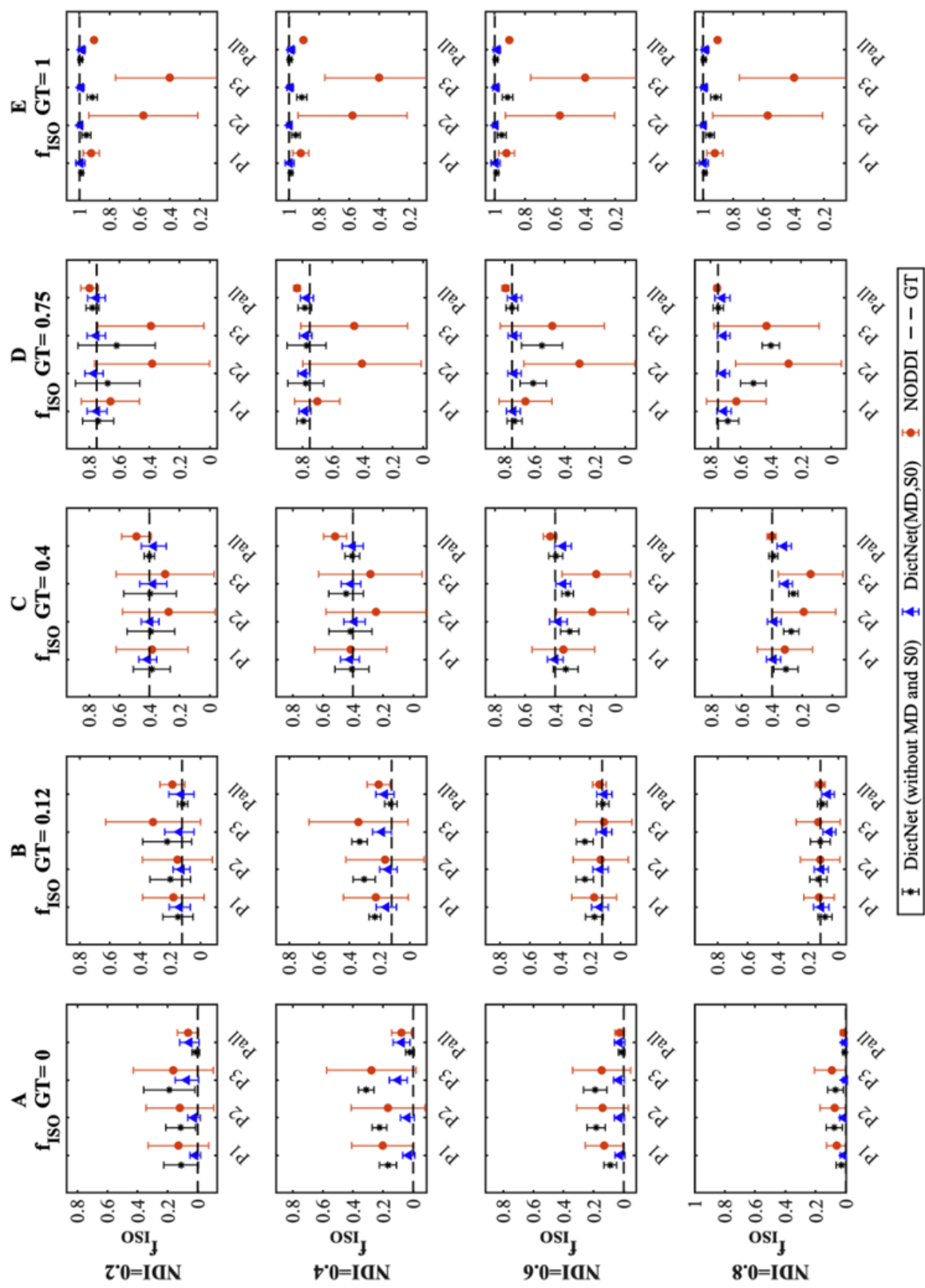


Figure 6.3: Comparison of DictNet with and without prior. Training for both cases involved identical optimization parameters and iterations.

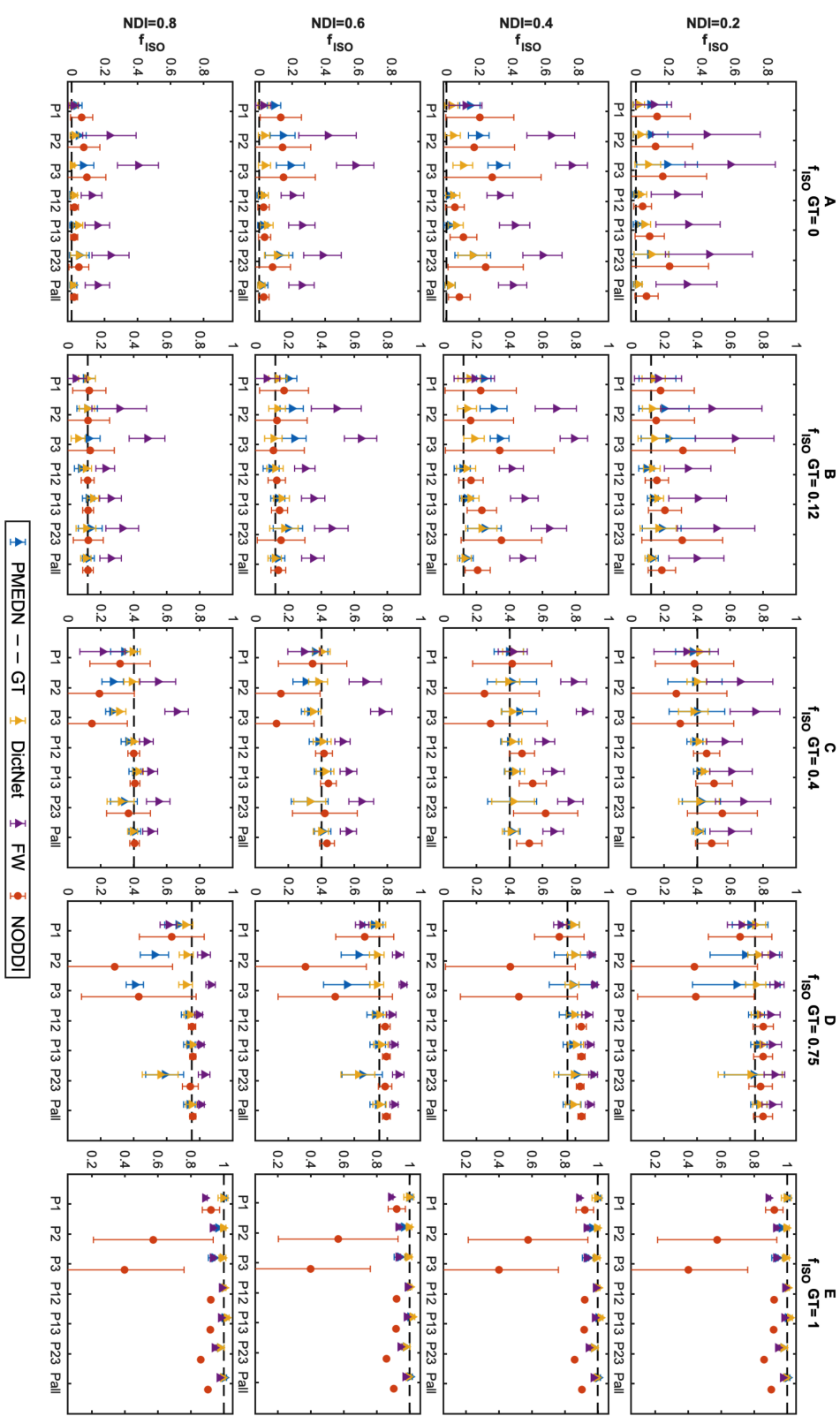


Figure 6.4: Dictionary-based network (DictNet) estimation of f_{ISO} at ground-truth values A) 0, B) 0.12, C) 0.4, D) 0.75, E) 1 (indicated with a dashed line) on the simulation test set with defined protocols P1, P2, P3, P12, P13, P23 and Pall for different NDI ground-truth values provided in Figure 5.6. DictNet generated f_{ISO} are compared with other methods such as NODDI, PMEDN, and .

Although, the extreme scenarios are unlikely in normal tissues in a healthy brain, it is not impossible to observe in neuro-pathogenic cases. Also, it is worth mentioning that such scenarios are not directly accounted for training single-shell DictNet. The evaluation of our single-shell approach with multi-shell NODDI suggests the results are ill-posed for both cases but identical. However, both (DLpN P1 & NODDI P12) are evidently better than single-shell estimation from original NODDI, shown in Figure-6.5.

6.4.2 *In-vivo*

In this section, high quality HCP and clinical HIV-CSVD cohort results are presented in three subsections. First, DLpN and NODDI results are shown with ground truth differences for subsequent single and multi-shell protocols. Here, the difference maps were computed referencing NODDI multi-shell as ground-truth. Then in 6.4.2.2, objective evaluation were done using Rician log-likelihood surrogate (Equation-6.2). Here, the objective function measures the similarity between reconstructed diffusion signal with scanner derived signal. In the last subsection, qualitative SNR comparison for single- and multi-shell reconstruction is done for two data-sets.

6.4.2.1 DLpN in High Quality HCP & Clinical HIV-CSVD

The *in-vivo* NODDI and DLpN reconstructions are visualized with their HSV colormaps (Section-3.2.2.1) in Figure-6.6. It demonstrates single-shell NODDI reconstructions are not reliable with original NODDI method. Their individual parameter maps and ground-truth difference maps are elaborated in Figures-6.7, 6.8 & 6.9.

Further, the parameter maps are individually analyzed with their difference maps to compare with the ground truth. Figure-6.7(A) represents f_{ISO} maps reconstructed

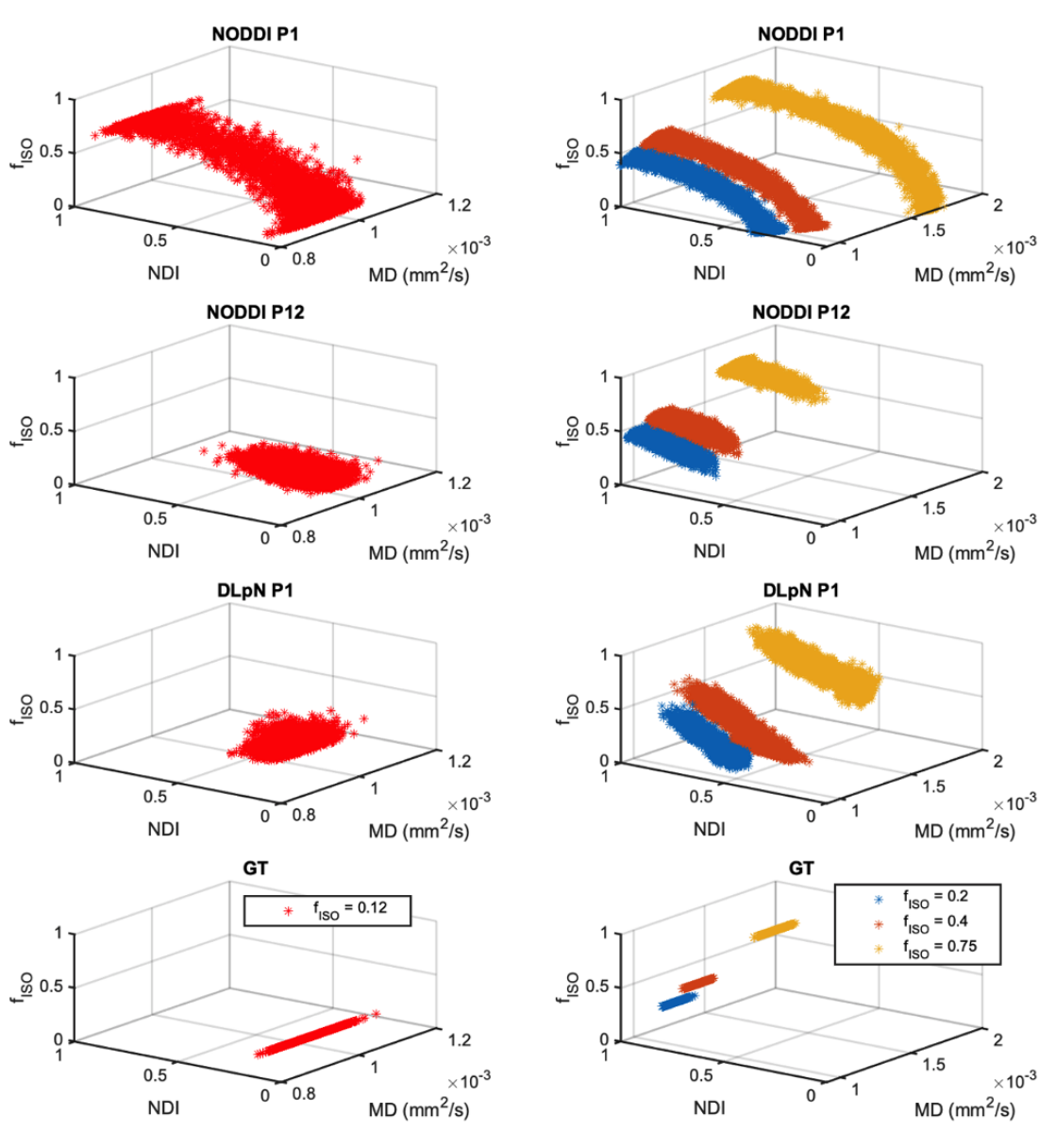


Figure 6.5: Extreme case estimation distribution for NODDI and DLpN, with ground-truth parameters shown for single-shell protocol P1 (i.e., $b=1000 \text{ s/mm}^2$) and multi-shell protocol P12 (i.e., $b=1000 \text{ s/mm}^2$ and $b=2000 \text{ s/mm}^2$). Left column represents high MD and high f_{ISO} cases corresponds to low NDI and normal f_{ISO} (i.e., NDI = 0.2, $f_{ISO} = 0.12$ in Figure 6.4) while right column represents normal MD and high f_{ISO} corresponds to the case of high NDI and high f_{ISO} (i.e., NDI = 0.8, $f_{ISO} = 0.4-0.75$ in Figure 6.4). Note GT: ground-truth.

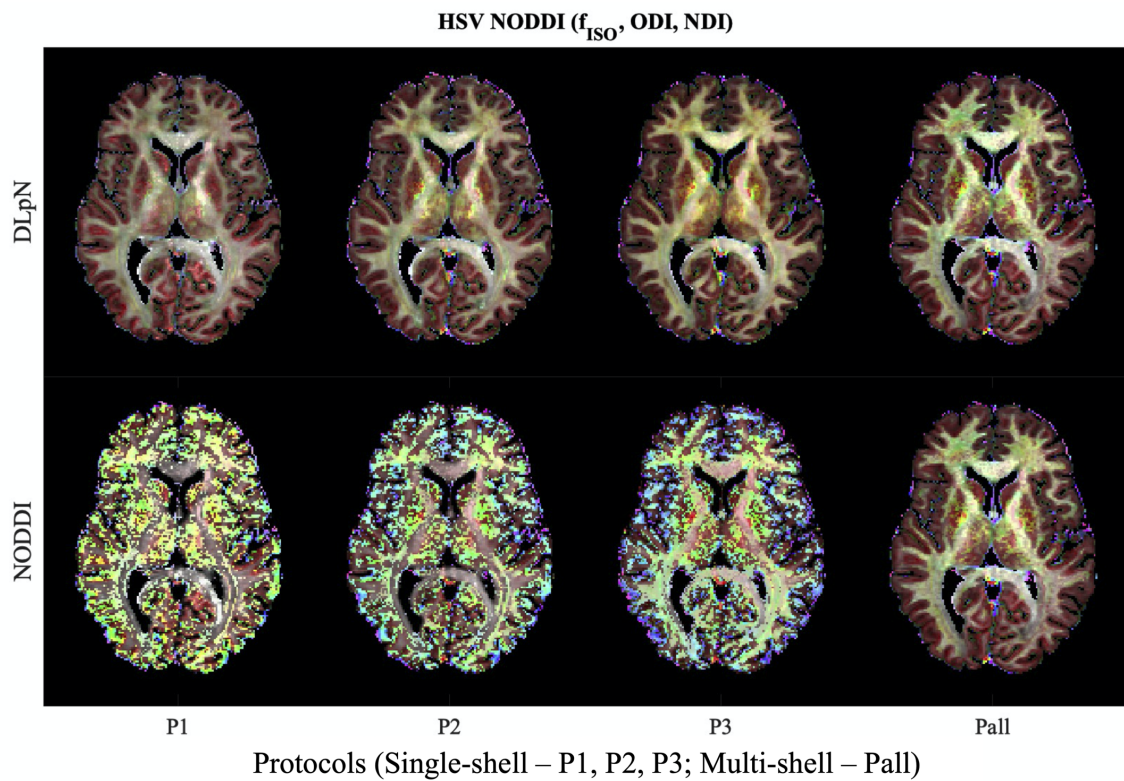


Figure 6.6: Combined parameter maps (f_{ISO} , ODI & NDI) are shown per protocol in HSV colorspace (Section-3.2.2.1), demonstrating single-shell and multi-shell reconstructions from DLpN and NODDI.

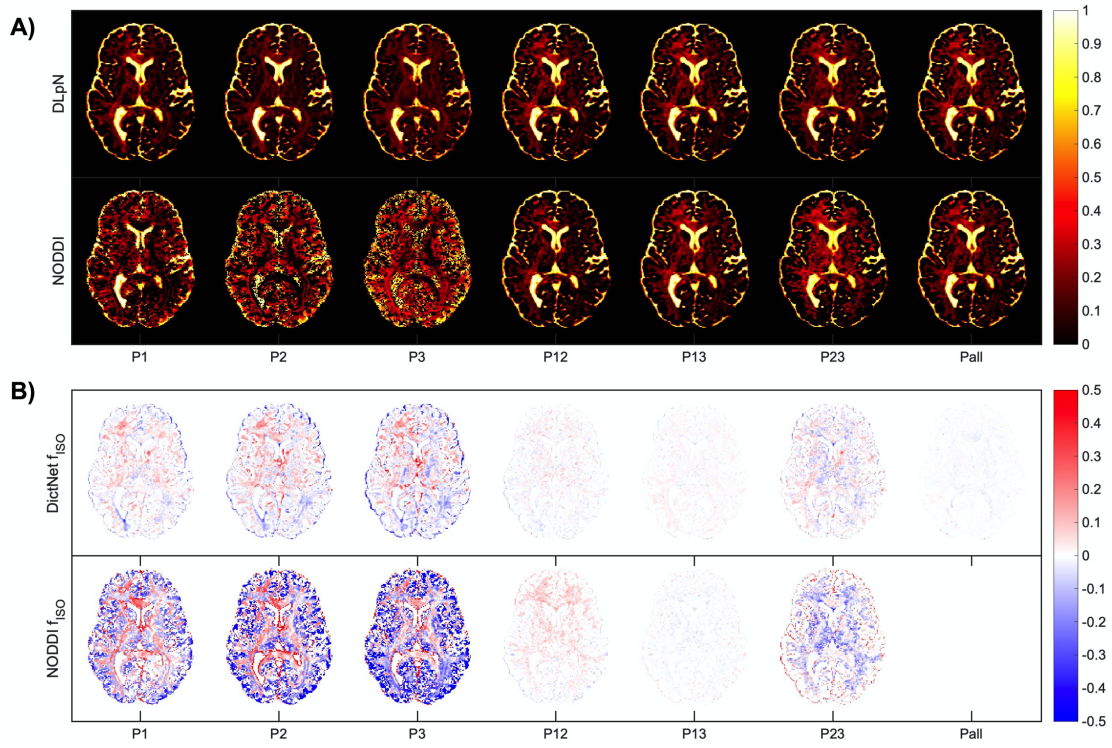


Figure 6.7: A) A representative axial view of the f_{ISO} maps estimated with proposed DictNet and NODDI for different protocols. Note, $NODDI_{Pall} f_{ISO}$ is considered as pseudo-ground-truth f_{ISO} and used as training data for DictNet; B) Difference maps for DictNet f_{ISO} and NODDI f_{ISO} with respect to $NODDI_{Pall} f_{ISO}$ for defined protocols. Intensity scales are shown.

using DictNet independently with priors, and NODDI for single- and multi-shell protocols. The f_{ISO} difference maps between the pseudo-ground-truth (i.e., $NODDI_{Pall}$) and DictNet along with NODDI with both single- and multi-shell are shown in Figure 6.7 (B). From the difference maps, it is evident that DictNet outperforms NODDI for single-shell protocols (P1, P2, P3) as well as for two-shell protocols (P12, P13, P23) with respect to the pseudo-ground-truth. Similarly, The NDI and ODI maps were shown for DLpN and NODDI fittings with different protocols in the human brain respectively in Figure 6.8(a)(A) and Figure 6.8(b)(A); and corresponding difference maps are shown in Figure 6.8(a)(B) and Figure 6.8(b)(B).

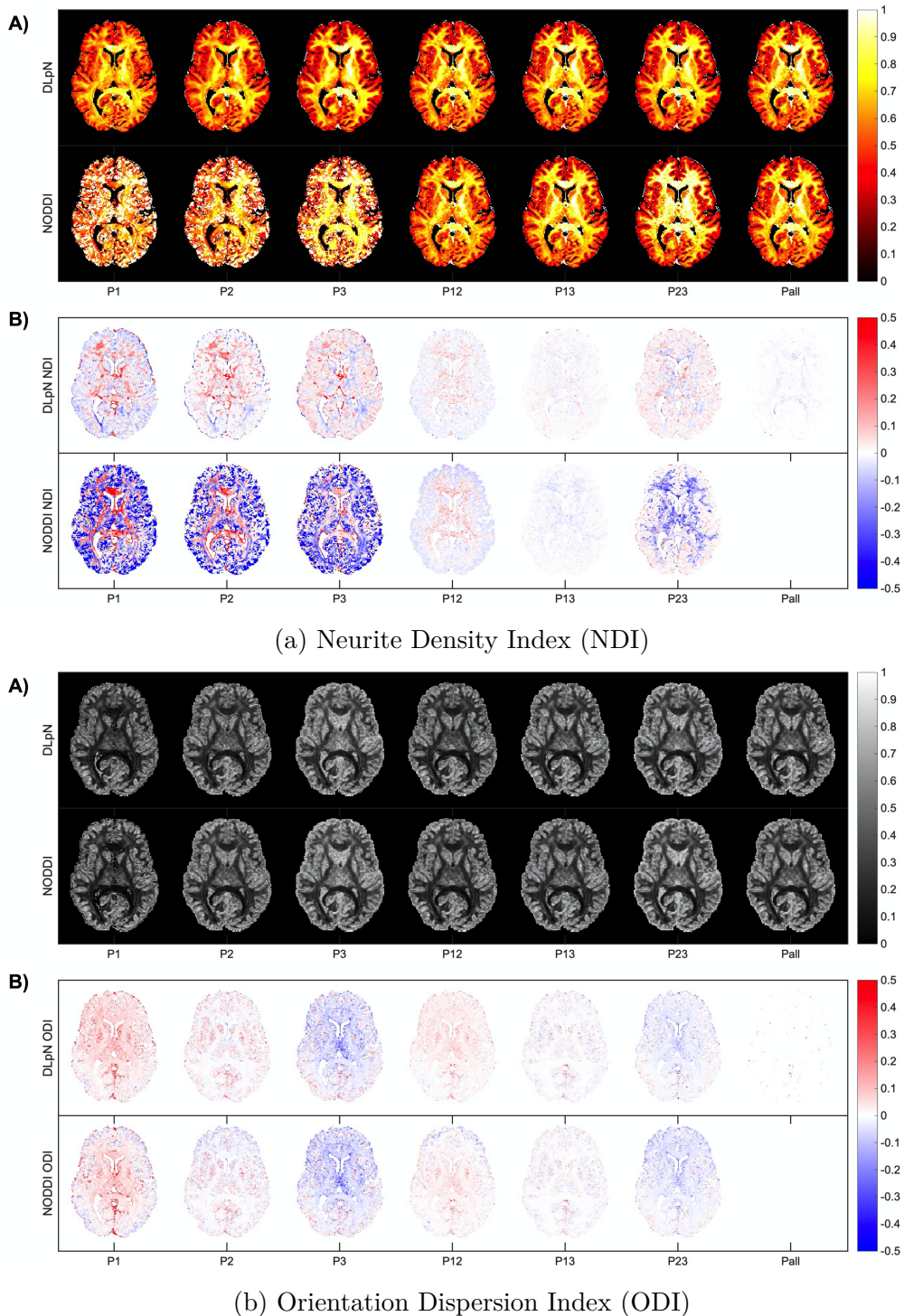


Figure 6.8: a) (A) A representative axial view of microstructural maps of NDI and (B) difference maps (with respect to $NODDI_{Pall}$) estimated with proposed DLpN and NODDI for different protocols on a human connectome project (HCP) subject. b) A representative axial view of microstructural maps of ODI and (B) difference maps (with respect to $NODDI_{Pall}$) estimated with proposed DLpN and NODDI for different protocols. Intensity scales are shown. Note, $NODDI_{Pall}$ is considered as pseudo-ground-truth for comparison.

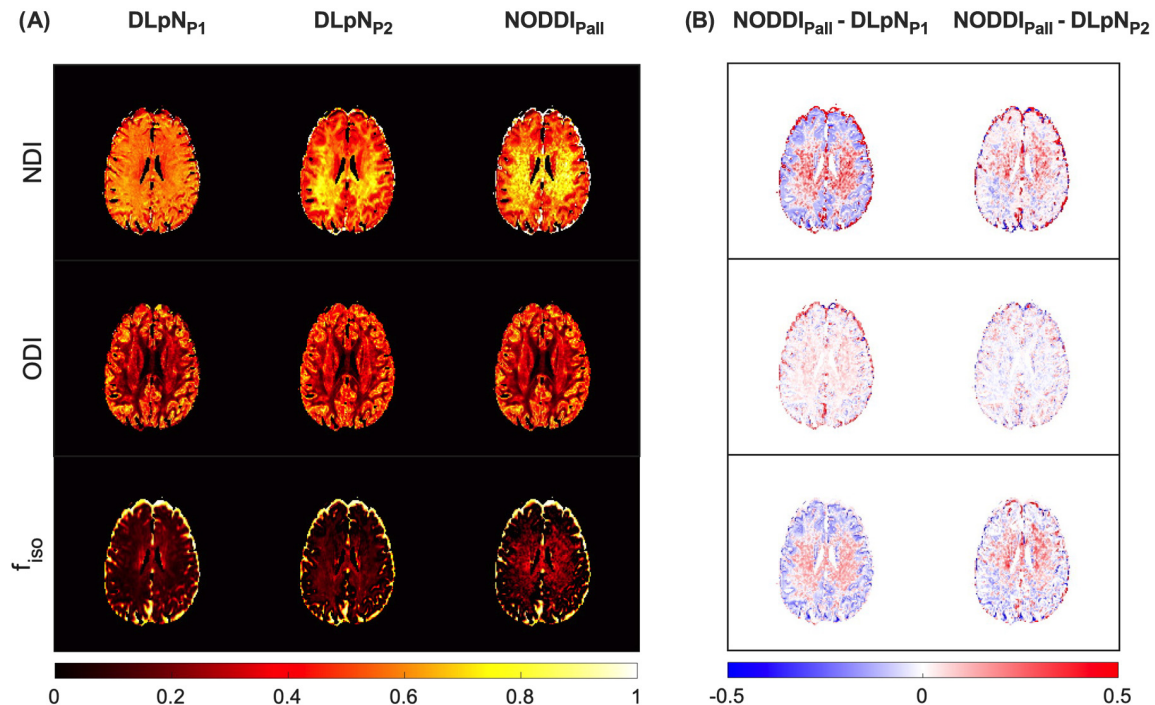


Figure 6.9: A) A representative axial view of the NDI, ODI, and fractional isotropy (f_{ISO}) maps estimated with proposed DLpN and NODDI for different protocols in CSVD. Note, $NODDI_{Pall}$ f_{ISO} is considered as pseudo-ground-truth f_{ISO} and used as training data for DictNet; B) Corresponding difference maps for DLpN-derived maps with respect to $NODDI_{Pall}$ for defined protocols P1 and P2. Intensity scales are shown.

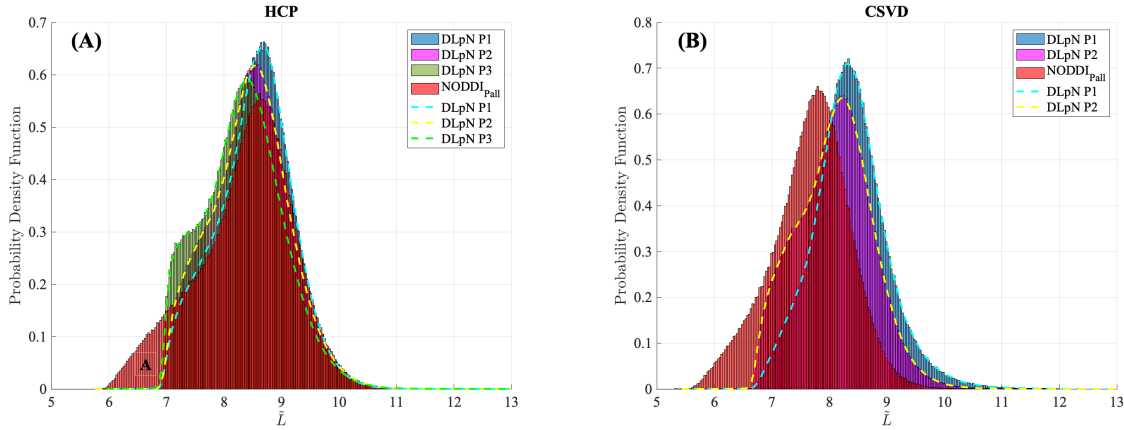


Figure 6.10: Log histograms for the objective values of DLpN P1, P2, P3 and $NODDI_{Pall}$ with (A) HCP and (B) CSVD test subjects. Positive direction along the x-axis corresponds to higher objective values. The goal for both NODDI and DLpN is to maximize the objective function. Region A is defined as the set of bins where the NODDI probability density function has lower objective values than DLpN

6.4.2.2 Objective Function Histogram Comparison

NODDI uses a Rician log-likelihood framework (Equation-5.1) to optimize the parameters. On the contrary, DLpN reconstruction was achieved in two subsequent stages utilizing mean squared error and Rician Log-likelihood objective function. Thus, it is relevant to observe the comparison of the Rician Log-Likelihood values in order to understand which technique and protocol scored the best objectively.

Objective Function Histograms for HCP and CSVD subjects were calculated with the objective function defined as the natural log distribution of the Rician log likelihood function, i.e.

$$\tilde{L} = \ln |L/N| \quad (6.2)$$

, where L is the negative Rician log likelihood described in Equation 5.1 and N is the number of diffusion gradients per protocol for normalizing the objective function for comparison. The higher objective value (\tilde{L}) indicates that the reconstructed micro-

parameters explain the scanner derived diffusion signal with greater accuracy.

From the definition of the objective function (Equation-6.2), the distribution that maximizes \tilde{L} can be said to have identified a better optimized set of NDI, ODI, and f_{ISO} . Objective evaluation of Figure-6.10 shows that for both HCP and CSVD reconstruction, $DLpN_{P1}$ had the highest distribution with maximum \tilde{L} , and then $DLpN_{P2}$ and $NODDI_{Pall}$, and the most poorly optimized case was found for $DLpN_{P3}$, probably due to lower SNR at higher b-value (Figure-6.1).

6.4.2.3 Signal-to-Noise Ratio (SNR)

SNR comparison demonstrates the visual improvement by utilizing single-shell data. In diffusion MR, T2-w (S0) image has the highest SNR and the SNR of different shell (b-value) is significantly different (Figure-6.1). This suggests data with higher b-value (lower SNR) may have difficulty reconstructing reliable metrics, since a lower SNR will affect the fitting quality. This is especially true for clinical cases. In clinical scenario, the HSV colormap of the combined parameters shows that the heavy noise in multi-shell derived parameters is qualitatively contrasting compared to single-shell. The improvement in Signal-to-Noise Ratio can also be attributed to the use of a high SNR T2-weighted prior in conjunction with single-shell estimation.

6.5 Clinical Validation of Single-Shell NODDI

Clinical validation is important in order to understand the accuracy and sensitivity of the parametric maps. This section aims to provide substantial evidence for clinical validation with single-shell NDI, ODI and f_{ISO} mapping. Initially to understand accuracy of using single-shell mapping, we demonstrate single-shell derived contrast in a White Matter Hyperintensity (WMH) case side by side with multi-shell derived

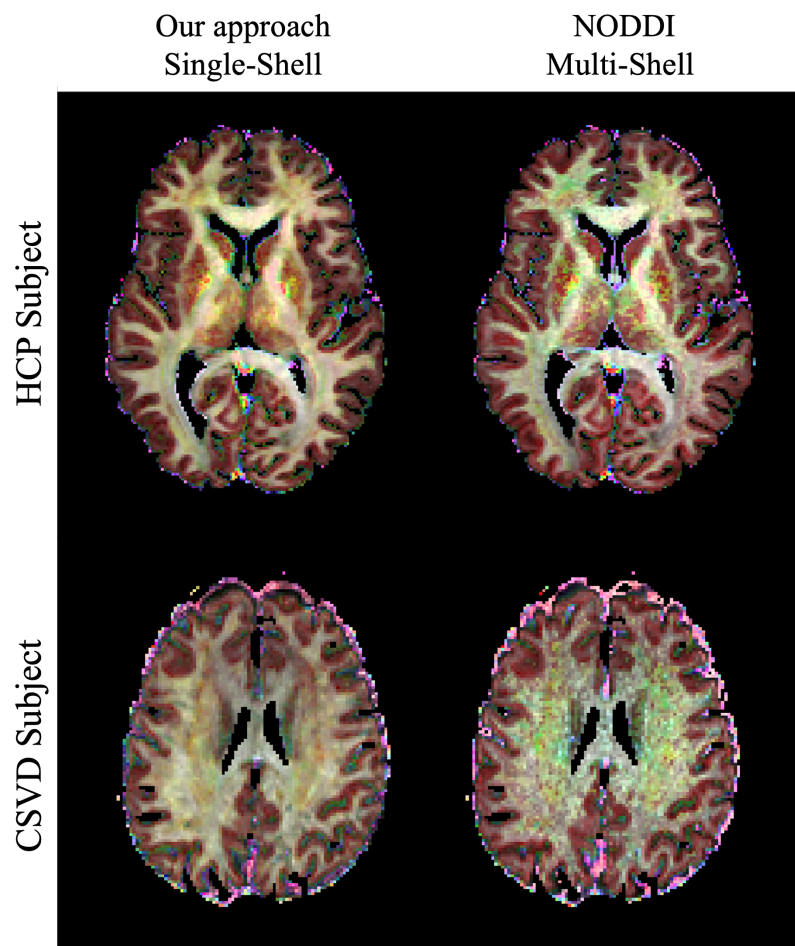


Figure 6.11: Qualitative SNR comparison between single shell and multishell NODDI

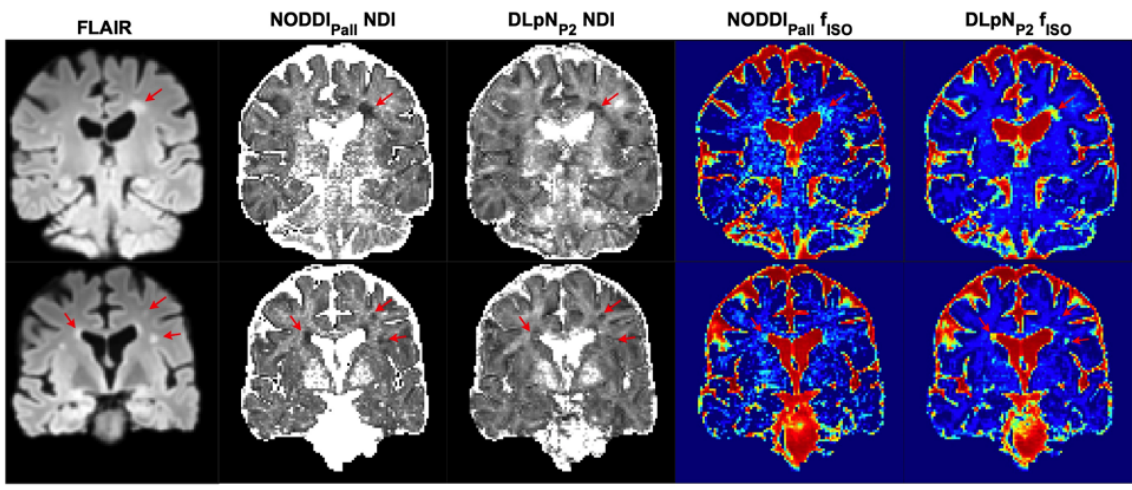


Figure 6.12: Comparison of DLpN derived NDI and f_{ISO} maps with $NODDI_{Pall}$ in CSVD

contrast, where our proposed approach holds the desired contrast compared with multi-shell NODDI. Then, mean percentage error and Pearson correlation quantifies the accuracy of the three parameters at Gray Matter and White Matter ROIs. Finally, we evaluate the sensitivity of our proposed approach by correlating the proposed single-shell reconstruction with aging and cognitive performance.

6.5.1 Single-Shell Contrast on White Matter Hyperintensity

A HIV-CSVD participant with WMH characterized by a Fazekas score [128] of 3, and hyper-intensity lesion volume of 1.77cm^3 was selected to demonstrate our single-shelled proposed contrast compared to multi-shell derived parameters. Figure-6.12 presents the NDI and f_{ISO} maps computed with $DLpN_{P2}$ and original $NODDI_{Pall}$, and corresponding T2 FLAIR images. Lesions in both NDI and f_{ISO} maps are clearly visible. Details are available in the Supplementary Materials (Figure S10-12) from [12].

6.5.2 Error (%) & Pearson Correlation of GM & WM ROIs

The performances of the single shell f_{ISO} with DictNet, and NDI and ODI with DLPN, have been assessed for both WM and GM by means of the percentage error (mean and standard deviation), as presented in Figure-6.13. The percentage errors are shown for all the parameters and protocols with respect to the pseudo-ground-truth NODDI_{all} parameters and reported as the mean of the ROIs. Single shell protocols (P1 and P2) had a roughly 5% error with a small variance in estimating NDI and ODI (Figure-6.13B and 6.13C). Comparisons of ROI mean values for six test subjects with DLPN and NODDI are reported in supporting figures S5, S6, and S7 (for f_{ISO} , NDI, and ODI, respectively) in the research study [12].

Pearson correlation analysis for JHU-ICBM WM and HO GM ROIs of the same test subjects showed strong correlations between NODDI_{all} and DLPN (Supporting Figure-S8 in [12]). Correlation coefficients for NDI with single-shell DLPN and NODDI_{all} are highlighted as follows: DLPN_{P1}, $r^2 = 0.875$; DLPN_{P2}, $r^2 = 0.927$; DLPN_{P3}, $r^2 = 0.944$. DLPN-based ODI maps also retained strong correlations with NODDI_{all} ($r^2 > 0.930$) and were found to be similar to those reported previously [8], for both single- and multi-shell cases. Scatter plots showing significant linear correlations between DLPN derived NDI, ODI, and DictNet derived f_{ISO} at different protocols (P1, P2, P3, P12, P13, P23 and Pall) with the ground-truth NODDI fitted with Pall protocol (NODDI_{all}). Asteric symbols indicate the mean of all the ROIs using John Hopkins University White Matter (WM) and Harvard Oxford cortical and sub-cortical gray matter (GM) atlases. Gray color indicates GM and blue indicates WM ROIs. Our proposed method showed very strong concordance with the pseudo ground-truth NODDI_{all} in single-shell and multi-shell protocols.

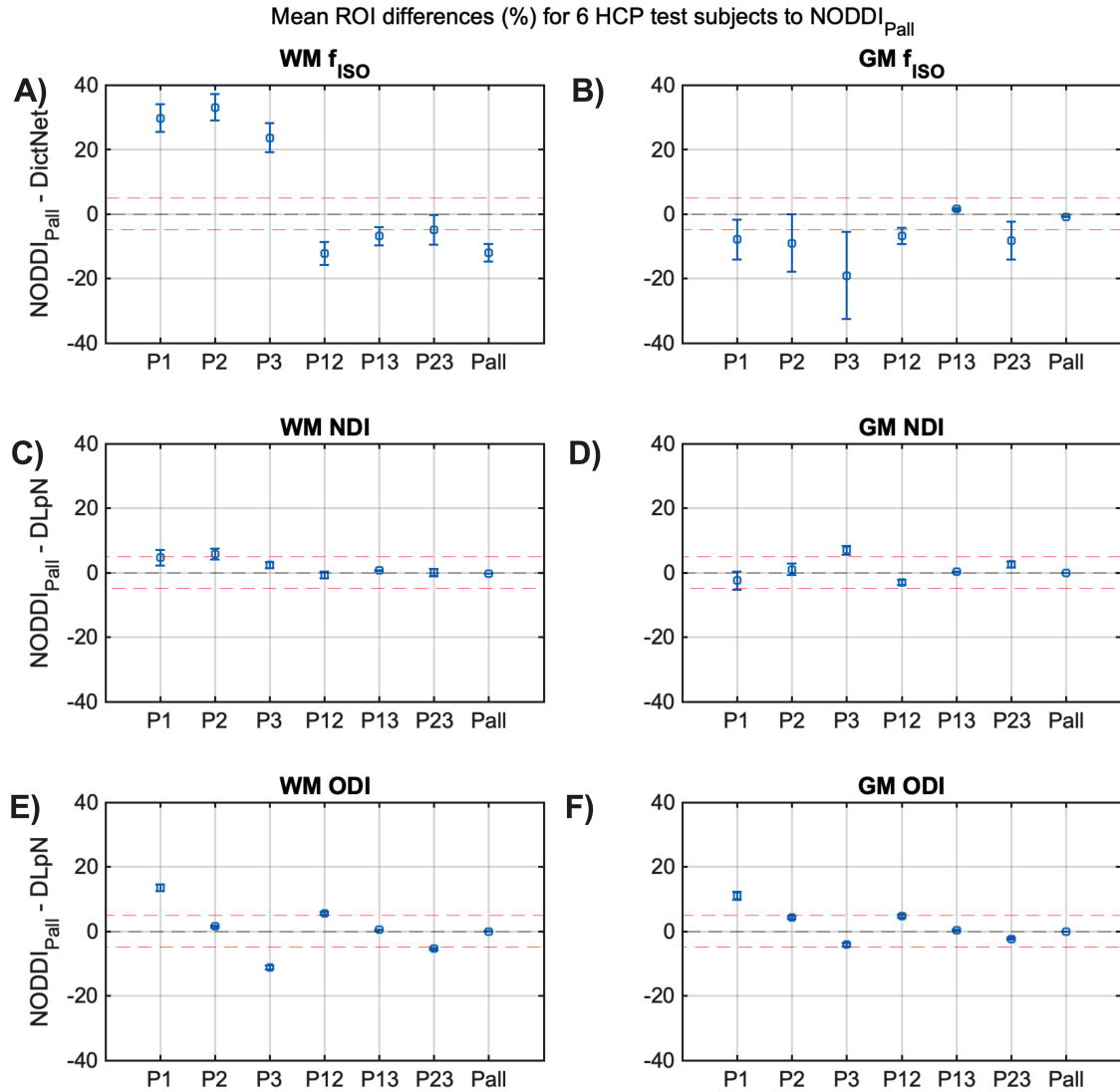


Figure 6.13: The estimation errors (%) from in vivo data in isotropic volume fraction f_{ISO} (A, B), neurite density index NDI (C, D) and orientation dispersion index ODI (E, F) for white matter (WM) and gray matter (GM) using DLpN single-shell protocols P1, P2, P3, and multi-shell protocols P12, P13, P23 and Pall. Errors were calculated with respect to the pseudo-ground-truth ($NODDI_{Pall}$) for six HCP test subjects.

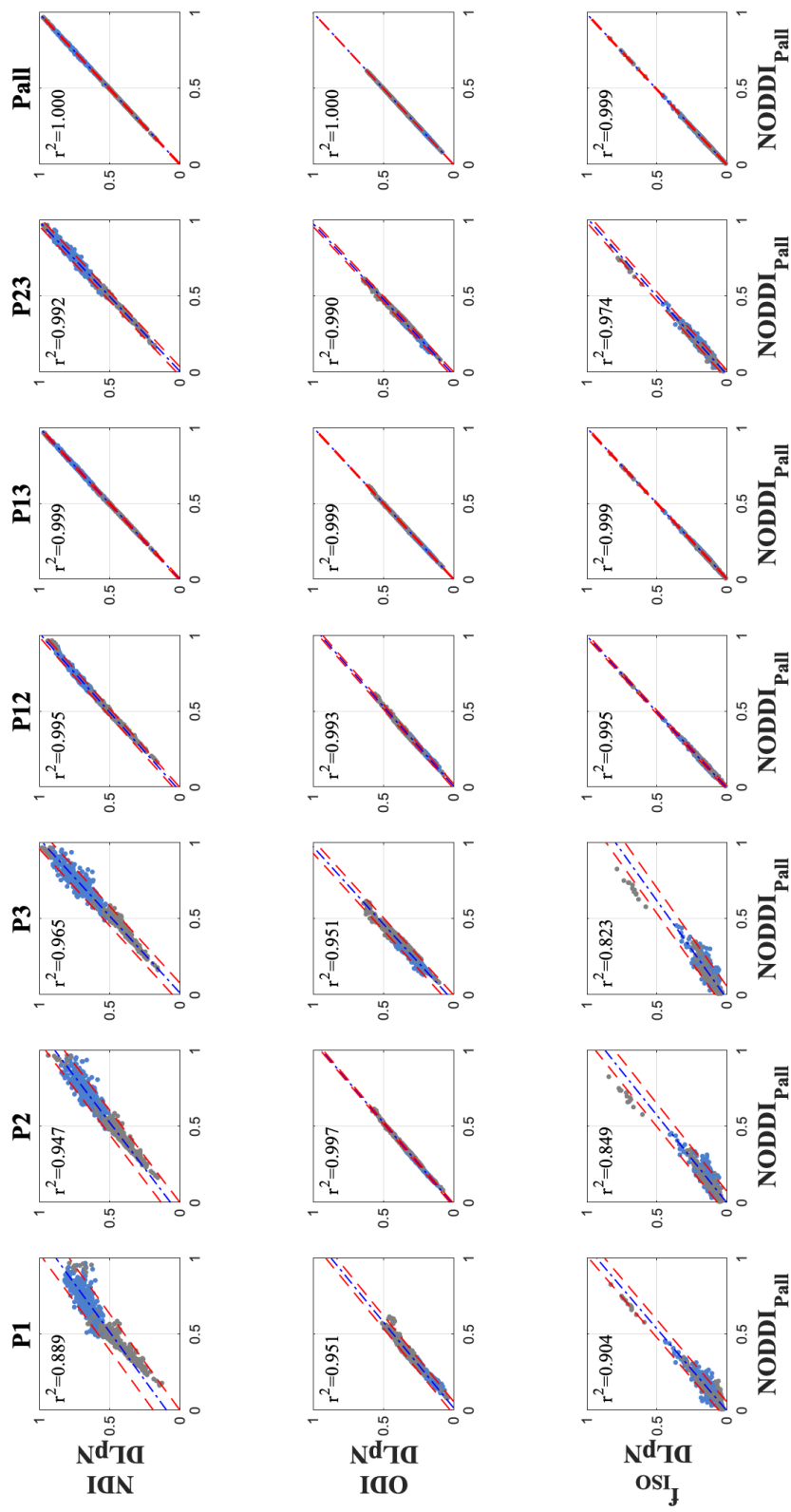


Figure 6.14: Pearson correlation with 8 HCP subjects using JHU WM (68) and HO cortical/sub-cortical GM (48+21) ROIs

6.5.3 Aging Vs Single/Multi-shell derived NDI, ODI & f_{ISO}

This section explores key insights from the comparison of aging with Single-shell and Multi-shell derived Neurite Density Index (NDI), Orientation Dispersion Index (ODI), and Fractional Isotropic volume (f_{ISO}) in gray and white matter tissue. Each plot in Figure-6.15, 6.16 & 6.17 shows a trend line for GM and WM with shaded areas representing the confidence intervals around these lines. The p-value and correlation coefficient (r) are provided for GM and WM in each plot. A p-value less than 0.05 and a higher absolute value of r indicates a stronger statistical relationship, highlighted in red box. The subject demographics details can be located in 6.2.2 (where P1 refers to $b = 1000s/mm^2$ and P2 refers to $b = 2000s/mm^2$).

6.5.3.1 Comparison of Single- and Multi-shell Derived f_{ISO} in Aging

Figure-6.15 presents the comparison between aging and f_{ISO} .

1. **Single-shell Derived f_{ISO} Shows Significant Correlation with Aging for both WM and GM** A statistically significant correlation is found between age and Single-shell derived f_{ISO} measures. Whereas the statistical sensitivity is diminished for multi-shell derived f_{ISO} .

2. **Fractional Isotropy(f_{ISO}) Increase with Aging:** A trend of statistically significant increase of f_{ISO} , a marker of neuroinflammation, with aging is observed in both GM and WM. The slope of free water increase in GM is higher than WM, congruent with histology.

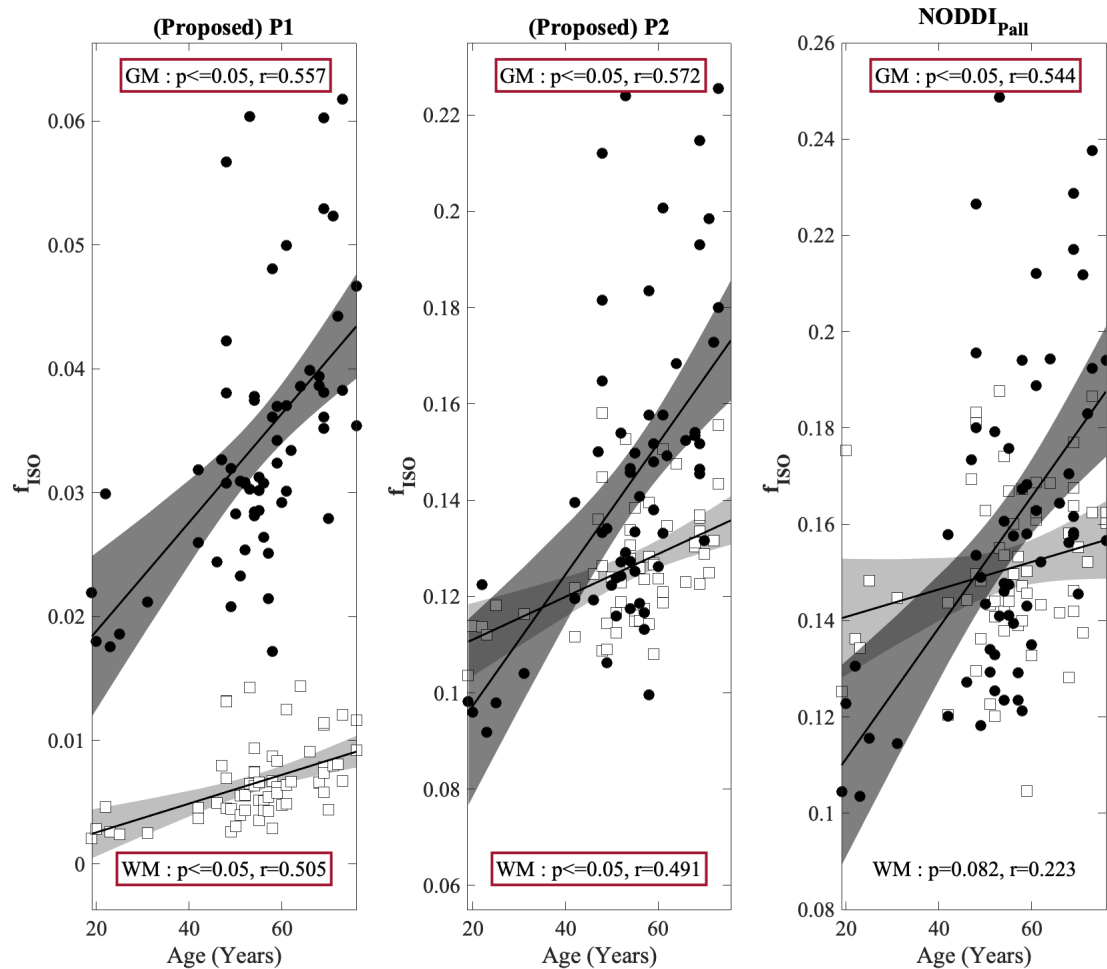


Figure 6.15: Correlation of mean f_{ISO} with aging from the combined JHU White Matter ROIs (squares) and combined Harvard-Oxford Cortical and Subcortical GM ROIs (circles)

6.5.3.2 Comparison of Single- and Multi-shell Derived *NDI* in Aging

Figure 6.16 presents the comparison between aging and NDI in both gray and white matter tissue in the brain.

- **Gray Matter NDI is Sensitive to Aging in Single-shell (P1)** A significant drop in GM NDI with aging is observed, particularly in low b-value NDI measurements, which supports the histological evidence in aging [1]. Multi-Shell(P12) NDI or High b-value (P2) Single-Shell NDI doesn't hold this sensitivity.

6.5.3.3 Comparison of Single- and Multi-shell Derived *ODI* in Aging

Figure 6.17 presents the comparison between aging and ODI in gray and white matter tissue in the brain.

1. **Trends of Single- and Multi-Shell ODIs are Closely Identical** ODI trends remain consistent across both single- and multi-shell which supports the ODI reconstruction observed in simulation in different protocols(Figure-5.7).
2. **Statistical Significance:** A statistically significant relationship between ODI and aging is observed in the WM tissue in both single and multi-shell reconstructions indicating WM is becoming more dispersed possibly due to the loss of fiber integrity, which is a common phenomenon in aging.

Our results provide substantial insights into the aging process at the microstructural level in the brain. The differential capabilities of Single- and Multi-shell NODDI in distinguishing between GM and WM properties, and their correlation with age, offer a nuanced understanding of brain aging. For single shell reconstruction, these

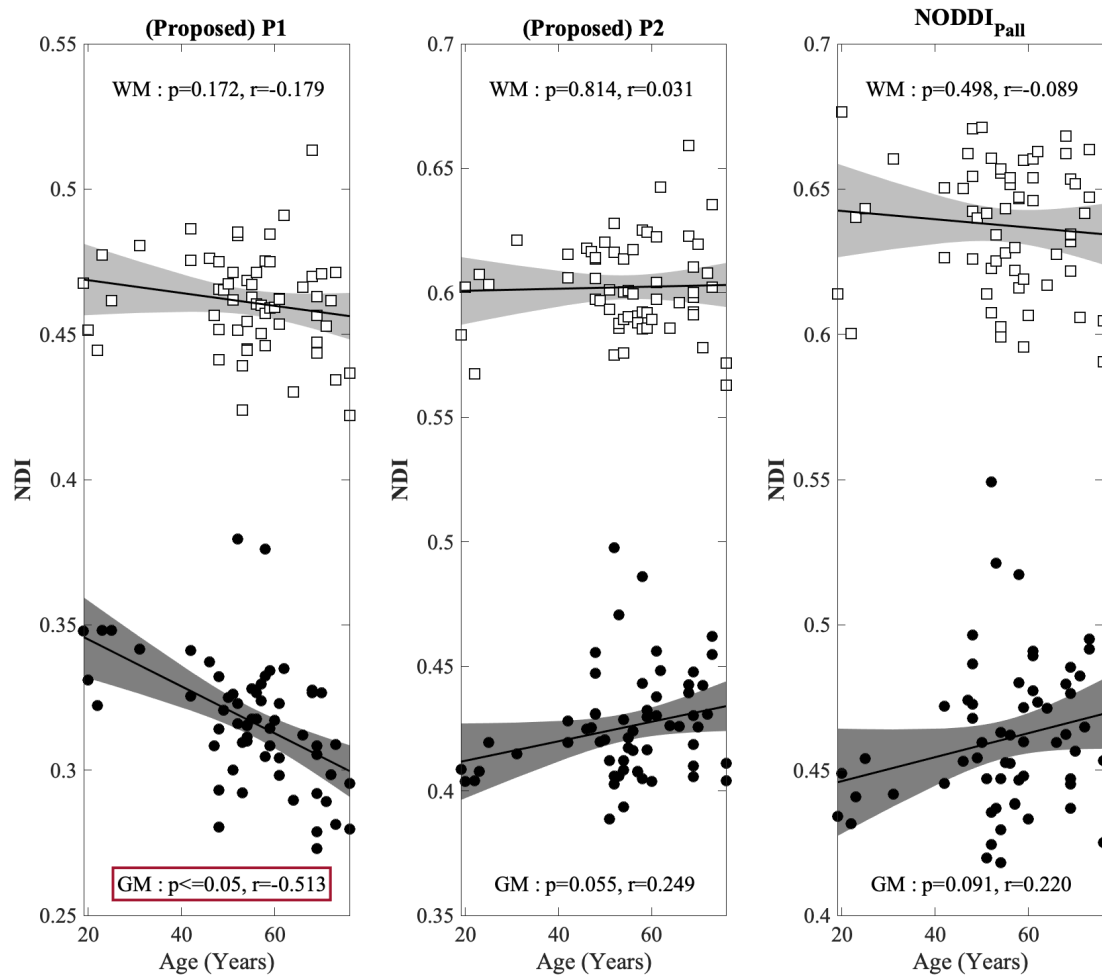


Figure 6.16: Correlation of mean NDI with Aging from the combined JHU White Matter ROIs (squares) and combined Harvard-Oxford Cortical and Subcortical GM ROIs (circles)

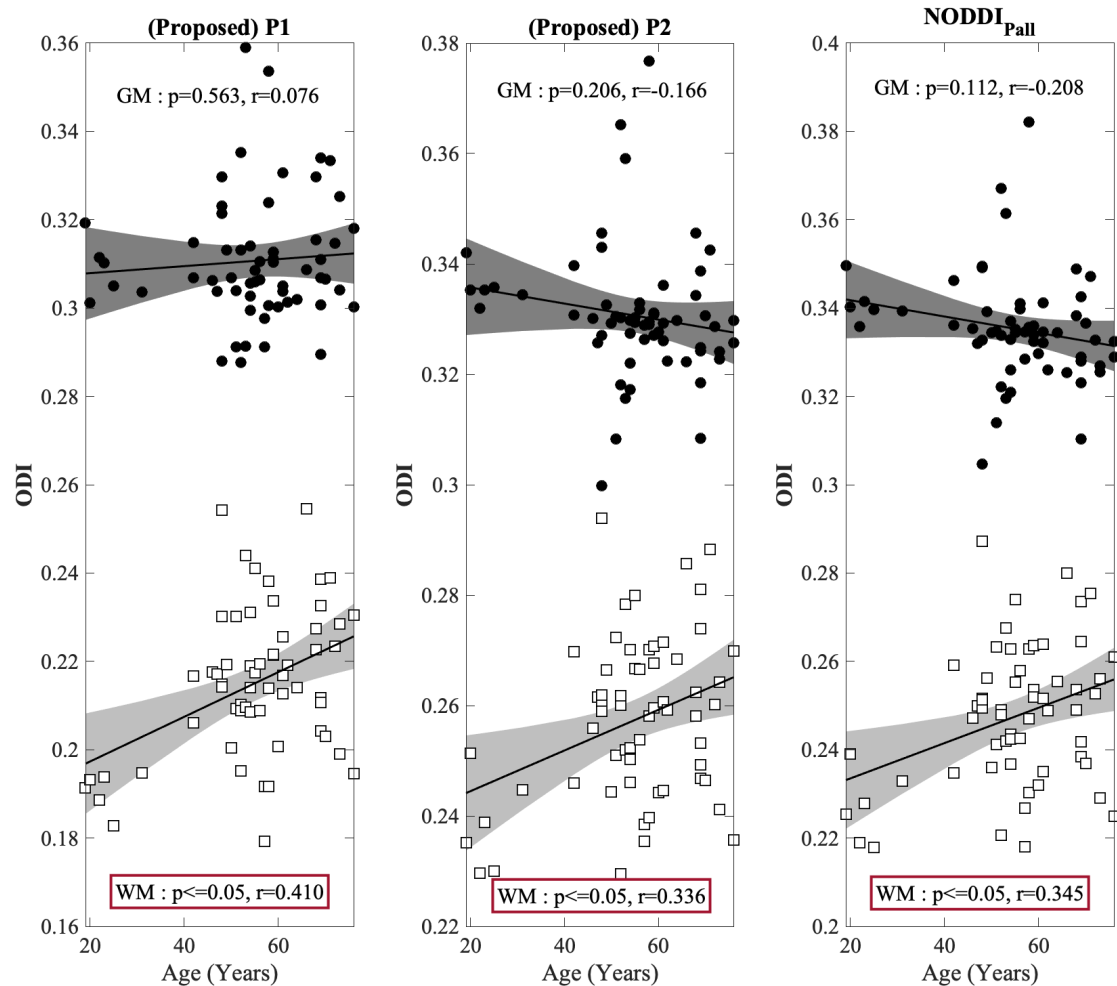


Figure 6.17: Correlation of mean ODI with Aging from the combined JHU White Matter ROIs (squares) and combined Harvard-Oxford Cortical and Sub-cortical GM ROIs(circles)

findings hold important implications for neuro-scientific research, potentially aiding in the early detection and monitoring of neuro-degenerative diseases.

6.5.4 Cognitive Scores of HIV+ & Control Subjects Vs Single & Multi-shell Derived NDI, ODI & f_{ISO}

This section explores the relationship between Single- and Multi-shell derived NODDI parameters and cognitive scores in HIV-positive and control groups, with a focus on gray and white matter tissue in the brain. Each plot in Figure-6.18, 6.19 & 6.20 shows a trend line for GM and WM with shaded areas representing the confidence intervals around these lines. The p-value and correlation coefficient (r) are provided for GM and WM in each plot. A p-value less than 0.05 and a higher absolute value of r indicates a stronger statistical relationship, highlighted in red box. The subject demographics details can be located in 6.2.2 (where P1 refers to $b = 1000s/mm^2$ and P2 refers to $b = 2000s/mm^2$).

6.5.4.1 Comparison of Single- and Multi-shell Derived f_{ISO} for Cognitive Scores

Key Observations:

1. In Multishell NODDI, no distinction is observed between GM and WM in f_{ISO} , which represents the histologically free water content. In contrast, Single-shell NODDI demonstrates sensitivity to this difference, typically showing higher free water content in GM than in WM.
2. An increase in free water content, indicative of neuroinflammation, has been observed to correlate with a decline in cognitive performance. This trend is especially evident in the HIV-positive group, where greater sensitivity to free water content in relation to cognitive performance (total z-score) is observed.

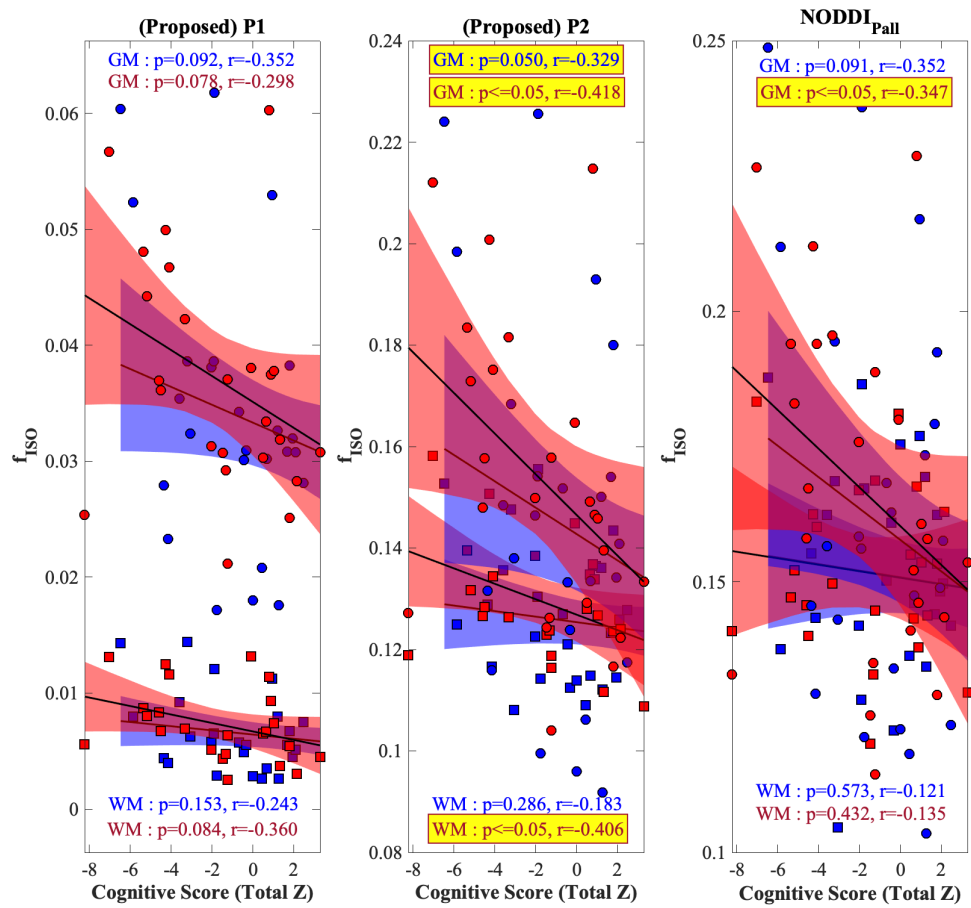


Figure 6.18: Correlation of f_{ISO} with Cognitive Scores of HIV+ and Control subjects using the combined JHU White Matter ROIs (squares) as Global WM and combined Harvard-Oxford Cortical/ Subcortical GM as Global GM ROI (circles)

6.5.4.2 Comparison of Single- and Multi-shell Derived *NDI* for Cognitive Scores

Key Observations:

1. NDI effectively differentiates between GM and WM in both single and multi-shell NODDI, as expected from histological characteristics.
2. In the HIV-positive group, a decrease in NDI correlates with higher cognitive performance, a relationship not observed in healthy controls. This trend is particularly prominent when low b-value single-shell derived NDI is considered, whereas multi-shell NODDI does not exhibit such trends or sensitivity.
3. This relationship is predominantly observed in GM, suggesting that low b-value single-shell NODDI may be more sensitive to changes in GM, also evident when analyzing age-related trends.

6.5.4.3 Comparison of Single- and Multi-shell Derived *ODI* for Cognitive Scores

Key Observations:

1. Both single- and multi-shell derived ODI display similar trends in the HIV and control groups within the CSVD-MRE cohort, aligning with findings from simulation studies.
2. For higher cognitive performance, a decrease in ODI for GM and an increase for WM is noted. Conversely, in HIV-positive subjects with lower cognitive performance, an increase in ODI for GM and a decrease for WM are observed, suggesting a lower adaptability scenario in these individuals.

These findings underscore the differential impact of HIV on brain tissue characteristics and cognitive function, as revealed through NODDI parameters. The distinct

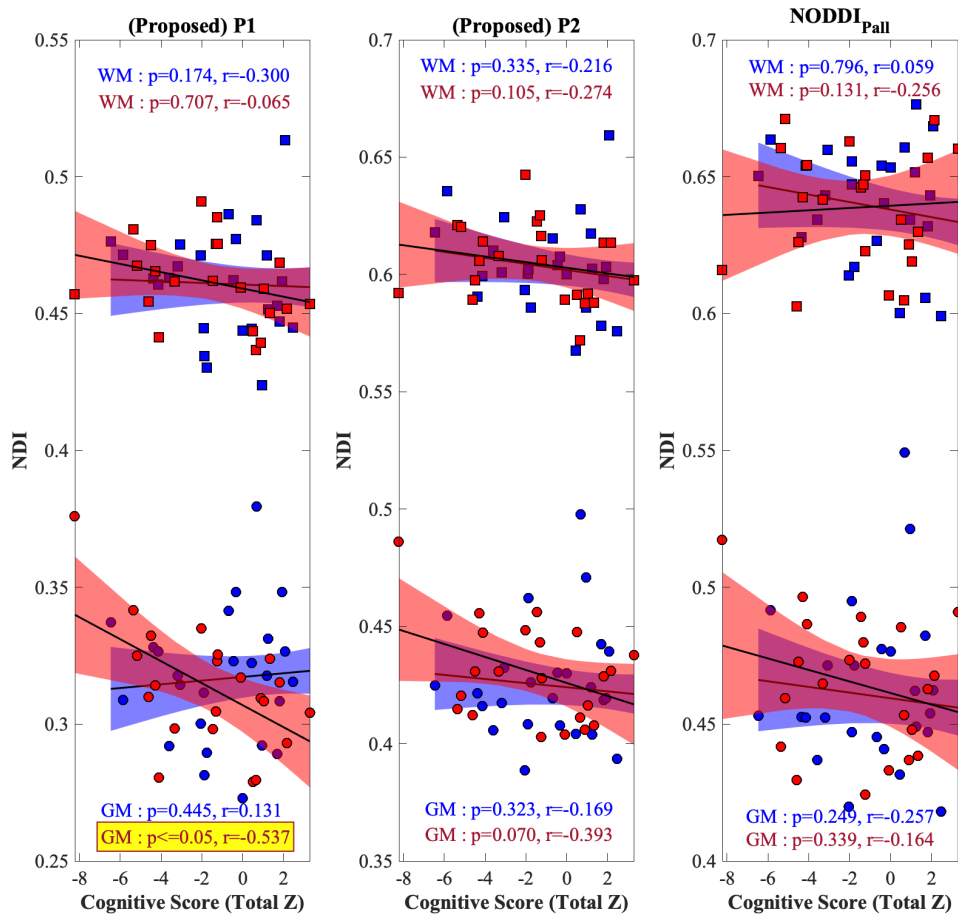


Figure 6.19: Correlation of NDI with Cognitive Scores of HIV+ and Control subjects using the combined JHU White Matter ROIs (squares) as Global WM and combined Harvard-Oxford Cortical/ Subcortical GM as Global GM ROI (circles)

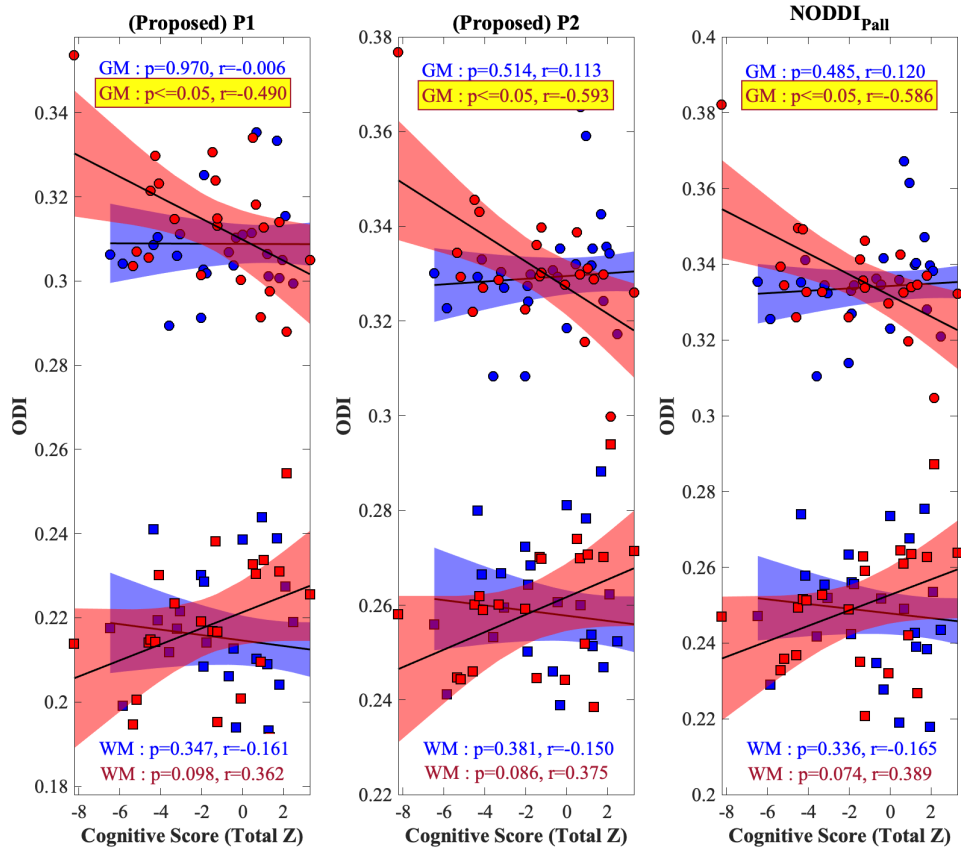


Figure 6.20: Correlation of ODI with Cognitive Scores of HIV+ and Control subjects using the combined JHU White Matter ROIs (squares) as Global WM and combined Harvard-Oxford Cortical/Subcortical GM as Global GM (circles)

patterns observed in HIV-positive subjects compared to controls highlight the potential of NODDI as a tool for understanding neurological changes associated with HIV.

In this work, we demonstrate that NODDI parameter maps such as NDI and ODI can be reconstructed from single-shell dMRI data using a dictionary learner estimated f_{ISO} as a prior. In order to generate f_{ISO} , we devise a network, that takes advantage of the IHT strategy used in recent studies [87, 122]. We propose a non-iterative scheme of IHT where a constant stochastic layer determines the learning of dictionary coefficients by the spatial-angular sparse dMRI data from the simulated dataset based on the protocol obtained from the in-vivo data. The generated coefficient vector contributes to a fully connected feed-forward network to estimate the f_{ISO} . The network incorporates important determinants of f_{ISO} priors [129] i.e. MD and, T2w signal S0 that facilitates single-shell estimation of f_{ISO} with NODDI based data-driven learning. The overall procedure drastically reduces memory requirements and training time compared to the deep learning approaches (used to reduce gradient directions in NODDI) [87, 122], and preserves the estimation accuracy and precision in estimating f_{ISO} compared to the ground-truth data.

Using both simulation and in-vivo data experiments, we evaluated the feasibility of our proposed DLpN approach for single-shell NODDI parameter mapping and compared the results with the multi-shell $NODDI_{Pall}$. The results from both experiments indicated that single-shell NDI and ODI reconstructions are possible with good accuracy in WM and GM ROIs. Our simulation results revealed that DictNet generated single- and multi-shell f_{ISO} values were stable whereas, on the same dataset, NODDI showed ill-posed behavior in f_{ISO} estimation in several cases likely due to NODDI model constraint. That is, in the NODDI fitting, higher f_{ISO} regions have

shown to be explained with higher ODI values, that influences the f_{ISO} contribution as well as NDI. Calculating the f_{ISO} from the dictionary instead of grid search shows that the log-likelihood objective function can be better optimized, and also allows for single-shell fitting reliably in the process. DLpN based NDI and ODI reconstructions for single-shell protocols are very close to the ground-truth values and consistently outperformed the original NODDI fittings. In addition, comparison of the simulation of DictNet derived f_{ISO} with bi-tensor model-based FW (both for single- and multi-shell), deep learner based PMEDN and NODDI in different protocols show that DictNet derived f_{ISO} estimation is stable with single-shell P1 and P2 protocols, compared to that of other approaches (Figure 6.4). It is because these approaches do not incorporate either S0, MD, or dictionary accounted for simulated complex tissue microstructure.

Using the in-vivo HCP data, we found that DLpN based single-shell NDI values had around 5% difference compared to the pseudo-ground-truth $NODDI_{Pall}$ in WM and GM for single-shell protocols (i.e., P1, P2 and P3). Interestingly, overall NDI and ODI results suggest that, P2 had a minimum error for both ($\sim 5\%$), even when it showed to have a higher difference with our estimated f_{ISO} prior ($\sim 30\%$) but our f_{ISO} prior retained strong correlations ($r^2 > 0.85$) with the same pseudo-ground-truth $NODDI_{Pall}$ (Figure 8 and Supplementary Figure S8). This means that $DictNet_{P2}$ identified a different (mean-shifted) set of f_{ISO} based on the built dictionary which retained the similar solution for NDI and ODI with $DLpN_{P2}$ similar to $NODDI_{Pall}$. The comparison of objective function histograms between DLpN and NODDI for the example test subject highlights this point (Figure 6.10). In addition, we show that a set of voxels in $NODDI_{Pall}$ optimization has lower objective values (region A), where the goal for all the approach was to maximize this objective function. $DLpN_{P2}$ derived NDI, ODI and f_{ISO} parameters resulted in a very similar objective function

histogram when compared to $NODDI_{Pall}$, except region A where NODDI performed poorly. As $DLpN_{P2}$ shows to reconstruct similar NDI and ODI maps as $NODDI_{Pall}$ (difference $\sim 5\%$) and multi-shell fitting noise gets reduced in the process. Therefore, $DLpN_{P2}$ is recommended to create single-shell NDI and ODI maps given training protocol as $Pall$. Possible reasons for biases in single-shell P1 and P3 include the following: firstly, DLpN ODIs obtained in P1 and P3 are relatively different from $NODDI_{Pall}$ observed from the simulation (also reported in previous study [8]) and resemble P2 or the middle protocol used in the $Pall$. Secondly, $DictNet_{P3}$ derived f_{ISO} estimation was not stable in simulation, due to the fact that higher b-value images have lower SNR. This also explains why the $DLpN_{P3}$ objective histogram is seen to be left skewed compared to $NODDI_{Pall}$, suggesting there were a large number of voxels that were not well optimized in $DLpN_{P3}$. Based on our simulation results, $DictNet_{P1}$ and $DictNet_{P2}$ derived f_{ISO} values were shown to be stable in simulation. But for the in-vivo experiment, P2 performed best in generating parameter maps close to the pseudo-ground-truth (i.e., $NODDI_{Pall}$ derived NDI and ODI maps). In case of P1, we saw P1 based ODI estimation was strongly correlated but different (mean-shifted) compared to $Pall$ based ODI. Yet interestingly, P1 based optimization has shown to yield better objective values than $NODDI_{Pall}$. But if we focus on reconstructing $NODDI_{Pall}$ equivalent NDI and ODI as they are histologically validated [130], $P2$ based DLpN is the approach to take with $Pall$ based training data. Nevertheless, the high correlation of $DLpN_{P1l}$ maps with $NODDI_{Pall}$ suggests the possibility of histological correlation to hold valid for $DLpN_{P1l}$ as well, and a subject for future study.

So, to compare DLpN derived NDI and ODI with any other NODDI based studies, it is recommended to use the middle protocol, i.e., in our case, P2 when DLpN is trained with $Pall$ (comprising of P1, P2 and P3). We hypothesize observing from the training pattern that to enable multi-shell equivalent reconstruction on P1, we will

need to change the training data protocol. That is, we will need to acquire training data with a b-value lower than P1 and another shell with b-value higher than P1. This will be further investigated on relevant datasets and should potentially allow the clinical cases with P1 to perform NODDI investigation.

As an exploratory analysis, we investigated a clinical cohort with CSVD (a low SNR dataset). As expected, DLpN derived single-shell maps showed high concordance with the pseudo-ground-truth $NODDI_{Pall}$ especially for P2 protocol. In addition, it is evident that $DLpN_{P2}$ is highly conspicuous for the lesions in both NDI and f_{ISO} maps than the original NODDI approach.

Major advantages of the DLpN approach are follows: first, NDI and ODI maps can be further improved with DLpN if independent f_{ISO} can be better estimated by leveraging phantom based f_{ISO} studies in future with single- or multi-shell cases. Second, the use of a single-shell protocol would reduce the scan time by more than 50% compared to the standard NODDI acquisition. Thus, this approach might be useful to obtain NDI and ODI reconstructions using a clinical scanner and in a clinically feasible acquisition time for cases such as stroke, pediatric or emergency subjects with sufficient resolution. Third, the DLpN approach may be applied retrospectively on the existing data collected with a reasonable number of diffusion directions and appropriate b-value (say $b=1000\text{ s/mm}^2$). However, prerequisites for using the existing dataset are that two additional subject scans are required with the same scan parameters with 3-shell protocol to train for f_{ISO} with the test case single-shell protocol as the middle protocol of the multi-shell training set. This study has some limitations. Firstly, the parallel diffusivity in the NODDI toolbox was not optimized for GM regions which is recommended in the previous works [131, 132] to obtain better outcomes for the cortical areas, which can be accommodated in the future experiments. Secondly, the nature of clinical dataset used was particularly focused on CSVD, fur-

ther disease cases need to be explored in future for further validation of the approach. However, as the training is performed voxel-wise, we expect to see similar results on other disease cases with low resolution clinical dMRI datasets. Thirdly, the DLpN processing time is currently 10 to 13 hours whereas the original NODDI model requires 20 to 30 hours to process on our multicore setup (Parallel 24 cores). However, AMICO setup with our single-shell DLpN approach should be able to reduce the NDI and ODI processing time down to <30 minutes. This work could be further extended to account for a reduced number of diffusion gradients, and incorporating quantitative T2 maps with advanced machine learning approaches.

6.6 Conclusions

In this chapter, we have solved the ill-posed single shell NODDI problem utilizing clinically available prior that closely relates to water density in the brain. We proposed to use a dictionary-based approach incorporating T2-w (S_0) and Mean Diffusivity prior that provides a reliable prior to independently estimate fractional isotropy(f_{ISO}) that enables neurite based quantification. We have demonstrated that single-shell based neurite density, fractional isotropy and orientation dispersion holds clinical contrast in low and high b-value settings (shown in a white matter hyperintensity case study). Initial result has shown positive results in high quality HCP data, and finally, application in clinical HIV-CSVD cohort is demonstrated. The sensitivity of the method was demonstrated on an aging population and cognitive performance of the population accompanied by Pearson correlation of white and gray matter ROIs. Current clinical cohort included 66 subjects, where well distributed age group is required in future to establish our findings.

Single-shell neurite and fractional isotropy quantification have been deemed as

a physically ill-posed problem. To our knowledge, our study is the first to take a systemic approach in solving this problem. We have solved the problem in two stages; with the utilization of clinically informed prior with AI, our work is the first to demonstrate sensitivity of single-shell neurite and fractional isotropy in an aging scenario, and further in cognitive performance decline with HIV neuro-inflammation.

Chapter 7

Summary of Contributions & Future Directions

7.1 Summary of Key Results

In this study, we have proposed to use AI with geometrical and multi-modal context in order to recover lost microstructural details from limited Q-space resolution in single-shell protocols with DTI and NODDI. Diffusion is a well observed phenomenon in the brain, and can be measured non-invasively with diffusion sensitive protocols with MRI but clinical dMRI suffers from lower angular resolution and singular b-value samplings that limits the retrievable microstructural details. Our preliminary objective was to recover clinical details from a lower angular resolution diffusion data in DTI. Then single-shell problem of NODDI was studied in a synthetic data simulation. Retrieving cues from the simulation, multi-modal priors was used to recover multi-compartments in NODDI. The investigation resulted in the following findings:

In Q-space up-sampling task,

- The clinical group differences for axial and mean diffusivity could be reliably retrieved with the proposed approach when utilizing geometrical context of

Q-space. Comparison with different techniques showed that False Positive outcomes from the clinical differences increased for the methods that did not directly utilize geometrical context from the Q-space.

- In Medical Imaging, scarcity of training data limits the data-driven learning in clinical studies. For dMRI, we observe that leveraging geometrical context of Q-space helps reduce the burden on the availability of training samples significantly.

In Single-Shell NODDI estimation,

- Synthetic data simulation revealed that single-shell NODDI can be conditioned with free water compartment in order to solve for Neurtie Density Index and Orientation Dispersion Index parameters.
- Simulation experiment further disclosed that the conditioning parameter f_{ISO} could not be retrieved without the help of multi-modal maps that related with free water compartment of tissue in single-shell.
- Comparison of theoretical objective function of single and multi-shell reconstruction of NODDI validated the reliability of estimated reconstruction.
- Single-shell estimated fractional isotropy showed greater sensitivity increasing with age in the Global White Matter and Gray Matter Regions. Further qualitative maps of clinical White Matter Hyperintensity Regions demonstrated expected contrast for neurite density index and fractional anisotropy.

7.2 Discussion

7.2.1 Retrieving Lost DTI-based Microstructure Differences

DTI (Section-3.2.1) metrics are computed after acquisition of diffusion signals in different spatial directions. The number of directions used in DTI computation are vital in capturing microstructure differences in different disease cases. Use of higher number of directions is often limited in clinical diffusion data acquisition because of urgency and clinical priorities of other modalities. However, it is evident (Figure-4.1) that statistically significant differences observed with higher angular resolution is lost in lower resolution DTI metric. Thus, different AI techniques have come forward to up-sample the Q-space.

Different AI (ML/DL) approaches have shown to improve visual image quality, but clinical validation was necessary to consciously make sure we are not making the reconstructions subject to hallucination. In this study, we have put forward an approach that uses the angular context of the Q-Space to up-sample Q-spaces of 50 Episodic and 50 Chronic Migraine patients and investigates the differences retained with the up-sampled reconstruction comparing different AI techniques. Global scoring metric was designed with true and false positive scores based on ROIs and TBSS WM fiber skeleton (Family wise corrected p-value reported). False positive scores was used to penalize the different methods.

The comparison revealed that our approach with Q-space angular context performed the best in resolving the lost clinical differences. The proposed approach also used the lowest training resources made available in the data-set, Only 5 training and validation data from healthy controls enabled test results on the chronic and episodic migraine population.

7.2.2 Retrieving Neurite & Extracellular Sensitivity with Single-Shell NODDI

NODDI is a practical biophysical model, built on the assumption that the neurites/dendrites and extracellular free water have constant diffusivity; and its objective is to quantify fractional compartments that results the final scanner derived diffusion signal. However, single-shell NODDI doesn't fit well and described as an ill-posed problem in the literature. Thus, it was not possible to quantify neurite information in clinical dMRI.

In this study, we examine the behaviour of NODDI under conditioned assumptions in simulation using single- and multi-shell data. Our simulation study has shown that holding extracellular f_{ISO} as prior, we are able to distinguish the neurite compartment volume and neurite dispersion, approximated to the ground truth data. This led to the necessity of independent approximation of f_{ISO} , which failed when using only single shell data. However, using clinically available multi-modal contrasts (that related to tissue water density), we were able to retrieve extracellular free water map using only single-shell data both in simulation and *in-vivo*. The mapping was done using a dictionary based approach motivated from PMEDN.

We studied the aging and cognitive scores relating to single- and multi-shell derived neurite volume, dispersion and extracellular free water metrics from 60 clinical subjects. We have observed clinically meaningful and sensitive changes in aging gray and white matter using single shell NODDI (using DLpN), especially with neurite density and free water. The orientation dispersion results were as similar to multi-shell. Our approach resulted in higher sensitivity in gray matter to aging with single shell data. Lower b-value single shell retrieved higher clinical sensitivity for neurite volume in GM, which supports the result of the objective function histogram com-

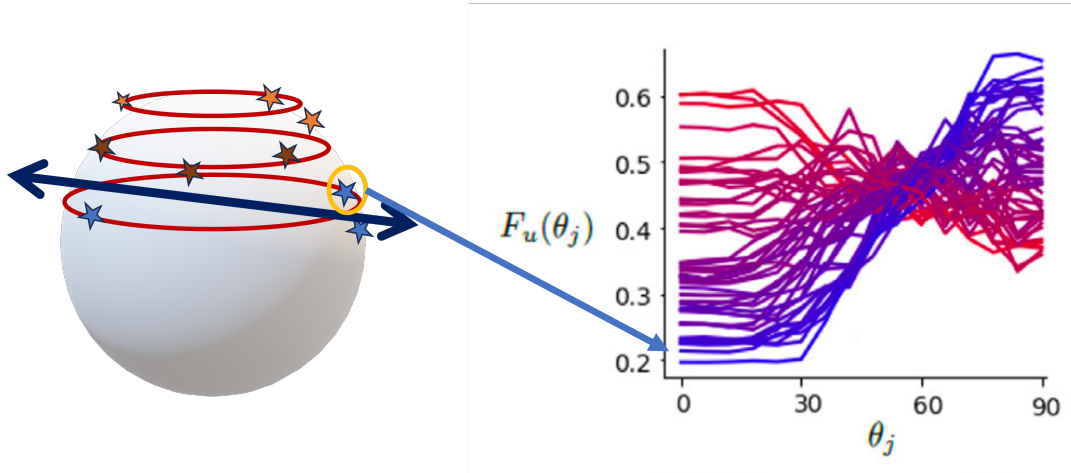


Figure 7.1: Zonal feature ($F_u(\theta_j)$) extraction from the Q-space using machine learner feature proposed by Karimi et al. [82]

parison. Our simulation results also demonstrated better neurite volume results with $b=1000 \text{ s}^2/\text{mm}$ in comparison with higher b-values, suggesting SNR plays a crucial role in NODDI fitting with rician log-likelihood function.

We observed that diffusion signal data with different b-values have different SNRs, indicating higher b-values might have reduced fitting quality when using multi-shell data.

7.3 Future Opportunities

7.3.1 Q-space Up-sampling without Optimized Diffusion Protocol

Our proposed approach in Chapter-4 could only up-sample diffusion signals for protocols with uniformly distributed directions (Optimized with IMOC Algorithm) whereas in most real clinical scenarios the diffusion directions are often un-optimized.

To resolve the issue, we have extended our work by incorporating zonal Q-space

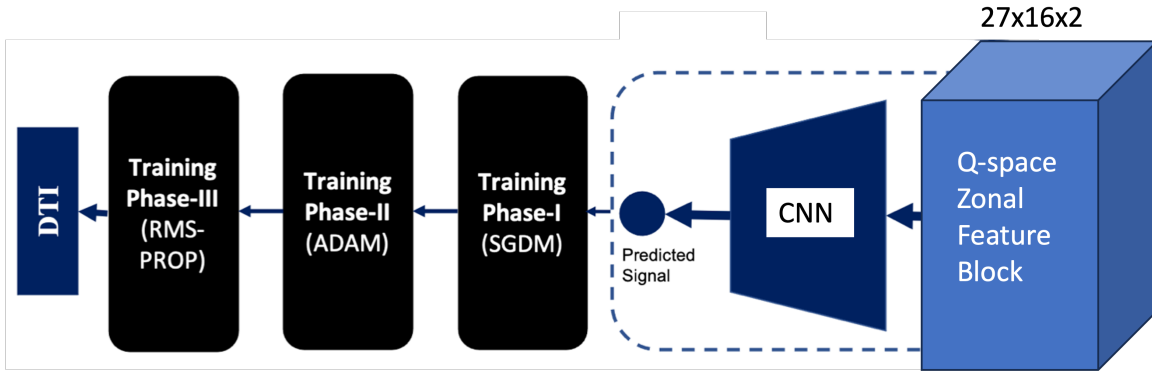


Figure 7.2: Zonal feature block with a 3D CNN trained with three phase optimization to upsample diffusion signal.

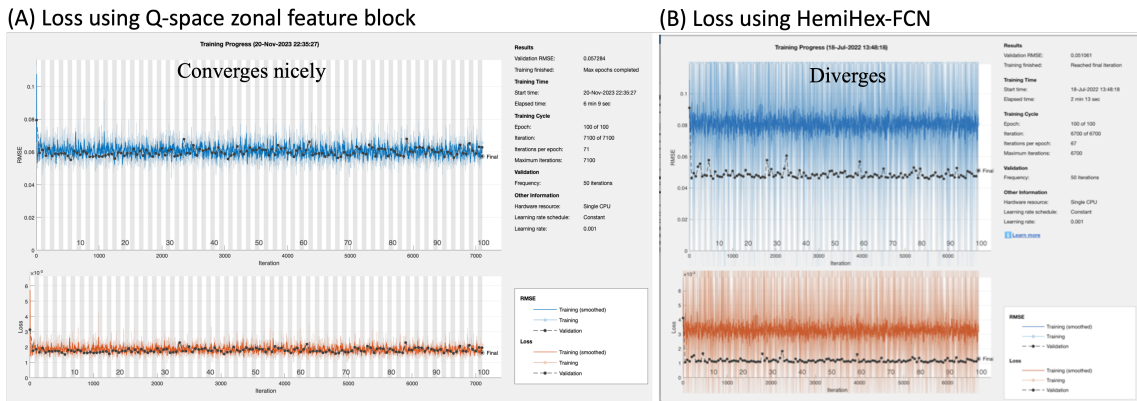


Figure 7.3: Loss comparison indicates performance using Q-space zonal feature block based network is better compared to HemiHex-FCN.

feature block in our learning strategy, implemented as a preliminary method that accounts for the non-uniform directions by utilizing intelligently catered Q-space features from the diffusion signals (Figure-7.1 and 7.2). The results we have obtained are promising when compared with HemiHex-MLP loss at the end of third phase optimization (Figure-7.3). Further experimentation is in progress to improve the up-sampling strategy for non-optimized cases.

7.3.2 Single-Shell NODDI in Clinical Longitudinal Study

We have successfully conducted an early stage investigation with proposed single-shell neurite information involving aging and cognitive status of HIV+ and Control subjects. In near future, we will be looking at 3 different time points that are 18 months apart for each subject, from the same data-set.

Further, microstructural investigation will be conducted on an earlier study, investigating the neurological implications of combined anti-retro-viral therapy (cART), that also includes longitudinal time-points. For this data-set, neurite quantification was not possible due to multi-shell requirement. We have scanned two volunteers using multi-shell for preliminary training and validation to reconstruct neurite measures from the available limiting single-shell data for the data-set. We expect to study progression of HIV pathogenesis in the brain as the virus is known to cross Blood Brain Barriers at the early stage of infection.

7.3.3 Multi-modal Sensitivity & AI in General MR

Multi-modality in MR comes with different sensitivities. Meaning they probe information regarding different tissue substrates. For example, myelin sensitivity with diffusion involves scanning with very low echo time and relatively low repetition time, which is not common for general diffusion protocols. This kind of physical limitations are very common in MR where different contrast brings out different tissue sensitivity or elements (e.g. Iron) residing in the tissue.

These contrasts can complement each other and depict further information on brain histology, ultimately influencing how to look at neural pathogenesis. AI is an indispensable tool in studying the relationship of these complementary sensitivities. In situations where physics is limited, data science can play a major role in advancing

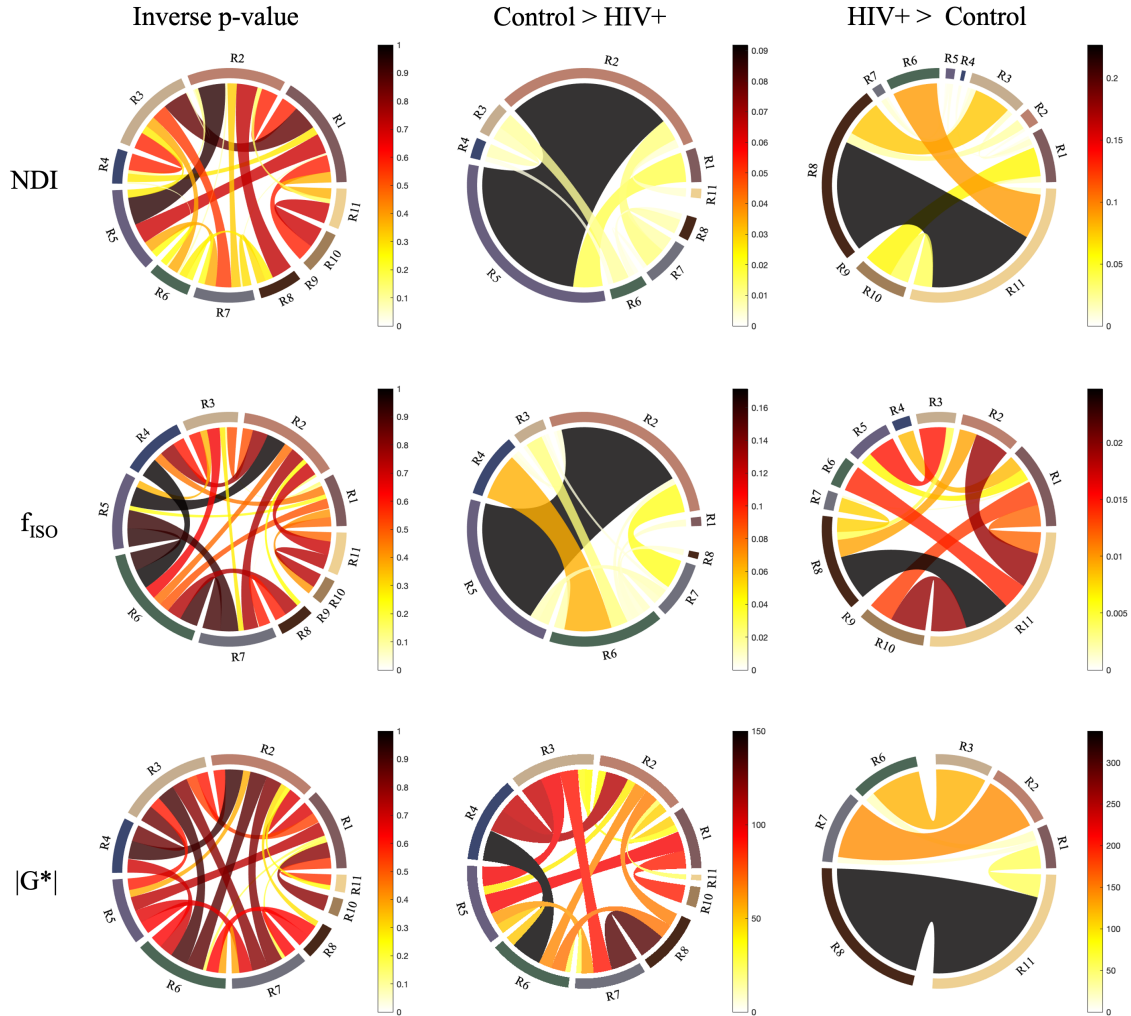


Figure 7.4: Example of multimodal MRI shows functional connectivity analysis of Visuo-Spatial Network using Diffusion and MR Elastography, where connectivity maps are generated from diffusion tractography. 34 control and 30 HIV subjects are used in the analysis.

such scenarios.

For example, we have previously reported that MR based stiffness can directly infer physical changes of brain tissue, and the free water content has shown to follow an inverse trend compared to stiffness in the HIV group [133]. Our recent analysis further explored HIV in Magnetic Resonance Elastography (MRE) functionally defined areas of the HIV brain by using diffusion based connectivity analysis. It is apparent that the change in neurite density and extracellular water affects the tissue stiffness in a functional brain network(Figure-7.4). Since MR Elastography requires a scanning setup not commonly available in clinical MRIs for the brain, diffusion derived metrics like NDI and f_{ISO} could potentially act as a surrogate if they can be mapped with viscosity and elastic modulus using AI models by using functionally defined regions and their connectivity. An elastography surrogate could be an important tool for brain tissue investigations.

7.3.4 Tackling Data Scarcity in Clinical dMRI

While accomplishing the two major objectives of Section-1.3.2, we have demonstrated that by leveraging sparse diffusion signal with their relative angular context, we can reduce the training sample burden significantly for clinical dMRI.

This finding is a pointer for future studies involving AI and dMRI. We expect that this will help in tackling future data scarcity problems in clinical dMRI.

Bibliography

- [1] T. Yousaf, G. Dervenoulas, and M. Politis, “Advances in MRI Methodology,” *International Review of Neurobiology*, vol. 141, pp. 31–76, 2018.
- [2] D. S. Novikov, V. G. Kiselev, and S. N. Jespersen, “On modeling,” *Magnetic Resonance in Medicine*, vol. 79, pp. 3172–3193, June 2018.
- [3] D. McClymont, I. Teh, and J. E. Schneider, “The impact of signal-to-noise ratio, diffusion-weighted directions and image resolution in cardiac diffusion tensor imaging – insights from the ex-vivo rat heart,” *Journal of Cardiovascular Magnetic Resonance*, vol. 19, p. 90, Nov. 2017.
- [4] A. Planchuelo-Gómez, S. Aja-Fernández, D. García-Azorín, A. Luis Guerrero, and R. Luis-García, “Fewer number of gradient directions in diffusion MRI can be counterbalanced with higher sample size: a migraine clinical study,” in *Proc. Intl. Soc. Mag. Reson. Med.* 28, 2020.
- [5] S. Aja-Fernández, C. Martín-Martín, . Planchuelo-Gómez, A. Faiyaz, M. N. Uddin, G. Schifitto, A. Tiwari, S. J. Shigwan, R. Kumar Singh, T. Zheng, Z. Cao, D. Wu, S. B. Blumberg, S. Sen, T. Goodwin-Allcock, P. J. Slator, M. Yigit Avci, Z. Li, B. Bilgic, Q. Tian, X. Wang, Z. Tang, M. Cabezas, A. Rauland, D. Merhof, R. Manzano Maria, V. P. Campos, T. Santini, M. A. da Costa Vieira, S. HashemizadehKolowri, E. DiBella, C. Peng, Z. Shen, Z. Chen, I. Ullah, M. Mani, H. Abdolmotalleby, S. Eckstrom, S. H. Baete, P. Filipiak, T. Dong, Q. Fan, R. de Luis-García, A. Tristán-Vega, and T. Pieciak, “Validation of deep learning techniques for quality augmentation in diffusion MRI for clinical studies,” *NeuroImage: Clinical*, vol. 39, p. 103483, Jan. 2023.
- [6] J. Zhang, S. Gregory, R. I. Scahill, A. Durr, D. L. Thomas, S. Lehericy, G. Rees, S. J. Tabrizi, H. Zhang, and TrackOn-HD investigators, “In vivo characterization of white matter pathology in premanifest huntington’s disease,” *Annals of Neurology*, vol. 84, pp. 497–504, Oct. 2018.
- [7] C. F. Slattery, J. Zhang, R. W. Paterson, A. J. M. Foulkes, A. Carton, K. Macpherson, L. Mancini, D. L. Thomas, M. Modat, N. Toussaint, D. M. Cash, J. S. Thornton, S. M. D. Henley, S. J. Crutch, D. C. Alexander,

- S. Ourselin, N. C. Fox, H. Zhang, and J. M. Schott, “ApoE influences regional white-matter axonal density loss in Alzheimer’s disease,” *Neurobiology of Aging*, vol. 57, pp. 8–17, Sept. 2017.
- [8] H. Zhang, T. Schneider, C. A. Wheeler-Kingshott, and D. C. Alexander, “NODDI: Practical in vivo neurite orientation dispersion and density imaging of the human brain,” *NeuroImage*, vol. 61, pp. 1000–1016, July 2012.
- [9] E. Gozdas, H. Fingerhut, L. Dacorso, J. L. Bruno, and S. M. H. Hosseini, “Neurite Imaging Reveals Widespread Alterations in Gray and White Matter Neurite Morphology in Healthy Aging and Amnestic Mild Cognitive Impairment,” *Cerebral Cortex (New York, N.Y.: 1991)*, vol. 31, pp. 5570–5578, Oct. 2021.
- [10] D. Wolpert and W. Macready, “No free lunch theorems for optimization,” *IEEE Transactions on Evolutionary Computation*, vol. 1, pp. 67–82, Apr. 1997. Conference Name: IEEE Transactions on Evolutionary Computation.
- [11] N. G. Gyori, M. Palombo, C. A. Clark, H. Zhang, and D. C. Alexander, “Training data distribution significantly impacts the estimation of tissue microstructure with machine learning,” *Magnetic Resonance in Medicine*, vol. 87, pp. 932–947, Feb. 2022.
- [12] A. Faiyaz, M. Doyley, G. Schifitto, J. Zhong, and M. N. Uddin, “Single-shell NODDI using dictionary-learner-estimated isotropic volume fraction,” *NMR in Biomedicine*, vol. 35, no. 2, p. e4628, 2022. _eprint: <https://onlinelibrary.wiley.com/doi/pdf/10.1002/nbm.4628>.
- [13] D. Le Bihan and H. Johansen-Berg, “Diffusion MRI at 25: exploring brain tissue structure and function,” *NeuroImage*, vol. 61, pp. 324–341, June 2012.
- [14] R. Brown, “XXVII. A brief account of microscopical observations made in the months of June, July and August 1827, on the particles contained in the pollen of plants; and on the general existence of active molecules in organic and inorganic bodies,” *The Philosophical Magazine*, vol. 4, pp. 161–173, Sept. 1828. Publisher: Taylor & Francis _eprint: <https://doi.org/10.1080/14786442808674769>.
- [15] G. Strijkers, M. Drost, and K. Nicolay, “Diffusion MRI: Theory, methods, and applications,” in *Diffusion imaging in muscle* (D. Jones, ed.), pp. 672–689, Oxford University Press, Jan. 2011.
- [16] E. A, “On the movement of small particles suspended in stationary liquids required by the molecular-kinetic theory of heat,” *Annalen Phys*, vol. 17, pp. 549–560, 1905.

- [17] W. S. Price, “Pulsed-field gradient nuclear magnetic resonance as a tool for studying translational diffusion: Part II. Experimental aspects,” *Concepts in Magnetic Resonance*, vol. 10, no. 4, pp. 197–237, 1998.
- [18] N. Nissan, E. Furman-Haran, M. Feinberg-Shapiro, D. Grobgeld, E. Eyal, T. Zelevinsky, and H. Degani, “Tracking the Mammary Architectural Features and Detecting Breast Cancer with Magnetic Resonance Diffusion Tensor Imaging,” *JoVE (Journal of Visualized Experiments)*, p. e52048, Dec. 2014.
- [19] I. O. Jelescu and M. D. Budde, “Design and Validation of Diffusion MRI Models of White Matter,” *Frontiers in Physics*, vol. 5, 2017.
- [20] M. Nel, “Phase encoding gradient mri | mri signal localisation | mri physics course #9,” 2023. YouTube, 38 minutes.
- [21] E. L. Hahn, “Spin Echoes,” *Physical Review*, vol. 80, pp. 580–594, Nov. 1950. Publisher: American Physical Society.
- [22] H. Y. Carr and E. M. Purcell, “Effects of Diffusion on Free Precession in Nuclear Magnetic Resonance Experiments,” *Physical Review*, vol. 94, pp. 630–638, May 1954. Publisher: American Physical Society.
- [23] H. C. Torrey, “Bloch Equations with Diffusion Terms,” *Physical Review*, vol. 104, pp. 563–565, Nov. 1956. Publisher: American Physical Society.
- [24] E. O. Stejskal and J. E. Tanner, “Spin Diffusion Measurements: Spin Echoes in the Presence of a Time-Dependent Field Gradient,” *The Journal of Chemical Physics*, vol. 42, pp. 288–292, Jan. 1965.
- [25] D. Le Bihan and E. Breton, “Imagerie de diffusion in-vivo par résonance magnétique nucléaire,” *Comptes-Rendus de l'Académie des Sciences*, vol. 93, pp. 27–34, Dec. 1985.
- [26] D. Le Bihan, E. Breton, D. Lallemand, P. Grenier, E. Cabanis, and M. Laval-Jeantet, “MR imaging of intravoxel incoherent motions: application to diffusion and perfusion in neurologic disorders,” *Radiology*, vol. 161, pp. 401–407, Nov. 1986.
- [27] P. T. Callaghan, “Physics of Diffusion,” in *Diffusion MRI: Theory, Methods, and Applications* (P. Jones, Derek K., ed.), p. 0, Oxford University Press, Nov. 2010.
- [28] T. Niendorf, R. M. Dijkhuizen, D. G. Norris, M. van Lookeren Campagne, and K. Nicolay, “Biexponential diffusion attenuation in various states of brain tissue: Implications for diffusion-weighted imaging,” *Magnetic Resonance in Medicine*, vol. 36, no. 6, pp. 847–857, 1996. _eprint: <https://onlinelibrary.wiley.com/doi/pdf/10.1002/mrm.1910360607>.

- [29] J. Cheng, D. Shen, P.-T. Yap, and P. J. Basser, "Single- and Multiple-Shell Uniform Sampling Schemes for Diffusion MRI Using Spherical Codes," *IEEE transactions on medical imaging*, vol. 37, pp. 185–199, Jan. 2018.
- [30] B. Lampinen, F. Szczepankiewicz, J. Lätt, L. Knutsson, J. Mårtensson, I. M. Björkman-Burtscher, D. van Westen, P. C. Sundgren, F. Ståhlberg, and M. Nilsson, "Probing brain tissue microstructure with MRI: principles, challenges, and the role of multidimensional diffusion-relaxation encoding," *NeuroImage*, vol. 282, p. 120338, Nov. 2023.
- [31] F. Aboitiz, A. B. Scheibel, R. S. Fisher, and E. Zaidel, "Fiber composition of the human corpus callosum," *Brain Research*, vol. 598, pp. 143–153, Dec. 1992.
- [32] J. M. Edgar, M. McLaughlin, H. B. Werner, M. C. McCulloch, J. A. Barrie, A. Brown, A. B. Faichney, N. Snaidero, K.-A. Nave, and I. R. Griffiths, "Early ultrastructural defects of axons and axon-glia junctions in mice lacking expression of Cnp1," *Glia*, vol. 57, pp. 1815–1824, Dec. 2009.
- [33] C. Hildebrand, S. Remahl, H. Persson, and C. Bjartmar, "Myelinated nerve fibres in the CNS," *Progress in Neurobiology*, vol. 40, pp. 319–384, Mar. 1993.
- [34] B. D. Trapp and G. J. Kidd, "Chapter 1 - Structure of the Myelinated Axon," in *Myelin Biology and Disorders* (R. A. Lazzarini, J. W. Griffin, H. Lassman, K.-A. Nave, R. Miller, and B. D. Trapp, eds.), pp. 3–27, San Diego: Academic Press, Jan. 2004.
- [35] J. A. Perge, K. Koch, R. Miller, P. Sterling, and V. Balasubramanian, "How the Optic Nerve Allocates Space, Energy Capacity, and Information," *Journal of Neuroscience*, vol. 29, pp. 7917–7928, June 2009. Publisher: Society for Neuroscience Section: Articles.
- [36] G. Xu, E. Takahashi, R. D. Folkerth, R. L. Haynes, J. J. Volpe, P. E. Grant, and H. C. Kinney, "Radial Coherence of Diffusion Tractography in the Cerebral White Matter of the Human Fetus: Neuroanatomic Insights," *Cerebral Cortex*, vol. 24, pp. 579–592, Mar. 2014.
- [37] N. Stikov, J. S. W. Campbell, T. Stroh, M. Lavelée, S. Frey, J. Novek, S. Nuara, M.-K. Ho, B. J. Bedell, R. F. Dougherty, I. R. Leppert, M. Boudreau, S. Narayanan, T. Duval, J. Cohen-Adad, P.-A. Picard, A. Gasecka, D. Côté, and G. B. Pike, "In vivo histology of the myelin g-ratio with magnetic resonance imaging," *NeuroImage*, vol. 118, pp. 397–405, Sept. 2015.
- [38] I. O. Jelescu, J. Veraart, E. Fieremans, and D. S. Novikov, "Degeneracy in model parameter estimation for multi-compartmental diffusion in neuronal tissue," *NMR in Biomedicine*, vol. 29, no. 1, pp. 33–47, 2016. _eprint: <https://onlinelibrary.wiley.com/doi/pdf/10.1002/nbm.3450>.

- [39] J. Spacek and M. Hartmann, “Three-dimensional analysis of dendritic spines. I. Quantitative observations related to dendritic spine and synaptic morphology in cerebral and cerebellar cortices,” *Anatomy and Embryology*, vol. 167, no. 2, pp. 289–310, 1983.
- [40] M. R. Bennett, L. Farnell, and W. G. Gibson, “Fiber Pathway Pathology, Synapse Loss and Decline of Cortical Function in Schizophrenia,” *PLOS ONE*, vol. 8, p. e60518, Apr. 2013. Publisher: Public Library of Science.
- [41] M. V. Sofroniew and H. V. Vinters, “Astrocytes: biology and pathology,” *Acta Neuropathologica*, vol. 119, pp. 7–35, Jan. 2010.
- [42] D. C. Alexander, P. L. Hubbard, M. G. Hall, E. A. Moore, M. Ptito, G. J. Parker, and T. B. Dyrby, “Orientationally invariant indices of axon diameter and density from diffusion MRI,” *Neuroimage*, vol. 52, no. 4, pp. 1374–1389, 2010. Type: Journal Article.
- [43] A. Schüz and G. Palm, “Density of neurons and synapses in the cerebral cortex of the mouse,” *Journal of Comparative Neurology*, vol. 286, no. 4, pp. 442–455, 1989. _eprint: <https://onlinelibrary.wiley.com/doi/pdf/10.1002/cne.902860404>.
- [44] A. Abbott, “Crumb of mouse brain reconstructed in full detail,” *Nature*, vol. 524, pp. 17–17, Aug. 2015. Number: 7563 Publisher: Nature Publishing Group.
- [45] N. Kasthuri, K. J. Hayworth, D. R. Berger, R. L. Schalek, J. A. Conchello, S. Knowles-Barley, D. Lee, A. Vázquez-Reina, V. Kaynig, T. R. Jones, M. Roberts, J. L. Morgan, J. C. Tapia, H. S. Seung, W. G. Roncal, J. T. Vogelstein, R. Burns, D. L. Sussman, C. E. Priebe, H. Pfister, and J. W. Lichtman, “Saturated Reconstruction of a Volume of Neocortex,” *Cell*, vol. 162, pp. 648–661, July 2015.
- [46] M. Palombo, A. Ianus, M. Guerreri, D. Nunes, D. C. Alexander, N. Shemesh, and H. Zhang, “SANDI: A compartment-based model for non-invasive apparent soma and neurite imaging by diffusion MRI,” *NeuroImage*, vol. 215, p. 116835, July 2020.
- [47] K. L. LEENDERS, D. PERANI, A. A. LAMMERTSMA, J. D. HEATHER, P. BUCKINGHAM, T. JONES, M. J. R. HEALY, J. M. GIBBS, R. J. S. WISE, J. HATAZAWA, S. HEROLD, R. P. BEANEY, D. J. BROOKS, T. SPINKS, C. RHODES, and R. S. J. FRACKOWIAK, “CEREBRAL BLOOD FLOW, BLOOD VOLUME AND OXYGEN UTILIZATION: NORMAL VALUES AND EFFECT OF AGE,” *Brain*, vol. 113, pp. 27–47, Feb. 1990.

- [48] S. N. Jespersen, J. L. Olesen, B. Hansen, and N. Shemesh, “Diffusion time dependence of microstructural parameters in fixed spinal cord,” *NeuroImage*, vol. 182, pp. 329–342, Nov. 2018.
- [49] H. Zhang, P. L. Hubbard, G. J. Parker, and D. C. Alexander, “Axon diameter mapping in the presence of orientation dispersion with diffusion MRI,” *Neuroimage*, vol. 56, no. 3, pp. 1301–1315, 2011. Type: Journal Article.
- [50] B. Kumaraswamy, “6 - Neural networks for data classification,” in *Artificial Intelligence in Data Mining* (D. Binu and B. R. Rajakumar, eds.), pp. 109–131, Academic Press, Jan. 2021.
- [51] A. Daducci, E. J. Canales-Rodríguez, H. Zhang, T. B. Dyrby, D. C. Alexander, and J.-P. Thiran, “Accelerated Microstructure Imaging via Convex Optimization (AMICO) from diffusion MRI data,” *NeuroImage*, vol. 105, pp. 32–44, Jan. 2015.
- [52] X. Liu, W. Xu, and X. Ye, “The Ill-Posed Problem and Regularization in Parallel Magnetic Resonance Imaging,” in *2009 3rd International Conference on Bioinformatics and Biomedical Engineering*, pp. 1–4, June 2009. ISSN: 2151-7622.
- [53] S. Bhadra, V. A. Kelkar, F. J. Brooks, and M. A. Anastasio, “On Hallucinations in Tomographic Image Reconstruction,” *IEEE Transactions on Medical Imaging*, vol. 40, pp. 3249–3260, Nov. 2021.
- [54] G. Ting, F. Grussu, Claudia Gandini Wheeler-Kingshott, Daniel Alexander, and Hui Zhang, “Deep-learning-informed parameter estimation improves reliability of spinal cord diffusion MRI,” in *Proc. Intl. Soc. Mag. Reson. Med. 30*, (UK), May 2022.
- [55] M. Tariq, T. Schneider, D. C. Alexander, C. A. Gandini Wheeler-Kingshott, and H. Zhang, “Bingham–NODDI: Mapping anisotropic orientation dispersion of neurites using diffusion MRI,” *NeuroImage*, vol. 133, pp. 207–223, June 2016.
- [56] K. Kamiya, M. Hori, and S. Aoki, “NODDI in clinical research,” *Journal of Neuroscience Methods*, vol. 346, p. 108908, Dec. 2020.
- [57] C. Davatzikos, “Machine learning in neuroimaging: Progress and challenges,” *NeuroImage*, vol. 197, pp. 652–656, Aug. 2019.
- [58] V. Antun, F. Renna, C. Poon, B. Adcock, and A. C. Hansen, “On instabilities of deep learning in image reconstruction and the potential costs of AI,” *Proceedings of the National Academy of Sciences of the United States of America*, vol. 117, pp. 30088–30095, Dec. 2020.

- [59] V. A. Kelkar, S. Bhadra, and M. A. Anastasio, “Compressible Latent-Space Invertible Networks for Generative Model-Constrained Image Reconstruction,” *IEEE Transactions on Computational Imaging*, vol. 7, pp. 209–223, 2021. Conference Name: IEEE Transactions on Computational Imaging.
- [60] O. Pasternak, N. Sochen, Y. Gur, N. Intrator, and Y. Assaf, “Free water elimination and mapping from diffusion MRI,” *Magnetic Resonance in Medicine*, vol. 62, no. 3, pp. 717–730, 2009. _eprint: <https://onlinelibrary.wiley.com/doi/pdf/10.1002/mrm.22055>.
- [61] T. Zheng, W. Zheng, Y. Sun, Y. Zhang, C. Ye, and D. Wu, “An Adaptive Network with Extragradient for Diffusion MRI-Based Microstructure Estimation,” in *Medical Image Computing and Computer Assisted Intervention – MICCAI 2022* (L. Wang, Q. Dou, P. T. Fletcher, S. Speidel, and S. Li, eds.), Lecture Notes in Computer Science, (Cham), pp. 153–162, Springer Nature Switzerland, 2022.
- [62] T. Zheng, C. Sun, W. Zheng, W. Shi, H. Li, Y. Sun, Y. Zhang, G. Wang, C. Ye, and D. Wu, “A microstructure estimation Transformer inspired by sparse representation for diffusion MRI,” May 2022. arXiv:2205.06450 [cs, eess].
- [63] L. Ning, C.-F. Westin, and Y. Rathi, “Estimating diffusion propagator and its moments using directional radial basis functions,” *IEEE transactions on medical imaging*, vol. 34, pp. 2058–2078, Oct. 2015.
- [64] Q. Tian, Z. Li, Q. Fan, J. R. Polimeni, B. Bilgic, D. H. Salat, and S. Y. Huang, “SDnDTI: Self-supervised deep learning-based denoising for diffusion tensor MRI,” *NeuroImage*, vol. 253, p. 119033, June 2022.
- [65] E. Kaden, F. Kruggel, and D. C. Alexander, “Quantitative mapping of the per-axon diffusion coefficients in brain white matter,” *Magnetic Resonance in Medicine*, vol. 75, no. 4, pp. 1752–1763, 2016. _eprint: <https://onlinelibrary.wiley.com/doi/pdf/10.1002/mrm.25734>.
- [66] E. Kaden, N. D. Kelm, R. P. Carson, M. D. Does, and D. C. Alexander, “Multi-compartment microscopic diffusion imaging,” *NeuroImage*, vol. 139, pp. 346–359, Oct. 2016.
- [67] D. Karimi and A. Gholipour, “Atlas-powered deep learning (ADL) – application to diffusion weighted MRI,” May 2022. arXiv:2205.03210 [physics].
- [68] D. Karimi and A. Gholipour, “Diffusion tensor estimation with transformer neural networks,” *Artificial Intelligence in Medicine*, vol. 130, p. 102330, Aug. 2022.

- [69] R. R. Jha, S. K. Pathak, V. Nath, W. Schneider, B. V. R. Kumar, A. Bhavsar, and A. Nigam, “VRfRNet: Volumetric ROI fODF reconstruction network for estimation of multi-tissue constrained spherical deconvolution with only single shell dMRI,” *Magnetic Resonance Imaging*, vol. 90, pp. 1–16, July 2022.
- [70] W. Ma and L. Peng, “Image Quality Transfer with Auto-Encoding Applied to dMRI Super-Resolution,” in *2021 4th International Conference on Advanced Electronic Materials, Computers and Software Engineering (AEMCSE)*, pp. 828–831, Mar. 2021.
- [71] Y. Diao and I. Jelescu, “Parameter estimation for WMTI-Watson model of white matter using encoder-decoder recurrent neural network,” *Magnetic Resonance in Medicine*, vol. 89, no. 3, pp. 1193–1206, 2023. eprint: <https://onlinelibrary.wiley.com/doi/pdf/10.1002/mrm.29495>.
- [72] Q. Tian, Z. Li, Q. Fan, C. Ngamsombat, Y. Hu, C. Liao, F. Wang, K. Setsompop, J. R. Polimeni, B. Bilgic, and S. Y. Huang, “SRDTI: Deep learning-based super-resolution for diffusion tensor MRI,” Feb. 2021. arXiv:2102.09069 [physics].
- [73] J. Du, S. Zhang, G. Wu, J. M. F. Moura, and S. Kar, “Topology Adaptive Graph Convolutional Networks,” Feb. 2018. arXiv:1710.10370 [cs, stat].
- [74] G. Chen, H. Jiang, J. Liu, J. Ma, H. Cui, Y. Xia, and P.-T. Yap, “Hybrid Graph Transformer for Tissue Microstructure Estimation with Undersampled Diffusion MRI Data,” in *Medical Image Computing and Computer Assisted Intervention – MICCAI 2022* (L. Wang, Q. Dou, P. T. Fletcher, S. Speidel, and S. Li, eds.), Lecture Notes in Computer Science, (Cham), pp. 113–122, Springer Nature Switzerland, 2022.
- [75] Y. Qin, Y. Li, Z. Zhuo, Z. Liu, Y. Liu, and C. Ye, “Multimodal super-resolved q-space deep learning,” *Medical Image Analysis*, vol. 71, p. 102085, July 2021.
- [76] A. Faiyaz, M. N. Uddin, and G. Schifitto, “Angular upsampling in diffusion MRI using contextual HemiHex sub-sampling in q-space,” Oct. 2022. arXiv:2211.00240 [cs, eess].
- [77] Y. Qin, Z. Liu, C. Liu, Y. Li, X. Zeng, and C. Ye, “Super-Resolved q-Space deep learning with uncertainty quantification,” *Medical Image Analysis*, vol. 67, p. 101885, Jan. 2021.
- [78] S. Sedlar, A. Alimi, T. Papadopoulo, R. Deriche, and S. Deslauriers-Gauthier, “A spherical convolutional neural network for white matter structure imaging via dMRI,” in *MICCAI 2021 - 24th International Conference on Medical Image Computing and Computer Assisted Intervention* (M. d. Bruijne, P. C. Cattin,

- S. Cotin, N. Padoy, S. Speidel, Y. Zheng, and C. Essert, eds.), vol. volume 12903 of *24th Medical Image Computing and Computer Assisted Intervention - MICCAI 2021, Part III*, (Strasbourg / Virtual, France), pp. Pages 529–539, Sept. 2021.
- [79] V. Nath, K. Ramadass, K. G. Schilling, C. B. Hansen, R. Fick, S. K. Pathak, A. W. Anderson, and B. A. Landman, “DW-MRI Microstructure Model of Models Captured Via Single-Shell Bottleneck Deep Learning,” in *Computational Diffusion MRI* (N. Gyori, J. Hutter, V. Nath, M. Palombo, M. Pizzolato, and F. Zhang, eds.), Mathematics and Visualization, (Cham), pp. 147–157, Springer International Publishing, 2021.
- [80] S. Lee, S. Purushwalkam, M. Cogswell, D. Crandall, and D. Batra, “Why M Heads are Better than One: Training a Diverse Ensemble of Deep Networks,” Nov. 2015. arXiv:1511.06314 [cs].
- [81] D. Karimi, C. Jaimes, F. Machado-Rivas, L. Vasung, S. Khan, S. K. Warfield, and A. Gholipour, “Deep learning-based parameter estimation in fetal diffusion-weighted MRI,” *NeuroImage*, vol. 243, p. 118482, Nov. 2021.
- [82] D. Karimi, L. Vasung, C. Jaimes, F. Machado-Rivas, S. Khan, S. K. Warfield, and A. Gholipour, “A machine learning-based method for estimating the number and orientations of major fascicles in diffusion-weighted magnetic resonance imaging,” *Medical Image Analysis*, vol. 72, p. 102129, Aug. 2021.
- [83] Q. Tian, B. Bilgic, Q. Fan, C. Liao, C. Ngamsombat, Y. Hu, T. Witzel, K. Setsompop, J. R. Polimeni, and S. Y. Huang, “DeepDTI: High-fidelity six-direction diffusion tensor imaging using deep learning,” *NeuroImage*, vol. 219, p. 117017, Oct. 2020.
- [84] M. Ren, H. Kim, N. Dey, and G. Gerig, “Q-space Conditioned Translation Networks for Directional Synthesis of Diffusion Weighted Images from Multi-modal Structural MRI,” in *Medical Image Computing and Computer Assisted Intervention – MICCAI 2021* (M. de Bruijne, P. C. Cattin, S. Cotin, N. Padoy, S. Speidel, Y. Zheng, and C. Essert, eds.), Lecture Notes in Computer Science, (Cham), pp. 530–540, Springer International Publishing, 2021.
- [85] S. Koppers, L. Bloy, J. I. Berman, C. M. W. Tax, J. C. Edgar, and D. Merhof, “Spherical Harmonic Residual Network for Diffusion Signal Harmonization,” pp. 173–182, 2019. Book Title: Computational Diffusion MRI ISBN: 9783030058302 9783030058319 Place: Cham Publisher: Springer International Publishing.
- [86] G. Chen, Y. Hong, Y. Zhang, J. Kim, K. M. Huynh, J. Ma, W. Lin, D. Shen, and P.-T. Yap, “Estimating Tissue Microstructure with Undersampled Diffusion

- Data via Graph Convolutional Neural Networks,” in *Medical Image Computing and Computer Assisted Intervention – MICCAI 2020* (A. L. Martel, P. Abolmaesumi, D. Stoyanov, D. Mateus, M. A. Zuluaga, S. K. Zhou, D. Racoceanu, and L. Joskowicz, eds.), Lecture Notes in Computer Science, (Cham), pp. 280–290, Springer International Publishing, 2020.
- [87] C. Ye, X. Li, and J. Chen, “A deep network for tissue microstructure estimation using modified LSTM units,” *Medical Image Analysis*, vol. 55, pp. 49–64, July 2019.
- [88] Z. Lin, T. Gong, K. Wang, Z. Li, H. He, Q. Tong, F. Yu, and J. Zhong, “Fast learning of fiber orientation distribution function for MR tractography using convolutional neural network,” *Medical Physics*, vol. 46, no. 7, pp. 3101–3116, 2019. _eprint: <https://onlinelibrary.wiley.com/doi/pdf/10.1002/mp.13555>.
- [89] E. K. Gibbons, K. K. Hodgson, A. S. Chaudhari, L. G. Richards, J. J. Majersik, G. Adluru, and E. V. DiBella, “Simultaneous NODDI and GFA parameter map generation from subsampled q-space imaging using deep learning,” *Magnetic Resonance in Medicine*, vol. 81, no. 4, pp. 2399–2411, 2019. _eprint: <https://onlinelibrary.wiley.com/doi/pdf/10.1002/mrm.27568>.
- [90] S. B. Blumberg, R. Tanno, I. Kokkinos, and D. C. Alexander, “Deeper Image Quality Transfer: Training Low-Memory Neural Networks for 3D Images,” in *Medical Image Computing and Computer Assisted Intervention – MICCAI 2018* (A. F. Frangi, J. A. Schnabel, C. Davatzikos, C. Alberola-López, and G. Fichtinger, eds.), Lecture Notes in Computer Science, (Cham), pp. 118–125, Springer International Publishing, 2018.
- [91] C. Ye, “Estimation of tissue microstructure using a deep network inspired by a sparse reconstruction framework,” in *International Conference on Information Processing in Medical Imaging*, pp. 466–477, Springer, 2017. Type: Conference Proceedings.
- [92] A. Faiyaz, M. Doyley, G. Schifitto, J. Zhong, and M. N. Uddin, “Single-Shell NODDI Using Dictionary Learner Estimated Isotropic Volume Fraction,” Apr. 2021. arXiv:2102.02772 [physics].
- [93] D. C. Alexander, D. Zikic, A. Ghosh, R. Tanno, V. Wottschel, J. Zhang, E. Kaden, T. B. Dyrby, S. N. Sotiroopoulos, H. Zhang, and A. Criminisi, “Image quality transfer and applications in diffusion MRI,” *NeuroImage*, vol. 152, pp. 283–298, May 2017.
- [94] G. L. Nedjati-Gilani, T. Schneider, M. G. Hall, N. Cawley, I. Hill, O. Ciccarelli, I. Drobnjak, C. A. M. G. Wheeler-Kingshott, and D. C. Alexander, “Machine

- learning based compartment models with permeability for white matter microstructure imaging,” *NeuroImage*, vol. 150, pp. 119–135, Apr. 2017.
- [95] E. R. Sabidussi, S. Klein, B. Jeurissen, and D. H. J. Poot, “dtiRIM: A generalisable deep learning method for Diffusion Tensor Imaging,” *NeuroImage*, p. 119900, Jan. 2023.
- [96] V. Golkov, A. Dosovitskiy, J. I. Sperl, M. I. Menzel, M. Czisch, P. Sämann, T. Brox, and D. Cremers, “q-Space Deep Learning: Twelve-Fold Shorter and Model-Free Diffusion MRI Scans,” *IEEE Transactions on Medical Imaging*, vol. 35, pp. 1344–1351, May 2016. Conference Name: IEEE Transactions on Medical Imaging.
- [97] D. E. Rumelhart, J. L. McClelland, and P. R. Group, *Parallel Distributed Processing, Volume 1: Explorations in the Microstructure of Cognition: Foundations*. The MIT Press, July 1986.
- [98] S. Hochreiter and J. Schmidhuber, “Long Short-Term Memory,” *Neural Computation*, vol. 9, pp. 1735–1780, Nov. 1997.
- [99] I. Goodfellow, J. Pouget-Abadie, M. Mirza, B. Xu, D. Warde-Farley, S. Ozair, A. Courville, and Y. Bengio, “Generative Adversarial Nets,” in *Advances in Neural Information Processing Systems*, vol. 27, Curran Associates, Inc., 2014.
- [100] A. Vaswani, N. Shazeer, N. Parmar, J. Uszkoreit, L. Jones, A. N. Gomez, . Kaiser, and I. Polosukhin, “Attention is All you Need,” in *Advances in Neural Information Processing Systems*, vol. 30, Curran Associates, Inc., 2017.
- [101] MICCAI, “MICCAI Challenge: Quality augmentation in diffusion mri for clinical studies: Validation in migraine, Retrieved from QUAD22 website <https://www.lpi.tel.uva.es/quad22/>,” 2022.
- [102] T. J. Simon, L. Ding, J. P. Bish, D. M. McDonald-McGinn, E. H. Zackai, and J. Gee, “Volumetric, connective, and morphologic changes in the brains of children with chromosome 22q11.2 deletion syndrome: an integrative study,” *NeuroImage*, vol. 25, pp. 169–180, Mar. 2005.
- [103] A. Finkelstein, A. Faiyaz, M. T. Weber, X. Qiu, M. N. Uddin, J. Zhong, and G. Schifitto, “Fixel-Based Analysis and Free Water Corrected DTI Evaluation of HIV-Associated Neurocognitive Disorders,” *Frontiers in Neurology*, vol. 12, 2021.
- [104] P. Basser, “Relationships between diffusion tensor and q-space MRI,” *Magnetic Resonance in Medicine*, vol. 47, no. 2, pp. 392–397, 2002.

- [105] C. F. Westin, S. E. Maier, H. Mamata, A. Nabavi, F. A. Jolesz, and R. Kikinis, “Processing and visualization for diffusion tensor MRI,” *Medical Image Analysis*, vol. 6, pp. 93–108, June 2002.
- [106] H. K. Aggarwal, M. P. Mani, and M. Jacob, “MoDL-MUSSELS: Model-Based Deep Learning for Multi-Shot Sensitivity Encoded Diffusion MRI,” *IEEE Transactions on Medical Imaging*, vol. 39, pp. 1268–1277, Apr. 2020. arXiv:1812.08115 [cs].
- [107] Y. Qiao, Y. Chen, L. Li, J. Chen, W. Emori, X. Wang, L. Yang, H. Zhou, G. Song, N. Naik, Z. Wang, and Z. Guo, “Corrosion Behavior of a Nickel-Free High-Nitrogen Stainless Steel with Hydrogen Charging,” *JOM*, vol. 73, pp. 1165–1172, Apr. 2021.
- [108] A. Ahmad, D. Parker, S. Dheer, Z. R. Samani, and R. Verma, “3D-QCNet – A pipeline for automated artifact detection in diffusion MRI images,” *Computerized Medical Imaging and Graphics*, vol. 103, p. 102151, Jan. 2023.
- [109] S. Fadnavis, J. Batson, and E. Garyfallidis, “Patch2Self: Denoising Diffusion MRI with Self-Supervised Learning,” in *Advances in Neural Information Processing Systems*, vol. 33, pp. 16293–16303, Curran Associates, Inc., 2020.
- [110] G. Chen, B. Dong, Y. Zhang, W. Lin, D. Shen, and P.-T. Yap, “Angular Upsampling in Infant Diffusion MRI Using Neighborhood Matching in x-q Space,” *Frontiers in Neuroinformatics*, vol. 12, p. 57, Sept. 2018.
- [111] I. B. Alaya, M. Jribi, F. Ghorbel, M. Mars, and T. Kraiem, “Quantitative evaluation of fiber tractography with a Delaunay triangulation-based interpolation approach,” *Medical & Biological Engineering & Computing*, vol. 57, pp. 925–938, Apr. 2019.
- [112] I. Ben Alaya, M. Jribi, F. Ghorbel, D. Sappey-Marinier, and T. Kraiem, “Fast and Accurate Estimation of the HARDI Signal in Diffusion MRI Using a Nearest-Neighbor Interpolation Approach,” *IRBM*, vol. 38, pp. 156–166, June 2017.
- [113] I. Ben Alaya, M. Jribi, F. Ghorbel, and T. Kraiem, “Comparison analysis of local angular interpolation methods in diffusion MRI,” *Computer Methods in Biomechanics and Biomedical Engineering: Imaging & Visualization*, vol. 10, pp. 687–696, Nov. 2022. Publisher: Taylor & Francis _eprint: <https://doi.org/10.1080/21681163.2021.2024089>.
- [114] A. Planchuelo-Gómez, D. García-Azorín, . L. Guerrero, S. Aja-Fernández, M. Rodríguez, and R. De Luis-García, “Structural connectivity alterations in chronic and episodic migraine: A diffusion magnetic resonance imaging connectomics study,” *Cephalalgia*, vol. 40, pp. 367–383, Apr. 2020.

- [115] J. Cheng, D. Shen, and P.-T. Yap, “Designing Single- and Multiple-Shell Sampling Schemes for Diffusion MRI Using Spherical Code,” *Medical image computing and computer-assisted intervention : MICCAI ... International Conference on Medical Image Computing and Computer-Assisted Intervention*, vol. 17, no. Pt 3, pp. 281–288, 2014.
- [116] J. Cheng, D. Shen, P.-T. Yap, and P. J. Basser, “Single- and Multiple-Shell Uniform Sampling Schemes for Diffusion MRI Using Spherical Codes,” *IEEE transactions on medical imaging*, vol. 37, pp. 185–199, Jan. 2018.
- [117] J. Andersson, S. Smith, and M. Jenkinson, “FNIRT-FMRIB’s non-linear image registration tool,” *14th Annual Meeting of the Organization for Human Brain Mapping*, Jan. 2008.
- [118] S. Mori, S. Wakana, P. C. M. v. Zijl, and L. M. Nagae-Poetscher, *MRI Atlas of Human White Matter*. Elsevier, May 2005. Google-Books-ID: ltwRYlvFNLIC.
- [119] T. E. Nichols and A. P. Holmes, “Nonparametric permutation tests for functional neuroimaging: a primer with examples,” *Human Brain Mapping*, vol. 15, pp. 1–25, Jan. 2002.
- [120] S. M. Smith and T. E. Nichols, “Threshold-free cluster enhancement: addressing problems of smoothing, threshold dependence and localisation in cluster inference,” *NeuroImage*, vol. 44, pp. 83–98, Jan. 2009.
- [121] M. F. Glasser, S. N. Sotiroopoulos, J. A. Wilson, T. S. Coalson, B. Fischl, J. L. Andersson, J. Xu, S. Jbabdi, M. Webster, and J. R. Polimeni, “The minimal preprocessing pipelines for the Human Connectome Project,” *Neuroimage*, vol. 80, pp. 105–124, 2013. Type: Journal Article.
- [122] C. Ye, “Tissue microstructure estimation using a deep network inspired by a dictionary-based framework,” *Medical Image Analysis*, vol. 42, pp. 288–299, Dec. 2017.
- [123] T. Blumensath and M. E. Davies, “Iterative Thresholding for Sparse Approximations,” *Journal of Fourier Analysis and Applications*, vol. 14, no. 5, pp. 629–654, 2008. Type: Journal Article.
- [124] L. Svennerholm, K. Boström, B. Jungbjer, and L. Olsson, “Membrane lipids of adult human brain: lipid composition of frontal and temporal lobe in subjects of age 20 to 100 years,” *Journal of Neurochemistry*, vol. 63, pp. 1802–1811, Nov. 1994.
- [125] A. Giorgio, L. Santelli, V. Tomassini, R. Bosnell, S. Smith, N. De Stefano, and H. Johansen-Berg, “Age-related changes in grey and white matter structure throughout adulthood,” *NeuroImage*, vol. 51, pp. 943–951, July 2010.

- [126] Y. Statsenko, T. Habuza, D. Smetanina, G. L. Simiyu, L. Uzianbaeva, K. Neidl-Van Gorkom, N. Zaki, I. Charykova, J. Al Koteesh, T. M. Almansoori, M. Belghali, and M. Ljubisavljevic, “Brain Morphometry and Cognitive Performance in Normal Brain Aging: Age- and Sex-Related Structural and Functional Changes,” *Frontiers in Aging Neuroscience*, vol. 13, 2022.
- [127] J. Veraart, E. Fieremans, and D. S. Novikov, “On the scaling behavior of water diffusion in human brain white matter,” *NeuroImage*, vol. 185, pp. 379–387, 2019. Type: Journal Article.
- [128] F. Fazekas, J. B. Chawluk, A. Alavi, H. I. Hurtig, and R. A. Zimmerman, “MR signal abnormalities at 1.5 T in Alzheimer’s dementia and normal aging,” *American journal of roentgenology*, vol. 149, no. 2, pp. 351–356, 1987. Type: Journal Article.
- [129] M. Golub, R. Neto Henriques, and R. Gouveia Nunes, “Free-water DTI estimates from single b-value data might seem plausible but must be interpreted with care,” *Magnetic Resonance in Medicine*, vol. 85, no. 5, pp. 2537–2551, 2021. Type: Journal Article.
- [130] F. Sepehrband, K. A. Clark, J. F. Ullmann, N. D. Kurniawan, G. Leanage, D. C. Reutens, and Z. Yang, “Brain tissue compartment density estimated using diffusion-weighted MRI yields tissue parameters consistent with histology,” *Human brain mapping*, vol. 36, no. 9, pp. 3687–3702, 2015. Type: Journal Article.
- [131] H. Fukutomi, M. F. Glasser, K. Murata, T. Akasaka, K. Fujimoto, T. Yamamoto, J. A. Autio, T. Okada, K. Togashi, H. Zhang, D. C. Van Essen, and T. Hayashi, “Diffusion Tensor Model links to Neurite Orientation Dispersion and Density Imaging at high b-value in Cerebral Cortical Gray Matter,” *Scientific Reports*, vol. 9, p. 12246, Aug. 2019. Number: 1 Publisher: Nature Publishing Group.
- [132] J. M. Guerrero, N. Adluru, B. B. Bendlin, H. H. Goldsmith, S. M. Schaefer, R. J. Davidson, S. R. Kescemeti, H. Zhang, and A. L. Alexander, “Optimizing the intrinsic parallel diffusivity in NODDI: an extensive empirical evaluation,” *PloS one*, vol. 14, no. 9, p. e0217118, 2019. Type: Journal Article.
- [133] A. Faiyaz, I. E. Kabir, M. M. Doyley, I. Sack, M. N. Uddin, and G. Schifitto, “Preliminary mr elastography investigation on hiv+ cohort with cerebral small vessel disease,” in *Proc. Intl. Soc. Mag. Reson. Med.* 29, 2021.
- [134] A. Faiyaz, M. M. Doyley, G. Schifitto, J. Zhong, and M. N. Uddin, “Deep learner estimated isotropic volume fraction enables reliable single-shell noddii reconstruction,” in *Proc. Intl. Soc. Mag. Reson. Med.* 29, 2021.

- [135] A. Faiyaz, M. Weber, I. Kabir, M. M. Doyley, I. Sack, M. N. Uddin, and G. Schifitto, “Evaluating mre-tract integrity in hiv-csvd cohort: A comprehensive analysis with functionally defined atlases and neurocognitive assessment,” in *Proc. Intl. Soc. Mag. Reson. Med.* 32, 2024.
- [136] A. Faiyaz, M. M. Doyley, G. Schifitto, and M. N. Uddin, “Artificial intelligence for diffusion MRI-based tissue microstructure estimation in the human brain: an overview,” *Frontiers in Neurology*, vol. 14, 2023. Publisher: Frontiers Media SA.
- [137] C. Eichner, S. F. Cauley, J. Cohen-Adad, H. E. Möller, R. Turner, K. Setsompop, and L. L. Wald, “Real diffusion-weighted MRI enabling true signal averaging and increased diffusion contrast,” *NeuroImage*, vol. 122, pp. 373–384, Nov. 2015.
- [138] F. Grussu, S. B. Blumberg, M. Battiston, L. S. Kakkar, H. Lin, A. Ianuş, T. Schneider, S. Singh, R. Bourne, S. Punwani, D. Atkinson, C. A. M. Gandini Wheeler-Kingshott, E. Panagiotaki, T. Mertzanidou, and D. C. Alexander, “Feasibility of Data-Driven, Model-Free Quantitative MRI Protocol Design: Application to Brain and Prostate Diffusion-Relaxation Imaging,” *Frontiers in Physics*, vol. 9, 2021.
- [139] I. O. Jelescu and M. D. Budde, “Design and validation of diffusion MRI models of white matter,” *Frontiers in physics*, vol. 28, p. 61, Nov. 2017.
- [140] E. A. Krijnen, A. W. Russo, E. Salim Karam, H. Lee, F. L. Chiang, M. M. Schoonheim, S. Y. Huang, and E. C. Klawiter, “Detection of grey matter microstructural substrates of neurodegeneration in multiple sclerosis,” *Brain Communications*, vol. 5, p. fcad153, June 2023.
- [141] M. Cieśluk, K. Pogoda, E. Piktel, U. Wnorowska, P. Deptuła, and R. Bucki, “Mechanical Properties of the Extracellular Environment of Human Brain Cells Drive the Effectiveness of Drugs in Fighting Central Nervous System Cancers,” *Brain Sciences*, vol. 12, p. 927, July 2022. Number: 7 Publisher: Multidisciplinary Digital Publishing Institute.
- [142] K.-D. Merboldt, W. Hanicke, and J. Frahm, “Self-diffusion NMR imaging using stimulated echoes,” *Journal of Magnetic Resonance (1969)*, vol. 64, pp. 479–486, Oct. 1985.
- [143] D. G. Taylor and M. C. Bushell, “The spatial mapping of translational diffusion coefficients by the NMR imaging technique,” *Physics in Medicine and Biology*, vol. 30, pp. 345–349, Apr. 1985.

- [144] L. J. O'Donnell, A. Daducci, D. Wassermann, and C. Lenglet, "Advances in computational and statistical diffusion MRI," *NMR in biomedicine*, vol. 32, p. e3805, Apr. 2019.
- [145] G. Zhu, B. Jiang, L. Tong, Y. Xie, G. Zaharchuk, and M. Wintermark, "Applications of Deep Learning to Neuro-Imaging Techniques," *Frontiers in Neurology*, vol. 10, 2019.
- [146] A. N. Nielsen, D. M. Barch, S. E. Petersen, B. L. Schlaggar, and D. J. Greene, "Machine Learning With Neuroimaging: Evaluating Its Applications in Psychiatry," *Biological Psychiatry: Cognitive Neuroscience and Neuroimaging*, vol. 5, pp. 791–798, Aug. 2020.
- [147] L. Jollans, R. Boyle, E. Artiges, T. Banaschewski, S. Desrivières, A. Grigis, J.-L. Martinot, T. Paus, M. N. Smolka, H. Walter, G. Schumann, H. Garavan, and R. Whelan, "Quantifying performance of machine learning methods for neuroimaging data," *NeuroImage*, vol. 199, pp. 351–365, Oct. 2019.
- [148] D. Ravi, N. Ghavami, D. C. Alexander, and A. Ianus, "Current Applications and Future Promises of Machine Learning in Diffusion MRI," in *Computational Diffusion MRI* (E. Bonet-Carne, F. Grussu, L. Ning, F. Sepehrband, and C. M. W. Tax, eds.), Mathematics and Visualization, (Cham), pp. 105–121, Springer International Publishing, 2019.
- [149] C.-L. Phuah, Y. Chen, J. F. Strain, N. Yechoor, O. J. Laurido-Soto, B. M. Ances, J.-M. Lee, and f. t. A. D. N. Initiative, "Association of Data-Driven White Matter Hyperintensity Spatial Signatures With Distinct Cerebral Small Vessel Disease Etiologies," *Neurology*, vol. 99, pp. e2535–e2547, Dec. 2022. Publisher: Wolters Kluwer Health, Inc. on behalf of the American Academy of Neurology Section: Research Article.
- [150] D. K. Jones and M. Cercignani, "Twenty-five pitfalls in the analysis of diffusion MRI data.," *NMR in Biomedicine*, vol. 23, pp. 803–820, Aug. 2010. MAG ID: 2015391962 S2ID: 77b79e9017e24f202f71fe2394bc43def105c428.
- [151] A. W. Anderson, "Measurement of fiber orientation distributions using high angular resolution diffusion imaging," *Magnetic Resonance in Medicine*, vol. 54, no. 5, pp. 1194–1206, 2005. _eprint: <https://onlinelibrary.wiley.com/doi/pdf/10.1002/mrm.20667>.
- [152] S. HashemizadehKolowri, R.-R. Chen, G. Adluru, and E. V. R. DiBella, "Jointly estimating parametric maps of multiple diffusion models from undersampled q-space data: A comparison of three deep learning approaches," *Magnetic Resonance in Medicine*, vol. 87, no. 6, pp. 2957–2971, 2022. _eprint: <https://onlinelibrary.wiley.com/doi/pdf/10.1002/mrm.29162>.

- [153] M. Afzali, T. Pieciak, S. Newman, E. Garyfallidis, E. Özarslan, H. Cheng, and D. K. Jones, “The sensitivity of diffusion MRI to microstructural properties and experimental factors,” *Journal of Neuroscience Methods*, vol. 347, p. 108951, Jan. 2021.
- [154] M. Bergamino, E. G. Keeling, R. R. Walsh, and A. M. Stokes, “Systematic Assessment of the Impact of DTI Methodology on Fractional Anisotropy Measures in Alzheimer’s Disease,” *Tomography*, vol. 7, pp. 20–38, Feb. 2021.
- [155] I. O. Jelescu, M. Palombo, F. Bagnato, and K. G. Schilling, “Challenges for biophysical modeling of microstructure,” *Journal of Neuroscience Methods*, vol. 344, p. 108861, Oct. 2020.
- [156] D. C. Van Essen, S. M. Smith, D. M. Barch, T. E. J. Behrens, E. Yacoub, K. Ugurbil, and WU-Minn HCP Consortium, “The WU-Minn Human Connectome Project: an overview,” *NeuroImage*, vol. 80, pp. 62–79, Oct. 2013.
- [157] M. Kleinnijenhuis, E. Johnson, J. Mollink, S. Jbabdi, and K. L. Miller, “A semi-automated approach to dense segmentation of 3D white matter electron microscopy,” Mar. 2020. Pages: 2020.03.19.979393 Section: New Results.
- [158] H.-H. Lee, K. Yaros, J. Veraart, J. L. Pathan, F.-X. Liang, S. G. Kim, D. S. Novikov, and E. Fieremans, “Along-axon diameter variation and axonal orientation dispersion revealed with 3D electron microscopy: implications for quantifying brain white matter microstructure with histology and diffusion MRI,” *Brain Structure and Function*, vol. 224, pp. 1469–1488, May 2019.
- [159] I. Hill, M. Palombo, M. Santin, F. Branzoli, A.-C. Philippe, D. Wassermann, M.-S. Aigrot, B. Stankoff, A. Baron-Van Evercooren, M. Felfli, D. Langui, H. Zhang, S. Lehericy, A. Petiet, D. C. Alexander, O. Ciccarelli, and I. Drobnyak, “Machine learning based white matter models with permeability: An experimental study in cuprizone treated in-vivo mouse model of axonal demyelination,” *NeuroImage*, vol. 224, p. 117425, Jan. 2021.
- [160] K. J. Friston, A. P. Holmes, K. J. Worsley, J.-P. Poline, C. D. Frith, and R. S. J. Frackowiak, “Statistical parametric maps in functional imaging: A general linear approach,” *Human Brain Mapping*, vol. 2, no. 4, pp. 189–210, 1994. _eprint: <https://onlinelibrary.wiley.com/doi/10.1002/hbm.460020402>.
- [161] J. L. Conel, “The cerebral cortex of the 3-month infant,” *The Anatomical Record*, vol. 97, p. 382, Mar. 1947.
- [162] D. C. Alexander, T. B. Dyrby, M. Nilsson, and H. Zhang, “Imaging brain microstructure with diffusion MRI: practicality and applications,” *NMR in biomedicine*, vol. 32, p. e3841, Apr. 2019.

- [163] R. Callaghan, D. C. Alexander, M. Palombo, and H. Zhang, “ConFiG: Contextual Fibre Growth to generate realistic axonal packing for diffusion MRI simulation,” *NeuroImage*, vol. 220, p. 117107, Oct. 2020.
- [164] H. Li, Z. Liang, C. Zhang, R. Liu, J. Li, W. Zhang, D. Liang, B. Shen, X. Zhang, Y. Ge, J. Zhang, and L. Ying, “SuperDTI: Ultrafast DTI and fiber tractography with deep learning,” *Magnetic Resonance in Medicine*, vol. 86, no. 6, pp. 3334–3347, 2021. _eprint: <https://onlinelibrary.wiley.com/doi/pdf/10.1002/mrm.28937>.
- [165] M. G. Hall and D. C. Alexander, “Convergence and Parameter Choice for Monte-Carlo Simulations of Diffusion MRI,” *IEEE Transactions on Medical Imaging*, vol. 28, pp. 1354–1364, Sept. 2009. Conference Name: IEEE Transactions on Medical Imaging.
- [166] D. N. Sousa and H. A. Ferreira, “MCSD: A MATLAB Tool for Monte-Carlo Simulations of Diffusion in biological Tissues,” *Journal of Open Source Software*, vol. 3, p. 966, Oct. 2018. <https://github.com/davidnsousa/mcsd/>.
- [167] I. Drobnjak, H. Zhang, A. İanuş, E. Kaden, and D. C. Alexander, “PGSE, OGSE, and sensitivity to axon diameter in diffusion MRI: Insight from a simulation study,” *Magnetic Resonance in Medicine*, vol. 75, no. 2, pp. 688–700, 2016. _eprint: <https://onlinelibrary.wiley.com/doi/pdf/10.1002/mrm.25631>.
- [168] S. Mikula, J. Binding, and W. Denk, “Staining and embedding the whole mouse brain for electron microscopy,” *Nature Methods*, vol. 9, pp. 1198–1201, Dec. 2012. Number: 12 Publisher: Nature Publishing Group.
- [169] S. Hsieh and M.-H. Yang, “Potential Diffusion Tensor Imaging Biomarkers for Elucidating Intra-Individual Age-Related Changes in Cognitive Control and Processing Speed,” *Frontiers in Aging Neuroscience*, vol. 14, p. 850655, Apr. 2022.
- [170] D. Novikov, J. Veraart, I. Jelescu, and E. Fieremans, “Mapping orientational and microstructural metrics of neuronal integrity with in vivo diffusion MRI,” Sept. 2016.
- [171] D. S. Novikov, J. Veraart, I. O. Jelescu, and E. Fieremans, “Rotationally-invariant mapping of scalar and orientational metrics of neuronal microstructure with diffusion MRI,” *NeuroImage*, vol. 174, pp. 518–538, July 2018.
- [172] D. S. Novikov, E. Fieremans, S. N. Jespersen, and V. G. Kiselev, “Quantifying brain microstructure with diffusion MRI: Theory and parameter estimation,” *NMR in Biomedicine*, vol. 32, no. 4, p. e3998, 2019. _eprint: <https://analyticalsciencejournals.onlinelibrary.wiley.com/doi/pdf/10.1002/nbm.3998>.

- [173] J. P. de Almeida Martins, M. Nilsson, B. Lampinen, M. Palombo, P. T. While, C.-F. Westin, and F. Szczepankiewicz, “Neural networks for parameter estimation in microstructural MRI: Application to a diffusion-relaxation model of white matter,” *NeuroImage*, vol. 244, p. 118601, Dec. 2021.
- [174] B. Anctil-Robitaille, A. Théberge, P.-M. Jodoin, M. Descoteaux, C. Desrosiers, and H. Lombaert, “Manifold-aware Synthesis of High-resolution Diffusion from Structural Imaging,” Aug. 2021. arXiv:2108.04135 [cs].
- [175] S. L. Merlet and R. Deriche, “Continuous diffusion signal, EAP and ODF estimation via Compressive Sensing in diffusion MRI,” *Medical Image Analysis*, vol. 17, pp. 556–572, July 2013.
- [176] I. H. Sarker, “Deep Learning: A Comprehensive Overview on Techniques, Taxonomy, Applications and Research Directions,” *SN Computer Science*, vol. 2, p. 420, Aug. 2021.
- [177] A. İanuş, J. Carvalho, F. F. Fernandes, R. Cruz, C. Chavarrias, M. Palombo, and N. Shemesh, “Soma and Neurite Density MRI (SANDI) of the in-vivo mouse brain and comparison with the Allen Brain Atlas,” *NeuroImage*, vol. 254, p. 119135, July 2022.
- [178] L. Zhan, A. D. Leow, N. Jahanshad, M.-C. Chiang, M. Barysheva, A. D. Lee, A. W. Toga, K. L. McMahon, G. I. de Zubicaray, M. J. Wright, and P. M. Thompson, “HOW DOES ANGULAR RESOLUTION AFFECT DIFFUSION IMAGING MEASURES?,” *NeuroImage*, vol. 49, pp. 1357–1371, Jan. 2010.
- [179] I. O. Jelescu, A. de Skowronski, F. Geffroy, M. Palombo, and D. S. Novikov, “Neurite Exchange Imaging (NEXI): A minimal model of diffusion in gray matter with inter-compartment water exchange,” *NeuroImage*, vol. 256, p. 119277, Aug. 2022.
- [180] J. L. Olesen, L. Østergaard, N. Shemesh, and S. N. Jespersen, “Diffusion time dependence, power-law scaling, and exchange in gray matter,” *NeuroImage*, vol. 251, p. 118976, May 2022.
- [181] Q. Tong, T. Gong, H. He, Z. Wang, W. Yu, J. Zhang, L. Zhai, H. Cui, X. Meng, C. W. M. Tax, and J. Zhong, “A deep learning-based method for improving reliability of multicenter diffusion kurtosis imaging with varied acquisition protocols,” *Magnetic Resonance Imaging*, vol. 73, pp. 31–44, Nov. 2020.
- [182] T. G. Close, J.-D. Tournier, F. Calamante, L. A. Johnston, I. Mareels, and A. Connelly, “A software tool to generate simulated white matter structures for the assessment of fibre-tracking algorithms,” *NeuroImage*, vol. 47, pp. 1288–1300, Oct. 2009.

- [183] L. Thesing, V. Antun, and A. C. Hansen, “What do AI algorithms actually learn? - On false structures in deep learning,” June 2019. arXiv:1906.01478 [cs, stat].
- [184] J. Veraart, D. S. Novikov, and E. Fieremans, “TE dependent Diffusion Imaging (TEdDI) distinguishes between compartmental T2 relaxation times,” *NeuroImage*, vol. 182, pp. 360–369, Nov. 2018.
- [185] M. Cottaar, F. Szczepankiewicz, M. Bastiani, M. Hernandez-Fernandez, S. N. Sotropoulos, M. Nilsson, and S. Jbabdi, “Improved fibre dispersion estimation using b-tensor encoding,” *NeuroImage*, vol. 215, p. 116832, July 2020.
- [186] J. Mollink, M. Kleinnijenhuis, A.-M. v. Cappellen van Walsum, S. N. Sotropoulos, M. Cottaar, C. Mirfin, M. P. Heinrich, M. Jenkinson, M. Pallebage-Gamarallage, O. Ansorge, S. Jbabdi, and K. L. Miller, “Evaluating fibre orientation dispersion in white matter: Comparison of diffusion MRI, histology and polarized light imaging,” *Neuroimage*, vol. 157, pp. 561–574, Aug. 2017.
- [187] A. Finkelstein, X. Cao, C. Liao, G. Schifitto, and J. Zhong, “Diffusion Encoding Methods in MRI: Perspectives and Challenges,” *Investigative Magnetic Resonance Imaging*, vol. 26, pp. 208–219, Dec. 2022.
- [188] M. N. Gurcan, L. E. Boucheron, A. Can, A. Madabhushi, N. M. Rajpoot, and B. Yener, “Histopathological image analysis: a review,” *IEEE reviews in biomedical engineering*, vol. 2, pp. 147–171, 2009.
- [189] P. J. Basser and C. Pierpaoli, “Microstructural and physiological features of tissues elucidated by quantitative-diffusion-tensor MRI,” *Journal of Magnetic Resonance. Series B*, vol. 111, pp. 209–219, June 1996.
- [190] H. Johansen-Berg and T. Behrens, *Diffusion MRI: From Quantitative Measurement to In vivo Neuroanatomy: Second Edition*. Elsevier, 2013.
- [191] Y. Assaf, T. Blumenfeld-Katzir, Y. Yovel, and P. J. Basser, “AxCaliber: a method for measuring axon diameter distribution from diffusion MRI,” *Magnetic Resonance in Medicine*, vol. 59, pp. 1347–1354, June 2008.
- [192] Y. Wang, Q. Wang, J. P. Haldar, F.-C. Yeh, M. Xie, P. Sun, T.-W. Tu, K. Trinkaus, R. S. Klein, A. H. Cross, and S.-K. Song, “Quantification of increased cellularity during inflammatory demyelination,” *Brain: A Journal of Neurology*, vol. 134, pp. 3590–3601, Dec. 2011.
- [193] J. Xu, X. Jiang, H. Li, L. R. Arlinghaus, E. T. McKinley, S. P. Devan, B. M. Hardy, J. Xie, H. Kang, A. B. Chakravarthy, and J. C. Gore, “Magnetic resonance imaging of mean cell size in human breast tumors,” *Magnetic Resonance in Medicine*, vol. 83, pp. 2002–2014, June 2020.

- [194] P. J. Basser, J. Mattiello, and D. LeBihan, “MR diffusion tensor spectroscopy and imaging,” *Biophysical Journal*, vol. 66, pp. 259–267, Jan. 1994.
- [195] P. T. Callaghan, C. D. Eccles, and Y. Xia, “NMR microscopy of dynamic displacements: k-space and q-space imaging,” *Journal of Physics E: Scientific Instruments*, vol. 21, p. 820, Aug. 1988.
- [196] P. J. Basser, J. Mattiello, and D. Lebihan, “Estimation of the Effective Self-Diffusion Tensor from the NMR Spin Echo,” *Journal of Magnetic Resonance, Series B*, vol. 103, pp. 247–254, Mar. 1994.
- [197] J. H. Jensen, J. A. Helpern, A. Ramani, H. Lu, and K. Kaczkynski, “Diffusional kurtosis imaging: The quantification of non-gaussian water diffusion by means of magnetic resonance imaging,” *Magnetic Resonance in Medicine*, vol. 53, no. 6, pp. 1432–1440, 2005. —eprint: <https://onlinelibrary.wiley.com/doi/pdf/10.1002/mrm.20508>.
- [198] V. Volodina and P. Challenor, “The importance of uncertainty quantification in model reproducibility,” *Philosophical transactions. Series A, Mathematical, physical, and engineering sciences*, vol. 379, no. 2197, p. 20200071, 2020.
- [199] D. Parker, A. A. Ould Ismail, R. Wolf, S. Brem, S. Alexander, W. Hodges, O. Pasternak, E. Caruyer, and R. Verma, “Freewater estimatoR using iNtErpolated iniTialization (FERNET): Characterizing peritumoral edema using clinically feasible diffusion MRI data,” *Plos one*, vol. 15, no. 5, p. e0233645, 2020. Type: Journal Article.
- [200] O. Bergmann, R. Henriques, C. Westin, and O. Pasternak, “Fast and accurate initialization of the free-water imaging model parameters from multi-shell diffusion MRI,” *NMR in Biomedicine*, vol. 33, no. 3, p. e4219, 2020. Type: Journal Article.
- [201] O. Pasternak, S. Kelly, V. J. Sydnor, and M. E. Shenton, “Advances in microstructural diffusion neuroimaging for psychiatric disorders,” *Neuroimage*, vol. 182, pp. 259–282, 2018. Type: Journal Article.
- [202] D. S. Novikov, J. Veraart, I. O. Jelescu, and E. Fieremans, “Rotationally-invariant mapping of scalar and orientational metrics of neuronal microstructure with diffusion MRI,” *NeuroImage*, vol. 174, pp. 518–538, 2018. Type: Journal Article.
- [203] R. N. Henriques, A. Rokem, E. Garyfallidis, S. St-Jean, E. T. Peterson, and M. M. Correia, “[Re] Optimization of a free water elimination two-compartment model for diffusion tensor imaging,” *BioRxiv*, p. 108795, 2017. Type: Journal Article.

- [204] L. J. Edwards, K. J. Pine, I. Ellerbrock, N. Weiskopf, and S. Mohammadi, “NODDI-DTI: estimating neurite orientation and dispersion parameters from a diffusion tensor in healthy white matter,” *Frontiers in neuroscience*, vol. 11, p. 720, 2017. Type: Journal Article.
- [205] I. Timmers, A. Roebroeck, M. Bastiani, B. Jansma, E. Rubio-Gozalbo, and H. Zhang, “Assessing microstructural substrates of white matter abnormalities: a comparative study using DTI and NODDI,” *PloS one*, vol. 11, no. 12, p. e0167884, 2016. Type: Journal Article.
- [206] F. Grussu, T. Schneider, H. Zhang, D. C. Alexander, and C. A. Wheeler-Kingshott, “Neurite orientation dispersion and density imaging of the healthy cervical spinal cord in vivo,” *Neuroimage*, vol. 111, pp. 590–601, 2015. Type: Journal Article.
- [207] A. R. Hoy, C. G. Koay, S. R. Kecskemeti, and A. L. Alexander, “Optimization of a free water elimination two-compartment model for diffusion tensor imaging,” *NeuroImage*, vol. 103, pp. 323–333, 2014. Type: Journal Article.
- [208] E. Garyfallidis, M. Brett, B. Amirbekian, A. Rokem, S. Van Der Walt, M. Descoteaux, and I. Nimmo-Smith, “Dipy, a library for the analysis of diffusion MRI data,” *Frontiers in neuroinformatics*, vol. 8, p. 8, 2014. Type: Journal Article.
- [209] S. N. Jespersen, L. A. Leigland, A. Cornea, and C. D. Kroenke, “Determination of axonal and dendritic orientation distributions within the developing cerebral cortex by diffusion tensor imaging,” *IEEE Trans Med Imaging*, vol. 31, no. 1, pp. 16–32, 2012. Type: Journal Article.
- [210] S. N. Jespersen, C. R. Bjarkam, J. R. Nyengaard, M. M. Chakravarty, B. Hansen, T. Vosegaard, L. Ostergaard, D. Yablonskiy, N. C. Nielsen, and P. Vestergaard-Poulsen, “Neurite density from magnetic resonance diffusion measurements at ultrahigh field: comparison with light microscopy and electron microscopy,” *Neuroimage*, vol. 49, no. 1, pp. 205–16, 2010. Type: Journal Article.
- [211] Y. Assaf and O. Pasternak, “Diffusion tensor imaging (DTI)-based white matter mapping in brain research: a review,” *Journal of molecular neuroscience*, vol. 34, no. 1, pp. 51–61, 2008. Type: Journal Article.
- [212] R. Dutta and B. D. Trapp, “Pathogenesis of axonal and neuronal damage in multiple sclerosis,” *Neurology*, vol. 68, no. 22 suppl 3, pp. S22–S31, 2007. Type: Journal Article.

- [213] J. C. Fiala, J. Spacek, and K. M. Harris, “Dendritic spine pathology: cause or consequence of neurological disorders?,” *Brain Res Brain Res Rev*, vol. 39, no. 1, pp. 29–54, 2002. Type: Journal Article.
- [214] C. Beaulieu, “The basis of anisotropic water diffusion in the nervous system—a technical review,” *NMR in Biomedicine: An International Journal Devoted to the Development and Application of Magnetic Resonance In Vivo*, vol. 15, no. 7-8, pp. 435–455, 2002. Type: Journal Article.
- [215] B. Jacobs, L. Driscoll, and M. Schall, “Life-span dendritic and spine changes in areas 10 and 18 of human cortex: A quantitative golgi study,” *Journal of Comparative Neurology*, vol. 386, no. 4, pp. 661–680, 1997. Type: Journal Article.
- [216] J. Mosso, D. Simicic, K. Şimşek, R. Kreis, C. Cudalbu, and I. O. Jelescu, “MP-PCA denoising for diffusion MRS data: promises and pitfalls,” *NeuroImage*, vol. 263, p. 119634, Sept. 2022.
- [217] N.-K. Chen, H.-C. Chang, A. Bilgin, A. Bernstein, and T. P. Trouard, “A diffusion-matched principal component analysis (DM-PCA) based two-channel denoising procedure for high-resolution diffusion-weighted MRI,” *PloS One*, vol. 13, no. 4, p. e0195952, 2018.
- [218] C. R. Figley, M. N. Uddin, K. Wong, J. Kornelsen, J. Puig, and T. D. Figley, “Potential Pitfalls of Using Fractional Anisotropy, Axial Diffusivity, and Radial Diffusivity as Biomarkers of Cerebral White Matter Microstructure,” *Frontiers in Neuroscience*, vol. 15, 2022.
- [219] Y. Masutani, “Recent Advances in Parameter Inference for Diffusion MRI Signal Models,” *Magnetic resonance in medical sciences: MRMS: an official journal of Japan Society of Magnetic Resonance in Medicine*, vol. 21, pp. 132–147, Mar. 2022.
- [220] A. Nowogrodzki, “The world’s strongest MRI machines are pushing human imaging to new limits,” *Nature*, vol. 563, pp. 24–26, Oct. 2018. Bandiera_abtest: a Cg_type: News Feature Number: 7729 Publisher: Nature Publishing Group Subject_term: Brain, Imaging, Neuroscience.
- [221] L. R. Ranzenberger and T. Snyder, “Diffusion Tensor Imaging,” in *StatPearls*, Treasure Island (FL): StatPearls Publishing, 2022.
- [222] C. M. Tax, F. Grussu, E. Kaden, L. Ning, U. Rudrapatna, C. John Evans, S. St-Jean, A. Leemans, S. Koppers, D. Merhof, A. Ghosh, R. Tanno, D. C. Alexander, S. Zappalà, C. Charron, S. Kusmia, D. E. Linden, D. K. Jones,

- and J. Veraart, “Cross-scanner and cross-protocol diffusion MRI data harmonisation: A benchmark database and evaluation of algorithms,” *NeuroImage*, vol. 195, pp. 285–299, July 2019.
- [223] L. Ning, E. Bonet-Carne, F. Grussu, F. Sepehrband, E. Kaden, J. Veraart, S. B. Blumberg, C. S. Khoo, M. Palombo, I. Kokkinos, D. C. Alexander, J. Coll-Font, B. Scherrer, S. K. Warfield, S. C. Karayumak, Y. Rathi, S. Koppers, L. Weninger, J. Ebert, D. Merhof, D. Moyer, M. Pietsch, D. Christiaens, R. A. Gomes Teixeira, J.-D. Tournier, K. G. Schilling, Y. Huo, V. Nath, C. Hansen, J. Blaber, B. A. Landman, A. Zhylka, J. P. W. Pluim, G. Parker, U. Rudrapatna, J. Evans, C. Charron, D. K. Jones, and C. M. W. Tax, “Cross-scanner and cross-protocol multi-shell diffusion MRI data harmonization: Algorithms and results,” *NeuroImage*, vol. 221, p. 117128, Nov. 2020.
- [224] A. Gupta, S. Nair, A. D. Schweitzer, S. Kishore, C. E. Johnson, J. P. Comunale, A. J. Tsioris, and P. C. Sanelli, “Neuroimaging of cerebrovascular disease in the aging brain,” *Aging and Disease*, vol. 3, pp. 414–425, Oct. 2012.
- [225] L. Chen, M. Mossa-Basha, N. Balu, G. Canton, J. Sun, K. Pimentel, T. S. Hatsukami, J.-N. Hwang, and C. Yuan, “Development of a quantitative intracranial vascular features extraction tool on 3D MRA using semiautomated open-curve active contour vessel tracing,” *Magnetic Resonance in Medicine*, vol. 79, pp. 3229–3238, June 2018.
- [226] L. Chen, T. Hatsukami, J.-N. Hwang, and C. Yuan, “Automated Intracranial Artery Labeling Using a Graph Neural Network and Hierarchical Refinement,” vol. 12266, pp. 76–85, 2020. Book Title: Medical Image Computing and Computer Assisted Intervention – MICCAI 2020 ISBN: 9783030597245 9783030597252 Place: Cham Publisher: Springer International Publishing.
- [227] A. Hilbert, V. I. Madai, E. M. Akay, O. U. Aydin, J. Behland, J. Sobesky, I. Galinovic, A. A. Khalil, A. A. Taha, J. Wuerfel, P. Dusek, T. Niendorf, J. B. Fiebach, D. Frey, and M. Livne, “BRAVE-NET: Fully Automated Arterial Brain Vessel Segmentation in Patients With Cerebrovascular Disease,” *Frontiers in Artificial Intelligence*, vol. 3, p. 552258, 2020.
- [228] S. Fan, Y. Bian, H. Chen, Y. Kang, Q. Yang, and T. Tan, “Unsupervised Cerebrovascular Segmentation of TOF-MRA Images Based on Deep Neural Network and Hidden Markov Random Field Model,” *Frontiers in Neuroinformatics*, vol. 13, p. 77, 2019.
- [229] Q. Wang, “HMRF-EM-image: Implementation of the Hidden Markov Random Field Model and its Expectation-Maximization Algorithm,” *ArXiv*, July 2012.

- [230] M. Reisert, E. Kellner, B. Dhital, J. Hennig, and V. G. Kiselev, “Disentangling micro from mesostructure by diffusion MRI: A Bayesian approach,” *NeuroImage*, vol. 147, pp. 964–975, Feb. 2017.